Optical NMR Study of ^{31}P Donor Spins in Isotopically Enriched ^{28}Si

by

Kamyar Saeedi Ilkhchy

M.Sc., Sharif University of Technology, 2008
B.Sc., University of Tabriz, 2005

Thesis Submitted In Partial Fulfillment of the
Requirements for the Degree of
Doctor of Philosophy

In the
Department of Physics
Faculty of Science

SIMON FRASER UNIVERSITY

Summer 2014

Approval

Name: **Kamyar Saeedi Ilkhchy**

Degree: **Doctor of Philosophy (Physics)**

Title of Thesis: ***Optical NMR Study of ^{31}P Donor Spins in Isotopically Enriched ^{28}Si***

Examining Committee: **Chair:** Dr. Bernd Stelzer
Assistant Professor

Dr. Michael L. W. Thewalt
Senior Supervisor
Professor

Dr. Simon P. Watkins
Supervisor
Professor

Dr. George Kirczenow
Supervisor
Professor

Dr. Patricia M. Mooney
Supervisor
Professor Emerita

Dr. Paul Haljan
Internal Examiner
Associate Professor

Dr. Kai-Mei Fu
External Examiner
Assistant Professor
Department of Electrical Engineering and Physics
University of Washington

Date Defended: July 14, 2014

Partial Copyright Licence

Abstract

A quantum computer requires a quantum system that is isolated from its environment, but can be integrated into devices, and whose states can be measured with high accuracy. Nuclear spin qubits using shallow neutral donors in semiconductors have been studied extensively as quantum memories due to their promise of long coherence lifetimes. However, the nuclear spins of neutral donors are not only difficult to initialize into known states and detect with high sensitivity, they are limited to use at cryogenic temperatures. The nuclear spins of ionized donors, on the other hand, have the potential for high-temperature operation.

In this thesis, I show how the distinctive optical properties of enriched ^{28}Si enable the use of hyperfine-resolved optical transitions (of donor bound excitons), as previously applied to great effect for isolated atoms and ions in vacuum. Together with efficient Auger photoionization, these optical transitions permit rapid nuclear hyperpolarization and electrical spin readout. These techniques are combined to detect nuclear magnetic resonance from dilute ^{31}P in an isotopically purified ^{28}Si sample, at concentrations inaccessible to conventional NMR techniques. Dynamical decoupling is used to measure cryogenic coherence times of over 180 seconds and 3 hours for an ensemble of neutral and ionized ^{31}P nuclear spins in ^{28}Si, respectively. A room-temperature coherence time of over 39 minutes is demonstrated in the latter system, which is more than an order of magnitude longer than the previous solid-state coherence time record. I further show that a coherent spin superposition can be cycled from 4.2 Kelvin to room temperature and back.

Keywords: ^{31}P donor spin qubit; isotopically enriched ^{28}Si; optical hyperpolarization; NMR; quantum coherence times; room temperature quantum memory

For my parents, Ali and Giti

Acknowledgements

I would like to express my deepest gratitude to my senior supervisor, Prof. Mike Thewalt, for accepting me to his research group and also for the excellent mentorship he has provided me over the past ~6 years. Being part of Mike's group gave me the unique opportunity to be involved in a high caliber research in collaboration with internationally known scientists. The enriched ^{28}Si samples, vital for this thesis, are provided through our collaborators involved in Avogadro project from Germany. I have greatly benefited from Mike's exceptional experimental skills that have made our lab unique by lots of handmade bits and pieces. Mike's ability to explain things clearly and simply without any equations resulting from his vast knowledge and experience was very valuable. I have found his enthusiasm and passion after more than 30 years of doing fundamental research in the lab admirable. I owe a great deal to Mike and the Department of Physics at Simon Fraser University for the generous financial support they have provided me over the past years.

My gratitude is also extended to my committee members Dr. George Kirczenow, Dr. Patricia Mooney and Dr. Simon Watkins for their useful advice, questions and fruitful discussion in our annual meetings. I would like to acknowledge Dr. John Morton and Dr. Stephanie Simmons for their brilliant ideas and useful collaboration. I would like to thank my friends and past colleagues, Michael Steger, Takeharu Sekiguchi and Albion Yang; and current lab mates, Jeff Salvail, Phillip Dluhy and Kevin Morse for the help they provided me on many occasions; specifically I acknowledge Phil who helped in proofreading this thesis. I'm really grateful to Bryan Gormann, Vic and Ken Myrtle, the extremely helpful technicians in the Physics department, and all the other people whose names I forgot to mention, but have supported me in working towards this goal.

At last but not least I would like to thank my parents who ultimately allowed me and my brother to enjoy the benefits of a much appreciated education. I will be forever indebted to them for all the support they have provided me throughout my life and specifically for allowing me to pursue my dream, and hope to never have to disappoint them. Also I want to thanks my brother, Elyar, who is by my side whenever I need him. Finally, I admire my first love, Neda, who was my greatest source of inspiration; her beautiful smile was my driving force.

Table of Contents

List of Tables

List of Figures

.

List of Acronyms

AEDMR	Auger Electron Detected Magnetic Resonance
A^0X	Acceptor bound exciton
BE	Bound Exciton
Cz	Czochralski (method)
CPMG	Carr-Purcell-Meiboom-Gill
CW	Continuous Wave
D^0	Neutral Donor
D^0X	Donor Bound Exciton
D^+	Ionized Donor
DDS	Direct Digital Synthesis
EDMR	Electrically Detected Magnetic Resonance
ENDOR	Electron Nuclear Double Resonance
EPR	Electron Paramagnetic Resonance
ESR	Electron Spin Resonance
fcc	Face Centered Cubic
FE	Free Exciton
FID	Free Induction Decay
Fz	Float Zone (method)
GS	Ground State
LO	Longitudinal Optical (phonon)
MW	Microwave
ND	Neutral Density (filter)
NMR	Nuclear Magnetic Resonance
NP	No Phonon
NV	Nitrogen Vacancy (defect center in diamond)
PC	Photoconductivity
PL	Photoluminescence
PLE	Photoluminescence Excitation
QC	Quantum Computation/Computing
QI	Quantum Information
QIP	Quantum Information Processing

RF	Radiofrequency
SNR	Signal to Noise Ratio
TA	Transverse Acoustic (phonon)
TO	Transverse Optical (phonon)
VCA	Virtual Crystal Approximation
WCP	Wavevector Conserving Phonon

1. Introduction

Humanity's desire (need) for computational power in modern society in order to solve hard problems such as simulating large biochemical systems, mining (searching and sorting) huge databases and deciphering codes, motivates the search for techniques and resources more powerful than classical supercomputers. Quantum computing (QC) and quantum information (QI) are the study of the information processing tasks that can be accomplished using quantum mechanical systems. The goals of QC and QI revolve around developing tools that sharpen our intuition about quantum mechanics and obtain fundamental insight into nature and take advantage of it to outperform today's classical computers on certain "hard" problems [1]. For some problems, quantum algorithms offer a polynomial speedup. The most well-known example of this is the quantum database search, which can be solved by Grover's algorithm [2]. Integer factorization is believed to be computationally infeasible with an ordinary computer for large integers if they are the product of few prime numbers. A quantum computer could efficiently solve this problem using Shor's algorithm [3, 4] allowing a quantum computer to decrypt many of the cryptographic systems in use today. Besides factoring of large composite numbers and quantum searching, quantum algorithms offering a more than polynomial speedup over the best known classical algorithm have been found for several other problems, including the simulation of quantum physical processes (quantum systems), relating to Feynman's early proposal [5]. These are just a few of several reasons to invest enormous amounts of time, energy and money in the effort to build QC devices.

The architectures for quantum computation can be categorized into three main groups [6]:

1) The gate or circuit based QC [7] relies upon a sequence of quantum operations, referred to as 'gates', applied to a well-initialised set of quantum bits (qubits) to process quantum information. (This will be the focus of the present thesis.)

2) The adiabatic QC [8] designates a single Hamiltonian to correspond to a full quantum sequence. The state is initialised into a known ground state (often at milliKelvin temperatures) and allowed to find the ground state of the modified Hamiltonian adiabatically. (This is very similar to the D-Wave[1] QC approach [9, 10] which may be easier to implement.)

3) The measurement-based QC [11-14] initialises its qubits into a particular entangled state (independent of which algorithm is to be applied), and then applies a sequence of conditional single-qubit measurements, leaving the output in the qubits not yet measured, and resulting in a sequence of quantum operations from left to right. The final output can then be read as usual.

1.1. Physical realizations of quantum computers

Building quantum information processing (QIP) devices is a great challenge for scientists and engineers of this century [15]. The theory of quantum error-correcting codes [16] strongly suggests that while quantum noise is a practical problem that needs to be addressed, it does not present a fundamental obstacle. Given the enormous potential applicability of QIP devices, how can they be achieved in a real physical system? What are the experimental requirements for building a quantum computer? To realize a quantum computer, we must not only give qubits robust physical representation, but also select a system in which they can be effectively manipulated. Furthermore, we must be able to prepare qubits in a specified set of initial states, and measure the final output state of the system. In other words these requirements [1] are the abilities to:

1. Robustly represent quantum information by qubits. If the choice of representation is poor, then decoherence will dominate resulting in loss of information.
2. Perform a universal family of unitary transformations on at least pairs of qubits. Two important factors to consider when evaluating the feasibility of implementing these unitary transformations are the achievable fidelity and the time required to perform these elementary operations.
3. Prepare a reasonably pure initial state (desired input). Note that it is only necessary to be able to repeatedly produce one specific quantum state with high fidelity.

[1] D-Wave Systems, Inc. is a quantum computing company, based in Burnaby, BC, Canada.

4. Measure the output result. A good figure of merit for measurement capability is the signal to noise ratio (SNR).

DiVincenzo has also presented a similar set of basic criteria for implementation of QC [17]. The challenge of experimental realization is that these fundamental requirements can often only be partially met and several prerequisites seem in opposition to each other. A quantum computer has to be well-isolated from its environment in order to retain its quantum properties, but at the same time its qubits have to be accessible to the control hardware so that they can be manipulated to perform a computation and to read out the result at the end. So, a realistic implementation must maintain a delicate balance between these constraints.

A key concept in understanding the merit of a particular candidate quantum computer is the notion of quantum noise, called decoherence (the process in which a system's behaviour changes from that which can be explained by quantum mechanics to that which can be explained by classical mechanics). This is because the length of the longest possible quantum computation is roughly given by the ratio of the time for which the system remains quantum-mechanically coherent to the time it takes to perform the required elementary unitary operations. These times are both determined by the strength of the coupling of the system to the external world. The timescale on which these relaxation processes occur can vary significantly (from shorter than nanoseconds to longer than minutes) and for the purposes of preserving quantum information over the course of an algorithm, longer times are better.

Clearly, much more can be said about various physical implementation proposals, which involve many different areas of physics, chemistry, and engineering, but are outside the scope of this study. Nevertheless, a brief overview of the trade-offs in selecting these QIP schemes is summarized in Table 1.1. Despite the number of entries in this table, only three fundamentally different qubit representations are given: photon, charge and spin. For the latest developments for each of the leading approaches one can refer to the recent review paper by Thaddeus Ladd [18].

Table 1.1: Brief characteristics of proposals for implementing quantum computers

Proposal based on	Major difficulty	Major advantage	Major disadvantage	General References.
Optical techniques	Producing single photons on demand	Photons are highly stable carriers of quantum information	Photons do not directly interact with one another	[19] [20] [21] [22]
Trapped atom/ion	Scaling up successes with small numbers of qubits	Superb state preparation and measurements	Weakness of phonon mediated spin-spin coupling	[23] [24] [25] [26] [27] [28]
Nuclear magnetic resonance	Directly accessing individual nuclei in a molecule	Superb dynamics in small molecules	Very noisy initial state	[29] [30] [31] [32]
Quantum Dots	Dephasing due to uncontrolled distant charge motion	Excellent techniques to create, control and measure even at single electron level	Relatively short coherence times for charge states	[33] [34] [35]
Cooper pairs/magnetic flux in Superconductors	Controlling electrostatic / magnetic fluctuation	Relative robustness Scalable devices	Very sensitive and short coherence	[36] [37]
Spins in semiconductors	Small coupling of nuclear spin/ hard to measure	Potential ability to scale-up tremendously	Non local coupling	[38] [39]

There is a large amount of work devoted to pursuing hybrid designs [40] which attempt to marry the best features of two or more existing technologies. The implementations of quantum information processing machines have developed into a fascinating and rich field; however, this thesis will be limited to a donor-spin-based all-silicon scheme, which has the advantage of building on our highly developed silicon nanotechnology.

1.1.1. Silicon-based donor spin qubits

Atomic, molecular, and optical quantum computing architectures continue to be studied; but motivation to envision some kind of solid state quantum computer is enormous[2]. The spin degree of freedom associated with electrons and nuclei is being intensively investigated as a key element of future quantum technologies. These spins have been investigated in a wide range of environments such as: the nuclei in a molecule moving freely in a liquid [41], the spin orientation of nuclei collectively in quantum dots [42], defect centers in crystalline samples like nitrogen vacancy centres in diamond [43], and finally, donors impurities in silicon [44]. Great progress has been made in the manipulation and measurement of qubits based on electronic spin states in semiconductors, including the electrical detection of the spin resonance of a single defect [45, 46], the detection of a single spin by magnetic resonance force microscopy [47], the single-shot electrical readout of an electron spin in a quantum dot [48], and the optical detection and manipulation of the electronic spin states of isolated nitrogen vacancy (NV) centers in diamond, including controlled coupling to the electronic and nuclear spins of other nearby centers [49-52].

The electron spin, which in an external *B* field has eigenstates either +1/2 (spin-up) or -1/2 (spin-down), respectively, the aligned and anti-aligned states of the spin with respect to a background magnetic field provides a potentially good representation for qubits. However, since the energy difference between different spin states is typically very small compared with other energy scales (such as the thermal energy at room temperature (RT))[3], the spin states of atoms are usually difficult to observe, and even more difficult to control. In carefully crafted environments, however, exquisite control is possible. Fortunately, spins are both long-lived (in particular, electron or nucleus donor spins in silicon can each have coherence time exceeding seconds [53-55]) and can be manipulated very quickly on the order of nanoseconds to microseconds [56, 57]. Both electronic and nuclear spins have their advantages and disadvantages for quantum information processing. Although both are long-lived in suitable systems, nuclear spins

[2] It has been estimated that the world has invested over US$1trillion in silicon technology since the invention of the transistor in the late 1940s.

[3] The energy of nuclear spin ($\mu_N B$) at B =10T is five orders of magnitude smaller than the thermal energy ($k_B T$) at RT (300K).

generally outlive electron spins due to their reduced couplings to the environment. However, since the nuclear spin is more isolated, the direct manipulation of it can be much slower, leading to correspondingly fewer operations within the qubit's coherence time. Electrons, on the other hand, couple to many different degrees of freedom, including multiple nuclei, photons, phonons and other unpaired electrons, making them easier to control but potentially leading to faster relaxation. There are many architecture proposals for using spin as a qubit, but a silicon-based hybrid electronic–nuclear system can make the best of both properties [58].

Recent proposals [17, 38, 39, 59, 60] to use the electron and nuclear spins of shallow donor impurities as qubits for Si-based QC have led to renewed interest in the properties of these systems [61-72]. Most of these studies focused on the phosphorus donor impurity, the most common shallow donor in Si, with only one stable isotope (^{31}P) with a nuclear spin of 1/2. Many of these QC schemes involve enriched ^{28}Si as the spin-free host material, because the elimination of the nonzero ^{29}Si nuclear spin greatly reduces coupling to the environment (decoherence) and improves coherence times. These approaches seek to take advantage of the highly developed state of silicon materials science and nanofabrication technology. Optical measurement and control of nuclear spins via the hyperfine interaction was absent from silicon based proposals, since these splittings were thought to be beyond the resolution limits of solid state spectroscopy. However, it has been shown [61] that the elimination of inhomogeneous isotope broadening inherent in highly enriched ^{28}Si has the added benefit of enabling an optical readout of the donor electron and nuclear spins using the resolved hyperfine components in the donor bound exciton (D^0X) transitions [62] due to remarkable reduction in linewidth compared to natural silicon. This is the realization of Fu's idea [73] for direct optical measurement of the nuclear spin state of a single ^{31}P impurity in ^{28}Si. This same property allows for the rapid hyperpolarization of both electron and nuclear spins at low magnetic fields by resonant optical pumping [65].

In 1998 Kane made a seminal proposal for a silicon-based QC [38]: precisely placing single phosphorous atoms (nuclear spin 1/2) within a crystalline wafer of ^{28}Si (nuclear spin 0), positioned beneath lithographically patterned electrostatic gates. These gates allow manipulation of the electron cloud surrounding the ^{31}P dopants, to perform single qubit operation via modulation of the hyperfine coupling seen by the ^{31}P nuclei.

Additional gates located above the region separating the ^{31}P dopants can be used to artificially create electron distributions connecting adjacent ^{31}P, much like a chemical bond, thus allowing two qubit operations to be performed. Although fabrication constraints of such a scheme are extremely challenging – for example, the gate should be separated by 10 nm or less, and the ^{31}P dopants must be registered precisely and in an ordered array. Nowadays, with sufficiently advanced technology, it is possible to place, control, and measure single nuclear spins in semiconductors [78], making Kane's vision of a silicon-based nuclear spin quantum computer [38] possible.

There has been recent and rapid progress in the development of a wide range of possible technologies for quantum information storage and processing [74]. The storage and retrieval of either quantum [60] or classical [75] information between the donor electron and nuclear spins, and the entanglement of these spins [76], have been demonstrated. Recently a single-atom transistor based on deterministic positioning of a phosphorus atom in epitaxial silicon using scanning tunnelling microscope (STM)–lithography has built [77]. Very recently the single-atom electron spin qubit in silicon [46] and high-fidelity readout and control of a nuclear spin qubit in silicon was demonstrated [78].

Nuclear spins of ionized P (D^+) in ^{28}Si as an ideal quantum memory

Beyond the enormous potential impact of quantum computation [7, 18], the development of a truly long term and portable quantum storage register operating at room temperature could lead to revolutionary new technologies such as "quantum money" and fraud-resistant quantum tokens [79, 80]. A recent breakthrough in solid-state quantum systems, which have the benefits of scalability and integration with existing devices, was the demonstration of a coherent storage time, or T_2, of ~2 s for the nuclear spin of a ^{13}C atom coupled to a NV center in diamond at room temperature [81]. Another promising semiconductor qubit system uses the electron and/or nuclear spins of shallow donor impurities such as ^{31}P in silicon [82]. Both of these host materials consist predominantly of an isotope with no nuclear spin (^{12}C or ^{28}Si), and spin coherence times can be extended by removing naturally-occurring isotopes having a nuclear spin, namely ^{13}C or ^{29}Si, each with nuclear spin I = 1/2 [83]. While the nuclear spin of neutral ^{31}P in ^{28}Si has demonstrated a record solid-state coherence time of 180 s [54], it is (like all

neutral shallow donors in Si) an inherently low temperature system. Even at 4.2 K the nuclear spin T_2 is limited by the electron spin relaxation time, T_1 [54], which decreases very rapidly with increasing temperature, reaching a few milliseconds at 10 K [84], and in addition the donors become thermally ionized above ~30 K.

Here we show that the nuclear spin of the ionized donor (D^+) has important advantages over that of the neutral donor (D^0), and is not limited to operation at cryogenic temperatures. There have been two very recent studies on the D^+ nuclear spin in natural Si, both at cryogenic temperatures: one using spin-dependent recombination to generate polarized D^+ in an ensemble [85], and another using a single electron transistor and electrical ionization to measure a single ^{31}P in the D^+ state [78]. In both of these devices, the nuclear spin T_2 of D^0 is believed to be limited by electric field noise arising from the nearby Si/SiO_2 interface, as the electric field couples to the nuclear spin by modulating its hyperfine interaction with the donor electron spin. The nuclear spin T_2 for D^+ was found to be considerably longer in both studies, as the removal of the electron spin eliminates this decoherence mechanism. The resulting D^+ spin coherence times of tens of milliseconds can be attributed to spectral diffusion from the ~5% of ^{29}Si naturally occurring in the samples [86]. By removing this source of spectral diffusion, using highly enriched ^{28}Si and dynamic decoupling, we find that the coherence time of $^{31}P^+$ can be extended to at least 180 min. at cryogenic temperatures. We further show that the D^+ nuclear spin is remarkably insensitive to temperature by measuring a lower bound for the coherence time at room temperature of 39 min.

1.2. Outline

This thesis exploits the possibilities of using the nuclear spin of neutral and ionized group V donors in general and ^{31}P donors specifically in isotopically enriched ^{28}Si as a quantum memory. We show that ^{28}Si not only provides a nuclear-spin-free environment, which leads to long T_{2e} and T_{2n}, but also permits a method for spin polarization and detection, which opens the door to exploring magnetic resonance of donors at densities below 10^{12} cm^{-3}. The dissertation will be organized as follows: In the next chapter (Chapter 2), I will briefly present the theory of the system we are working with. The samples and experimental methods and the apparatuses of the experiment

performed will be explained in Chapter 3. Finally, Chapter 4 will present the results of the project and provide a discussion of the findings.

2. Background and Theory

The theoretical framework of necessary topics related to this thesis work will now be presented. This chapter will explore the theory of quantum bits (qubits) and how to control them with magnetic resonance techniques, the spin interaction Hamiltonian and various decoherence channels, and how these topics manifest themselves in donor impurities in Si to make them a leading candidate for qubit implementation. Next, I will derive the energy levels of the Hamiltonian describing our spin qubit system (^{28}Si:P). Finally, theoretical limitations on the coherence time of these specific qubits based on previous works will be discussed.

2.1. Qubit

The most basic building block of a quantum computer is the quantum bit (qubit), which is often realized by a two-level quantum system. The difference between a classical bit and a qubit is that a qubit can be in a state other than just zero ($|0\rangle$) or one ($|1\rangle$), i.e., in a linear combination of states often called a superposition. This superposition principle is one of the key computational features of quantum mechanics which allows for the creation of states like:

$$|\psi\rangle = \alpha|0\rangle + \beta|1\rangle = \begin{pmatrix}\alpha\\ \beta\end{pmatrix}, \tag{2.1}$$

where the α and β are complex numbers referred as amplitudes and the '$|\ \ \rangle$' represent states in quantum mechanics. We can examine a bit to determine whether it is in the state 0 or 1. Actually computers do this all the time when they retrieve the contents of their memory. We cannot do this with qubits to find values of α and β.[4] Instead when we measure a qubit we obtain either a 0 or 1, with probability $|\alpha|^2$ or $|\beta|^2$, respectively.

[4] Unless infinitely many identically prepared qubits were measured.

Since the sum of these probabilities must be one ($|\alpha|^2 + |\beta|^2 = 1$), we can rewrite Equation (2.1) as:

$$|\psi\rangle = cos\frac{\theta}{2}|0\rangle + e^{i\varphi}sin\frac{\theta}{2}|1\rangle, \tag{2.2}$$

where θ and φ are real numbers which define a point on the unit three-dimensional sphere known as the Bloch sphere, as shown in in Figure 2.1. Although this geometric representation provides a useful means of visualizing the states of a single qubit, there is no equivalent representation for multiple qubits.

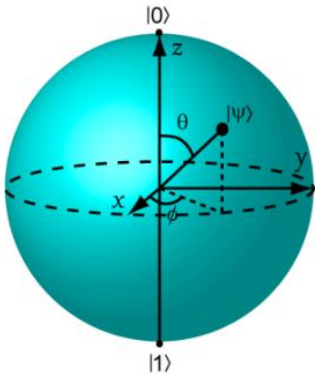

Figure 2.1: ***Bloch sphere representation of a qubit. A qubit's state can be any vector lying inclusively within the unit sphere, where the $|0\rangle$ and $|1\rangle$ eigenstates are along the z axis by convention. Pure (mixed) states occupy the surface (full body) of the sphere.***

Many different physical systems can be used to realize qubits, for example, the two different polarization states of a photon, two energy states of an electron orbiting a single atom or the alignment of nuclear spin in a magnetic field could all be potential qubits. The latter is the center of discussion for the rest of this thesis. It should be mentioned that spins controlled using magnetic resonance have provided the first [87], most advanced [88, 89], and highest fidelity [90] experimental demonstrations of quantum algorithms to date.

2.2. Semiconductor silicon as an important platform

Next to oxygen, silicon is the most abundant element on the earth. Certain refining problems impeded the use of silicon in the early days of semiconductors. Once these problems were solved, the advantages of silicon immediately made it the semiconductor of choice. Without it, modern electronics, communication, and computers (and maybe quantum computers) would be impossible [91]. Silicon, a group IV element (with four valence electrons and diamond crystal structure), is by far the most common and well known semiconductor used in integrated circuits. The Si structure can be visualized by considering a face-centered cubic (fcc) lattice with two atoms for each lattice site (the second one at one quarter of the diagonal length along the [111] direction) as shown in Figure 2.2. Every atom in this tetrahedral structure, the building block of the diamond lattice, forms a covalent bond with its four nearest neighbours resulting in electrons being shared between atoms, so the valence energy shell of each atom is full by eight shared valence electrons [92].

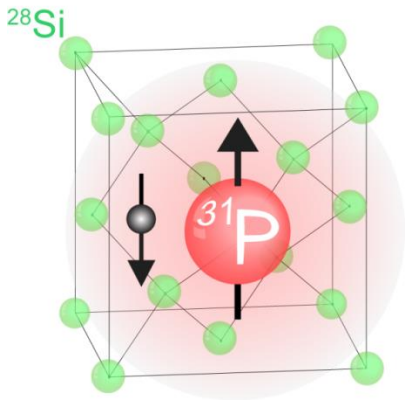

Figure 2.2: ***Schematics of the silicon diamond lattice populated only with ^{28}Si with a single substitutional ^{31}P at the center surrounded by its electron cloud.***

The band structure of the highest energy valence band and the lowest energy conduction band in silicon is shown schematically in Figure 2.3. The maximum of the valence band occurs at the Brillouin zone center (k = 0) and a minimum of the conduction band is seen to occur at approximately 85% of the distance to the zone boundary along the [001] direction, producing an indirect band gap (E_g). The hole states

near the valence band maxima are classified by their angular momentum j_h. The spin-orbit interaction splits the j_h=1/2 valence band (referred to as the split-off band) from the j_h=3/2 bands (referred to as the light hole and heavy hole bands).

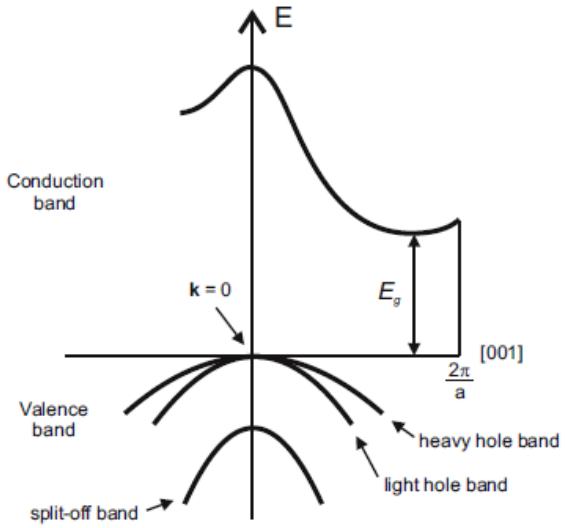

Figure 2.3: Schematic band structure for silicon along the [001] direction [93]

Silicon, like almost all other semiconductors in its natural form, consists of a mixture of stable isotopes with a fixed natural abundance. The three stable isotopes of Si with their natural abundances are shown in Table 2.1.

Table 2.1: Some important properties of silicon

Lattice constant (A°)	5.43
Atomic density (atoms/ cm^{-3})	5.0 x 10^{22}
Band gap energy (eV)	1.12eV@300K and 1.17eV@4.2K
Stable isotopes (natural abundances)	^{28}Si (92.23%), ^{29}Si (4.67%) and ^{30}Si (3.10%)
Nuclear spin of isotopes	^{28}Si (0), ^{29}Si (1/2) and ^{30}Si (0)
Normal impurities	^{31}P as a shallow donor, B acceptor, C, O

Due to its central role in conventional electronics, silicon has become one of the most highly purified materials, with impurity and defect densities typically measured in parts per billion or below. Even the isotopic variation in silicon can be controlled. We

believe Si can bridge the gap between approaches to quantum information processing: providing long quantum information lifetimes and high fidelity operations within a semiconductor device.

2.2.1. Donor impurities in silicon

In a real crystal, the lattice is not perfect; that is, the perfect geometric periodicity is disrupted in some manner, and contains imperfections or defects such as substitutional or interstitial impurities.

Phosphorus (^{31}P), is a group V substitutional shallow impurity in silicon (Si) that has one extra proton and one extra electron compared to the surrounding Si atoms (illustrated in Figure 2.2). The attractive Coulomb potential between this extra electron and the P nucleus is screened by the core electrons of the P atom, as well as its four remaining valence electrons and all of the valence electrons of the neighbouring Si atoms, so that the extra valence electron is only loosely bound to the P atom. This loosely bound electron can be easily ionized by thermal, electrical or optical excitations, and as a result, the P atom 'donates' an electron to the Si conduction band. This is the reason why P in Si is referred to as a donor impurity. The discrete energy levels revealed in the optical spectrum at low temperatures show that P impurities can be considered analogous to a hydrogen atom embedded in the Si lattice. The net effect of the crystal potential on the donor electron is that it changes the mass of the electron from its value in free space to the effective mass m^*. A detailed analysis of shallow impurities in silicon using the effective mass approximation can be found in the review article by Kohn [94-96].

Phosphorus is monoisotopic with an atomic mass of 31. ^{31}P has a nuclear spin I of 1/2, which couples to the S = 1/2 spin of the donor electron. In the absence of a magnetic field, this results in a three-fold degenerate state corresponding to total spin F=1, called the triplet state and a singlet state corresponding to F=0, with the energy separation being the hyperfine constant A, which has been previously measured to be equal to 117.53MHz [97]. The degeneracy of the F = 1 triplet state can be lifted by the application of an external magnetic field (details in section 2.5).

In this work, the qubits under investigation are dilute (< 10^{15} cm^{-3}) donor atoms (D), namely ^{31}P (I = 1/2), hosted in crystalline silicon. These donors have energies in the semiconductor band gap of silicon, sitting slightly below the conduction band, with binding energies (E_d) of 45 meV.

Energy level structure of donors in unstrained silicon

The ground state of hydrogenic donors forms just below the conduction band minimum, which is sixfold degenerate in k-space. This implies that the donors' electronic energy states are formed out of six equivalent ellipsoids about the k = 0 point, and because all electronic wavefunctions must conform to the tetrahedral symmetry of the lattice, the 1s ground state must be sixfold degenerate as well. The six 1s states can be broken apart into singlet, doublet and triplet states. The singlet is an even superposition of all six ellipsoids (a member of the “A" symmetry point group), triplets are an odd superposition of two coaxial ellipsoids (and are themselves threefold degenerate (of the “T2" point group), and the doublets are the two remaining antisymmetric orthogonal combinations (of the “E" point group). The singlet, doublet and triplet states each experience a different potential due to the nucleus; phosphorus has low-lying 1s:A states which, when split due to the Zeeman interaction, make up the qubit ground state. Due to parity, it is only the 1s:A state which experiences a hyperfine splitting with the nucleus [6].

2.2.2. Excitons and donor bound excitons (D^0X) in silicon

The electron-hole pair, bound by the Coulomb interaction, is referred to as a free exciton (FE) in silicon and it is typically formed when a photon with above band gap energy excites an electron from the valence band to the conduction band, leaving behind a hole in the valence band. There are two main types of excitons: 1) Frenkel excitons in which the electron and hole are tightly bound to each other and have radius on the order of the lattice spacing. 2) Wannier-Mott excitons consisting of a loosely bound electron-hole pair and having a radius much larger than the lattice spacing. The second type is most common in silicon [96]. A bound exciton (BE) is an electron-hole pair that is localized at a neutral impurity. The existence of BE was first proposed by Lampert [98] and later observed experimentally in silicon by Haynes [99] who noted the presence of

sharp luminescence lines at energies lower than the free exciton energy. This subsequently led to the development of a quantitative method for characterizing these impurities in silicon based on photoluminescence (PL) spectroscopy of bound excitons [100]. Due to the indirect band gap of Si and the requirement for wave vector conservation, the PL intensity of BE occurs with the participation of wave-vector conserving phonons (WCP). The dominant WCP replica is the transverse optical (TO), but the longitudinal optical (LO) and transverse acoustic (TA) WCP also exist. Also, a weak no-phonon (NP) transition is allowed by scattering from the short range potential known as the central cell potential near the donor ion. In the PL spectrum of the ground state of a donor bound exciton (D^0X) in silicon as illustrated in Figure 2.4, there is typically a no-phonon transition as well as phonon-assisted transitions (generally broader than NP due to phonon dispersion and lifetime) which occur at lower energy [101].

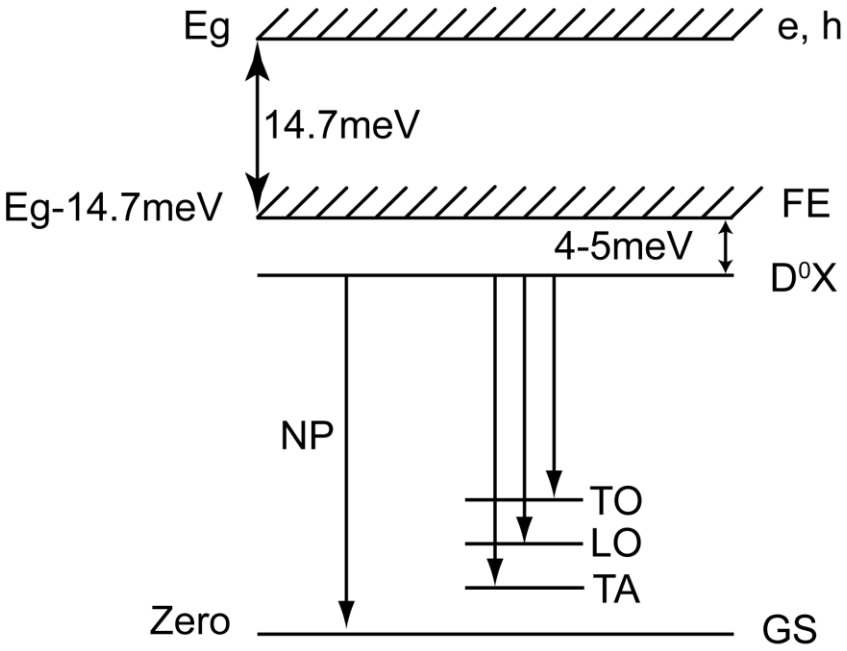

Figure 2.4: ***Schematic total energy diagram for the PL spectrum of D^0X in Si. GS is the crystal ground state and 4-5 meV is the localization energy of donor bound exciton (D^0X) compared to a neutral donor and a free exciton (FE). The FE energy continuum starts 14.7meV (binding energy) below the free electron and free hole energy continuum which starts at the band gap energy (Eg).***

Another consequence of the Si indirect band gap for the D^0X is the very low PL quantum efficiency (10^{-4} for P) that results from the long radiative lifetime, thus leading to the dominance of nonradiative Auger recombination [102, 103]. In the Auger decay of D^0X, the energy resulting from the recombination of the electron-hole pair is used to ionize the neutral donor, leaving behind an ionized donor (D^+) and an energetic free electron. Further details of shallow donor BE in Si are found in several reviews [104, 105].

The D^0X consists of two interacting electrons and one hole, as well as the fixed positive donor ion. In the ground state D^0X, it is energetically favourable for the two electrons to occupy the lowest valley-orbit state (1s), forming a spin singlet, removing the electrons' paramagnetic contribution to the BE energy levels. Instead, it is the spin-3/2 hole which splits the energy levels of the BE under a magnetic field, as shown in the Figure 2.5. We assume that the hyperfine coupling between the hole and the nucleus in the D^0X is negligible since the hole wave function is p-like and therefore has a node at the nucleus.

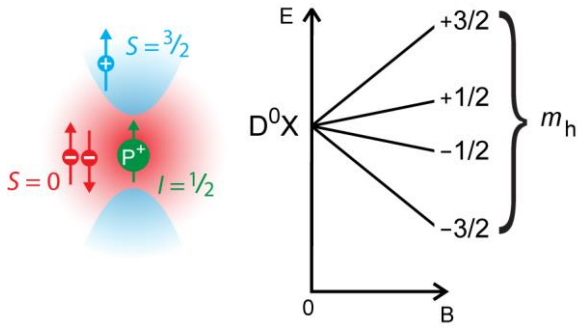

Figure 2.5: ***D^0X schematic and energy levels under a magnetic field showing the Zeeman splitting and hole spin projection. Note that there is no hyperfine interaction between the hole spin and the nuclear spin, and the two electrons form a singlet ground state.***

2.2.3. Highly enriched ^{28}Si as a perfect semiconductor vacuum

Traditionally, the properties of a semiconductor are determined by its elemental composition and structure. However, in the last 20 years isotopic composition has been shown to be another very important determinant of the optical, electrical, and magnetic

properties of semiconductors [106]. The studies of isotope effects in Si was limited to thermal conductivity [107] and Raman scattering [108] due to the lack of sufficiently isotopically pure bulk Si samples (enriched to more than 99.9% ^{28}Si). However, recently, the international Avogadro project[5] was launched [109] and continues to produce extremely isotopically pure ^{28}Si crystals [110]. The availability of ^{28}Si in the form of a bulk single crystal with a reasonably high chemical purity and high isotopic purity allowed for the investigation of isotopic composition effects on the optical and electronic properties. The results of isotopic effects on the optical spectra of semiconductors have been summarized in a comprehensive review [111].

The first photoluminescence (PL) spectroscopy study [61] revealed significantly sharper no-phonon (NP) donor bound exciton (D^0X) transition lines compared to those seen in natural Si (^{nat}Si). This sharpening [61, 112-114] of the NP bound exciton (BE) transition for phosphorus (P) reduces the full width at half maximum (FWHM) from 0.041 cm^{-1} (5.1 μeV) in natural silicon to 0.014 cm^{-1} (1.7 μeV) in enriched ^{28}Si (limited by instrumental resolution of the Fourier transform spectrometer). It appeared that the BE linewidth in ^{nat}Si was limited by inhomogeneous isotope broadening, an effect not accounted for within the virtual crystal approximation (VCA), in which the actual crystal is approximated by a hypothetical one with identical atoms having the average isotopic mass, ignoring the effects of local differences in the isotopic mass.

This statistical fluctuation of the local isotopic composition within the effective volume of the BE of radius 3.5 nm leads to local fluctuations in the band gap energy causing the inhomogeneous broadening in ^{nat}Si. In the same study, it was found that there exists a 0.92 cm^{-1} (110 μeV) decrease in the indirect band gap energy of the highly enriched ^{28}Si sample relative to ^{nat}Si, due to the renormalization of E_g by the electron-phonon interaction. In addition to sharper PL lines, the infrared absorption resulting from transitions between the electronic ground state of neutral donor and acceptor impurities and their bound excited states revealed many transitions with reduced linewidths in ^{28}Si as compared to ^{nat}Si [115-118].

[5] Approach to redefine kilogram based on the Avogadro number determination of very highly isotopically purified ^{28}Si single crystal sphere.

Though these topics will not be explored in any more depth, PL studies on copper-related impurity centres in ^{28}Si have led to the discovery of four- and five-atom complexes in Si that contain combinations of copper [119], silver, gold [120], platinum [121] and lithium atoms, thanks to the greatly reduced linewidths of the PL transitions associated with these centres in ^{28}Si [122, 123]. Further reading on the photoluminescence of deep defects involving transition metals in ^{28}Si and the new insights that have been revealed is summarized in a review paper [117].

By eliminating almost all inhomogeneous broadening and spins in the host crystal, highly enriched ^{28}Si approaches a semiconductor vacuum [54], enabling the use of hyperfine-resolved optical transitions, as is standard for atom and ion qubits in vacuum, but retaining the advantages of Si device technology, Auger photoionization for polarization and readout, and the ability to precisely and permanently place the qubit atoms [124].

2.3. Magnetic resonance in QC

Direct manipulation and detection of nuclear spin states using radiofrequency (RF) electromagnetic waves is a well-developed field known as nuclear magnetic resonance (NMR). These techniques are widely used in chemistry to measure properties of liquids, solids, and gases, to determine the structure of molecules, and to image materials. These many applications have led to NMR technology becoming quite sophisticated, allowing control and observation of tens to thousands of nuclei in an experiment. The coherent control of nuclear spin dynamics has recently been taken to a new level, motivated by the interest in quantum information processing [125]. Pulsed magnetic resonance provides a way of manipulating quantum systems such as nuclear and electron spins, and has proven itself to be a powerful tool in the development of quantum computation. Liquid state NMR has been the main experimental implementation of quantum protocols, allowing exquisite control of systems up to seven

qubits in size [29]. The scalability limitations[6] surrounding NMR implementations [31] that arise from the small nuclear Zeeman energy (causing difficulty in initializing nuclear spin into a pure state under reasonably high magnetic field and low temperature) can be overcome by turning to electron paramagnetic resonance (EPR), analogous in many ways to NMR but with the advantage that pure states are experimentally accessible. These strengths have led to many EPR-based solid state quantum information processing proposals [126-129].

For the purpose of this thesis, we will examine NMR for one and two spin systems. First, we must describe how electromagnetic radiation interacts with a single magnetic spin; then we will consider the physical nature of coupling between spins (spin-spin coupling).

2.3.1. Single spin dynamics

The interaction of a magnetic field with a spin is described by the Hamiltonian $H = -\vec{\mu} \cdot \vec{B}$, where $\vec{\mu}$ is the spin magnetic moment, and $B = B_0\hat{z} + B_1(\hat{x}\cos\omega t + \hat{y}\sin\omega t)$ is a typical applied magnetic field. B_0 is static and very large compared to B_1, which is several orders of magnitude smaller so that perturbation theory can be employed to study this system [1]. Unpaired electrons (with spin S = 1/2) and spin-active nuclei (S > 0) are paramagnetic. They respond to a magnetic field by adjusting their (2S + 1) spin eigenstates' energies. This breaking of degeneracy through the Zeeman interaction splits the eigenstates' energy levels. For the simplest case of spin-½ particles, the states are split to the aligned or anti-aligned eigenstates with the magnetic field. At a fixed magnetic field this energy splitting corresponds to a frequency that can be used to drive population transitions between the eigenstates. The frequencies for electronic transitions are much higher than the nuclear ones in the fixed magnetic field due to the difference in the Bohr and nuclear magnetons (μ_B=13.9962 GHz/T compared to μ_n=7.6 MHz/T). This electron splitting can be >> kT, so large equilibrium polarization is possible, which is useful for initialization or as computational

[6] As the number of qubits increases, the signal resulting from the pseudo-pure state preparation decreases exponentially. This decay quickly becomes prohibitive and renders quantum error correction ineffective.

resources [60] but also makes electrons a strong contributor to nuclear decoherence [130].

2.3.2. Spin-spin coupling

More than one spin is usually present in systems of interest (^{31}P and ^{29}Si which both have nuclear spin ½ in addition to the electron spin of ^{31}P). These spins interact through two dominant mechanisms: direct dipolar coupling, and indirect coupling through bond-electron-mediated interactions (from wavefunction overlap), also known as J-coupling [131]. The impurity concentrations of the purified Si samples reduced to the extent that inter-donor interactions become negligible, so ignoring J-coupling is an excellent approximation. We shall be interested in the case where dipolar coupling is dominant due to the very low concentration of ^{31}P impurities and the very high isotopic purities of our ^{28}Si samples. We are mainly interested in the nuclear spin of P donors, so the main source of decoherence is the coupling of P donors to the electron spin.

2.4. Hamiltonian of the Si:P spin system

The response of the phosphorus ^{31}P donor nucleus and its associated electron in isotopically pure ^{28}Si (denoted as ^{28}Si:P employed in this thesis) to its environment and a magnetic field will be explored in this section. The neutral phosphorus donor $^{31}P^0$ ground state in Si under an external static magnetic field $\mathbf{B} = B_0\hat{\mathbf{z}}$ along the Z axis is described with the following basic two-spin Hamiltonian in frequency units (**S** and **I** being spin operators of the donor electron and ^{31}P nucleus respectively),

$$H_{Si:P} = -\gamma_{\mathrm{e}}\mathbf{S}_{\mathrm{e}} \cdot \mathbf{B} - \gamma_{\mathrm{p}}\mathbf{I}_{\mathrm{p}} \cdot \mathbf{B} + A\mathbf{S}_{\mathrm{e}} \cdot \mathbf{I}_{\mathrm{p}}$$

$$= |\gamma_e| S_z B_0 - \gamma_p I_z B_0 + a(S_z I_z + (S_+ I_- + S_+ I_-)/2) \qquad (2.3)$$

Where $\gamma_{\mathrm{e}} = -g_e\mu_B = 115.68\ \frac{\mu eV}{T} = 27.972\ \frac{GHz}{T}$ and $\gamma_{\mathrm{P}} = g_P\mu_n = 71.346\ \frac{neV}{T} = 17.252\ \frac{MHz}{T}$ are the gyromagnetic ratios of electron and P nucleus respectively, and $A = a/h = 486.07\ neV = 117.53\ MHz$ is the hyperfine constant [97]. The first and second terms are the Zeeman energies of the donor electron (S=1/2) and the ^{31}P

nucleus (I=1/2), respectively, while the last term represents the hyperfine interaction between the electronic and nuclear spins. This hyperfine interaction, which comes about from the direct coupling of a nucleus to an orbiting electron, permits selective operations on the nuclei and electron as the transitions will be given by different nuclear and electronic frequencies. Note that the Hamiltonian for $^{31}P^{+}$ has only the central term ($-\gamma_p \mathbf{I}_p \cdot \mathbf{B}$). The approximate eigenstates of the spin Hamiltonian can be given in the (m_e, m_I) representation, where m_e is the electron spin projection and m_I is the ^{31}P nuclear spin projection. In the notation used here, the single (↑ or ↓) and double (⇑ or ⇓) arrows denote the electron and nuclear spins, respectively, with an 'up' arrow denoting an eigenvalue of +1/2 and a 'down' arrow denoting an eigenvalue of –1/2. The eigenvalues of the spin Hamiltonian give the energies of the four resolved hyperfine branches of the ^{31}P donor ground state. The four neutral donor (D^0) hyperfine levels, labeled by their electron and nuclear spins, and ionized donor (D^+) ground states, in the low field regime where the nuclear Zeeman energy is small, are shown in Figure 2.6 (the $|\uparrow\Downarrow\rangle$ and $|\downarrow\Uparrow\rangle$ labels are approximate at low B_0 because of hyperfine mixing).

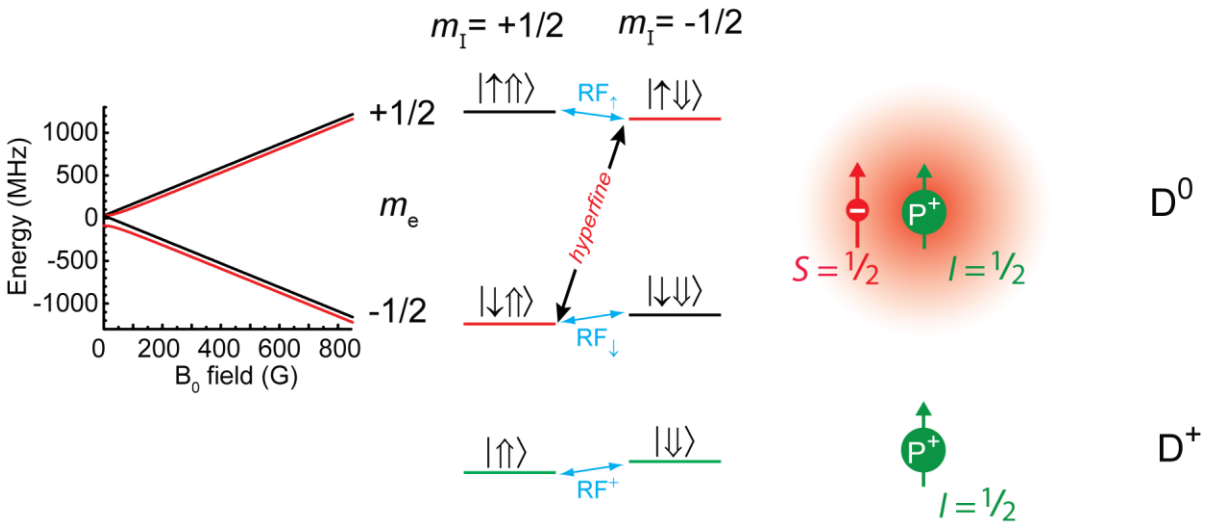

Figure 2.6: ***The schematic energy level diagram of the D^0 and D^+ ground state together with Zeeman splittings are shown from B_0=0 to 845G including the hyperfine splitting of the D^0 ground state. The magnitude of the D^+ Zeeman splitting has been exaggerated to show the ordering of the D^+ states.***

Even with the hyperfine interaction, the parallel-spin states $|\uparrow\Uparrow\rangle$ and $|\downarrow\Downarrow\rangle$ are energy eigenstates with the energy eigenvalues given by linear functions of B_0 for these pure states:

$$E_{|\uparrow\Uparrow\rangle}(B_0) = \frac{A}{4} + \frac{(\gamma_e - \gamma_p)B_0}{2} \tag{2.4}$$

$$E_{|\downarrow\Downarrow\rangle}(B_0) = \frac{A}{4} - \frac{(\gamma_e - \gamma_p)B_0}{2} \tag{2.5}$$

The energies of the two antiparallel-spin states $|\uparrow\Downarrow\rangle$ and $|\downarrow\Uparrow\rangle$ (for simplicity, we denote the mixed states by the spin eigenstates to which they tend in the limit of high B, but always have an admixture of the other component) are non-linear functions of the field.

$$E_{|\uparrow\Downarrow\rangle}(B_0) = -\frac{A}{4} + \sqrt{\left(\frac{A}{2}\right)^2 + \left(\frac{(\gamma_e + \gamma_p)B_0}{2}\right)^2} \tag{2.6}$$

$$E_{|\downarrow\Uparrow\rangle}(B_0) = -\frac{A}{4} - \sqrt{\left(\frac{A}{2}\right)^2 + \left(\frac{(\gamma_e + \gamma_p)B_0}{2}\right)^2} \tag{2.7}$$

At B = 0, $|\uparrow\Downarrow\rangle$ state is degenerate with $|\uparrow\Uparrow\rangle$ and $|\downarrow\Downarrow\rangle$ states, with energy of $A/4$, while $E_{|\downarrow\Uparrow\rangle}$ is lower by an amount of $3A/4$. At low field, $E_{|\uparrow\Downarrow\rangle}$ increases quadratically in B_0 and crosses $E_{|\uparrow\Uparrow\rangle}$ at ~3.4 Tesla (calculated later in this section), while $E_{|\downarrow\Uparrow\rangle}$ decreases quadratically in B_0 and never crosses $E_{|\downarrow\Downarrow\rangle}$. From the energy Equations (2.4) to (2.7), the NMR frequencies for the up and down electron spin branches, labelled in Figure 2.6 by $RF_\uparrow$ and $RF_\downarrow$ respectively, are:

$$\mathrm{RF}_\uparrow(B_0) = E_{|\uparrow\Uparrow\rangle} - E_{|\uparrow\Downarrow\rangle} = \frac{A}{2} + \left[\frac{(\gamma_e - \gamma_p)B_0}{2} - \sqrt{\left(\frac{A}{2}\right)^2 + \left(\frac{(\gamma_e + \gamma_p)B_0}{2}\right)^2}\right] \tag{2.8}$$

$$\mathrm{RF}_\downarrow(B_0) = E_{|\downarrow\Downarrow\rangle} - E_{|\downarrow\Uparrow\rangle} = \frac{A}{2} - \left[\frac{(\gamma_e - \gamma_p)B_0}{2} - \sqrt{\left(\frac{A}{2}\right)^2 + \left(\frac{(\gamma_e + \gamma_p)B_0}{2}\right)^2}\right] \tag{2.9}$$

The $\mathrm{RF}_{\uparrow}$ + $\mathrm{RF}_{\downarrow}$= A for any B_0 values and as shown in Figure 2.7, the NMR frequency for electron spin-up branch (and electron down branch) has a maximum (and minimum) at ~845 Gauss (B_{m}). The crossing point of the upper branch (m_e=+1/2) is given as $\mathrm{RF}_{\uparrow}(B_c) = 0$. Hence,

$$B_c \approx \frac{\mathrm{A}}{2\gamma_p} = 3.4043\ \mathrm{T} \tag{2.10}$$

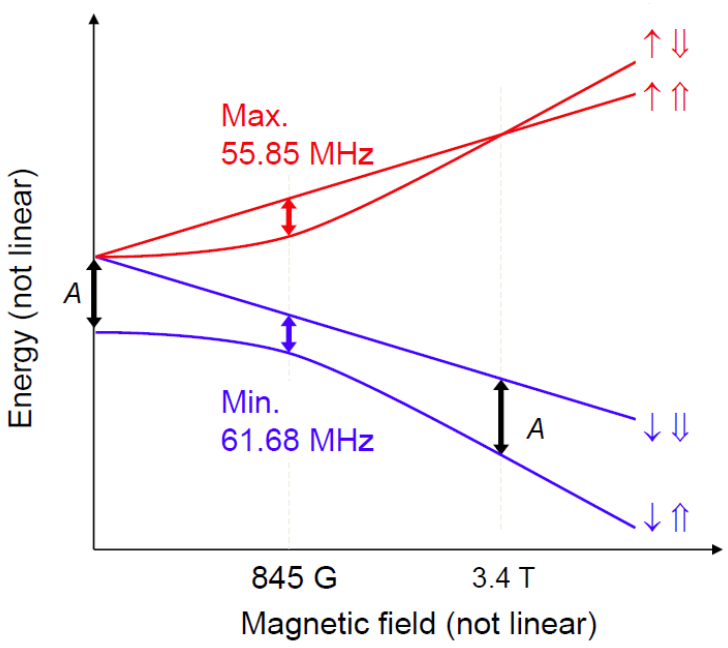

Figure 2.7: ***Schematic energy level diagram of the D^0 ground state together with characteristic magnetic fields (B_m=845G and B_c=3.4T).***

2.4.1. Magic field ("Clock Transitions") for neutral P donors in Si

In NMR, it is of particular interest that a certain magnetic field, B_{m}, gives both a maximum and a minimum for the hyperfine splitting of the up and down electron spins, ($\mathrm{RF}_{\uparrow\mathrm{max}}$ and $\mathrm{RF}_{\downarrow\mathrm{min}}$) respectively. This is an advantageous field for NMR measurements, since the effects of any inhomogeneity in the magnetic field are minimized as well as sensitivity to temporal B noise, as was recognized earlier for the analogous atomic hydrogen system [132]. The extreme point is given as $\frac{d\mathrm{RF}_{\uparrow}}{dB} = 0$, and equivalently $\frac{d\mathrm{RF}_{\downarrow}}{dB} = 0$, corresponding to NMR frequencies referred as 'clock transitions'; so we have:

$$B_m = A\,(\gamma_e - \gamma_p)/2(\gamma_e + \gamma_p)\sqrt{\gamma_e\gamma_p} = 844.91\ \mathrm{G} \tag{2.11}$$

$$\mathrm{RF}_{\uparrow\max}(B_m) \approx 55.848\ \mathrm{MHz} \tag{2.12}$$

$$\mathrm{RF}_{\downarrow\min}(B_m) \approx 61.682\ \mathrm{MHz} \tag{2.13}$$

Thus, the difference between hyperfine splittings of upper and lower branches (doublets) is smallest at this point (shown in Figure 2.8).

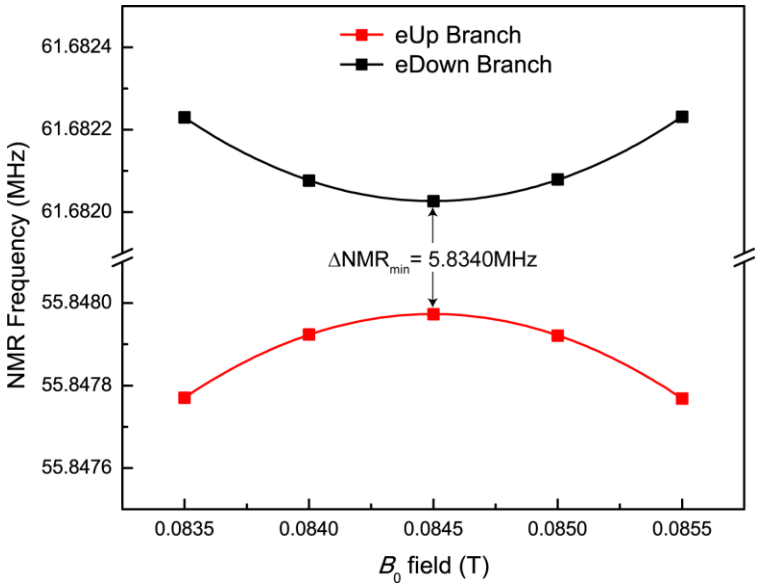

Figure 2.8: ***The two NMR resonance frequencies as a function of the applied magnetic field showing $df/dB = 0$ at B_m=0.08449 T.***

2.5. Theory of relaxation rates of P donors spins in bulk Si

In the phenomenological model of decoherence, T_1 and T_2 are known as the spin-lattice (longitudinal) and spin-spin (transverse) relaxation rates, respectively. They define important time scales for the lifetimes of non-equilibrium classical states and quantum superposition states respectively. T_1 is usually longer than T_2, since the spin-lattice relaxation is slower due to weaker dipole-dipole interaction effects. An on-resonance $(90\,°)_y$ pulse rotates a magnetization vector along the Z eigenstate into a superposition state, which can be thought of as being in the x-y plane of the Bloch

sphere. A prominent characteristic of the free induction decay (FID), the principal output of a magnetization readout experiment, is the exponential decay of the magnetization signal. One cause of this is inhomogeneity in the static magnetic field (B_0), which leads to precessing spins in one part of the sample falling out of phase with those in another part (coherence limit given by T_2^*). Effects due to inhomogeneities are, in principle reversible, but there are other sources of phase randomization which are fundamentally irreversible. For example, decoherence that originates from spin-spin couplings (T_2) and the thermalization of the spins to equilibrium (T_1).

2.5.1. T_1 decoherence time

The electron spin-lattice relaxation rates (T_{1E}) corresponding to $|\Delta m_e| = 1$ and $|\Delta m_I| = 0$ vary tremendously with field and temperature. There are three main T_{1E} relaxation processes that each dominate in different magnetic field and temperature ranges: the Orbach process (in which the electron can be excited into the next excited state by absorbing a phonon and later relax back into either the spin-up or spin-down ground state by emitting a second phonon, which indirectly allows T_{1E} relaxation), the Raman process (in which a phonon can change the electron's spin state by scattering off the electron spin via a virtual excited state), and the direct process (in which phonons with the same energy as the Zeeman splitting are directly absorbed and emitted). Each of these processes relies upon phonons that are either directly or indirectly resonant with the energy splitting of the electron. The Orbach process ($\alpha\, \mathrm{Exp}(-\Delta/T)$ where Δ is a the energy difference between ground state and next excited state) dominates above temperatures of 6 K. Like the Orbach process, the T^9 component of the Raman process ($\alpha T^9+\beta B^2 T^7$) is independent of field, concentration and orientation in the temperature range of 2.5 K - 6 K [133]. The direct process (B^4T) dominates at the lowest temperatures (below 2.5 K) where the low-energy excitations are more populated than the larger ones necessary for Raman or Orbach relaxation.

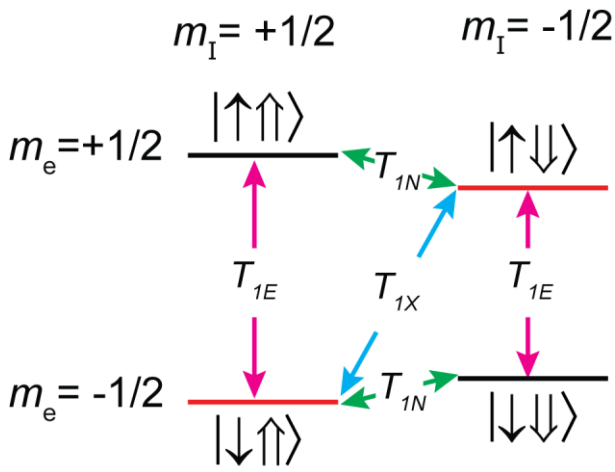

Figure 2.9: T_1 relaxation processes in our system

The nuclear relaxation rate T_{1N} corresponding to $|\Delta m_e| = 0$ and $|\Delta m_I| = 1$; and the cross relaxation rate T_{1X} corresponding to the "flip-flop" transition $\Delta m_e \Upsilon 1$, $\Delta m_I \pm 1$ differ dramatically between donors. Specifically, phosphorus donors exhibit weak cross relaxation compared to T_{1E}, whereas bismuth donors show much stronger cross relaxation compared to T_{1E} [6] . The principal difficulty in measuring T_{1X} is the long timescales involved; T_{1X} exceeds hours at low fields and temperatures.

2.5.2. T_2 decoherence time

For phosphorus, the prototypical donor in ^{28}Si, the reported electron T_2 (T_{2e}) is found to be inversely proportional to the donor density (for densities in the range from 10^{14} to 10^{16} cm^{-3}), and a similar observation has been made for the nuclear T_2 (T_{2n}) [53]. This motivates the study of coherence lifetimes at even lower donor densities; however, densities of 10^{13} cm^{-3} are at the limit of detection by conventional electron spin resonance (ESR) and electron nuclear double-resonance (ENDOR) and the signal is orders of magnitude below the threshold of standard NMR detection sensitivity. Previous conventional NMR studies of ^{31}P in Si were restricted to very heavily doped samples [134-136]. Both EPR and NMR measure ensembles by detecting small oscillating magnetic fields perpendicular to B_0. Ordinary NMR uses a solenoid that coaxially encircles the sample; coherently rotating the transverse magnetization creates

a weak field which drives a current through the coil connected to a spectrometer [131]. Such a readout pulse rotates the entire ensemble of spins at that transition frequency, both the aligned and anti-aligned spin populations, so the total transverse magnetisation is proportional to the net population difference between the two eigenstates. The optical NMR detection technique presented in this work provides information in a regime inaccessible to conventional NMR due to both the small number of spins and the low equilibrium polarization. Unlike conventional NMR, which detects the precession of the net magnetization in the transverse (x-y) plane, our optical method is sensitive only to I_z, the nuclear polarization parallel to B_0 [137].

Decoherence channels in our system

In this section, we consider common spin baths that may affect our qubits: ^{29}Si and background phosphorus donors. The random distribution of residual spin-active ^{29}Si atoms can couple through a dipolar interaction with the donor qubits to reduce T_{2E}. In a similar manner, the electrons of nearby donors can also couple to one another. In addition to reducing the concentration of ^{29}Si spins, one can also reduce the concentration of donor spins to improve the electronic lifetimes (T_{1E} *and* T_{2E},) of the donor ensemble [138] and nuclear lifetimes (T_{1n} *and* T_{2n},) of donor ensemble [54, 55]. Recently, it has been shown that the ^{29}Si bath induces decoherence through its flip-flopping dynamics, but it also suppresses donor-induced decoherence via Overhauser shifts that cause the donors to be off-resonant with each other [86]. The two types of decoherence induced by donor flip-flopping are distinguished by Tyryshkin between indirect flip flops (flip flops among bath spins) and direct flip flops (flip flops with the central spin) [53].

2.6. NMR experiments in QC to measure decoherence

The experimental methods for measuring the principal relaxation times are well-known in NMR. To measure T_1, we can apply an RF π pulse to flip the spin by 180 °, after which it relaxes exponentially with time constant τ back towards equilibrium. We can measure the T_2 coherence time using the simple Hahn echo or other more complex dynamical decoupling pulse sequences which will be described later in this section.

First, the resonance RF pulse length and frequency need to be calibrated by Rabi and Ramsey experiments respectively.

2.6.1. Rabi Oscillation

The Rabi cycle is the cyclic behaviour of a two-state quantum system in the presence of an oscillatory driving field. In the context of a nuclear magnetic resonance experiment, the Rabi frequency is the nutation frequency of a sample's net nuclear magnetization vector about a radiofrequency field (Note that this is distinct from the Larmor frequency, which characterizes the precession of a transverse nuclear magnetization about a static magnetic field.). The precise length (assuming fixed RF power) of 180 ° (π) RF pulses can be extracted from the period of Rabi Oscillations. A rotation R_y less than $(90\,°)_y$ also generates a detectable FID with an initial amplitude proportional to sin(R). If one were to record the FID amplitude while incrementing the pulse length, one would observe Rabi oscillations. This decaying sinusoid is limited by the RF pulse inhomogeneities (or B_1 inhomogeneities) across the ensemble. This will be demonstrated with examples in more detail in the Results section 4.8.1.

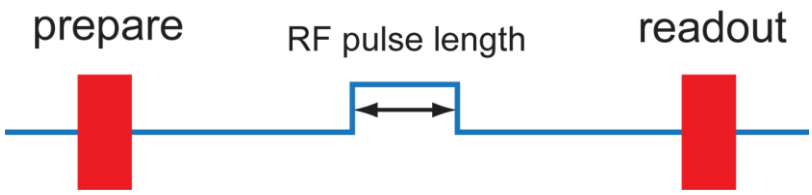

Figure 2.10: Pulse sequence of the Rabi oscillation experiment

2.6.2. Ramsey Fringes

The exact RF resonant frequency can be extracted from the applied RF frequency and the frequency of the Ramsey fringes. After determining the proper π pulse length by the Rabi experiment, the Ramsey experiment, the simplest two pulse scheme, uses two $\pi/2$ pulses, with variable separation τ, as shown in Figure 2.11. In order to obtain a clearer signature, the RF frequency was offset by several kHz from the resonant RF determined previously by CW NMR (example in the Results section). This

should result in fringes with a period of order ms as τ is scanned, and we refer to this experiment as a Ramsey fringe measurement due to the strong fringes, but in reality what is being measured is simply the FID, together with the offset between the applied RF frequency and the actual resonance frequency. The amplitude decay of these fringes shows T_2^* which is usually much shorter than T_2 and is dependent on the homogeneity of the static magnetic field. If these inhomogeneities are static on the time scale of the spin's lifetime they can be refocused with appropriate π pulses.

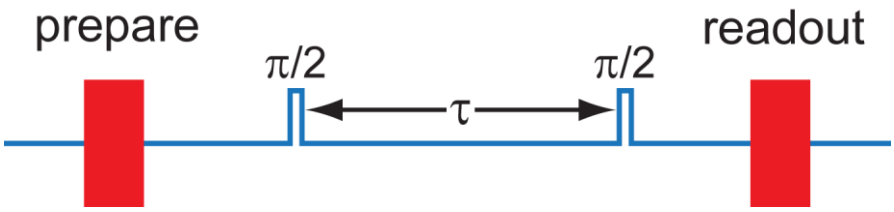

Figure 2.11: Pulse sequence of the Ramsey fringe experiment.

2.6.3. Hahn Echo (Spin-Echo)

In magnetic resonance, a spin echo is the refocusing of spin magnetisation by a pulse of resonant electromagnetic radiation. The Hahn echo experiment which is the simplest decoupling pulse sequence uses only one refocusing pulse. This refocusing technique effectively decouples the ensemble from its inhomogeneous environment, and is essential for maintaining long-term coherent control of an ensemble of spins. A visual representation of this refocusing technique is shown in Figure 2.12. The vertical arrow (on top of Figure 2.12 shown inside the Bloch sphere) is the average magnetic moment of a group of spins, such as electrons or nuclei after polarization. All are vertical in the vertical magnetic field and spinning on their long axis, but this illustration is in a rotating reference frame where the spins are stationary on average.

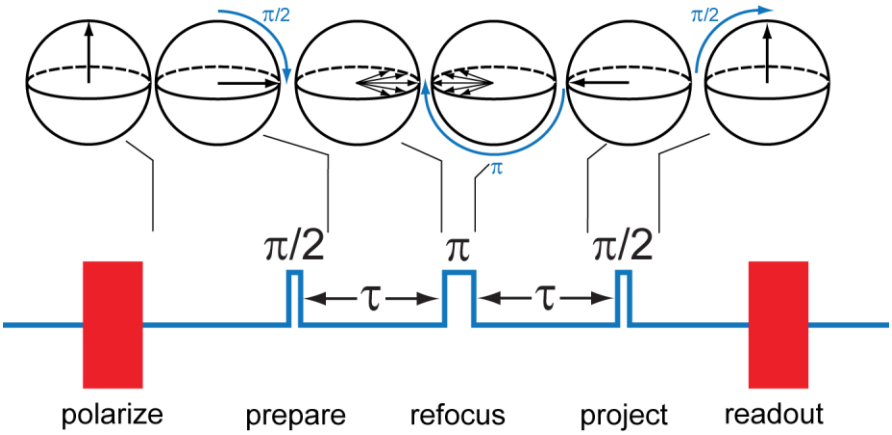

Figure 2.12: ***Pulse sequence of Hahn Echo experiment along with an illustration of the spins on the Bloch sphere at different stages of the sequence.***

A 90 degree ($\pi/2$) pulse has been applied that flips the arrow into the horizontal (x-y) plane. Due to local magnetic field inhomogeneities (variations in the magnetic field at different parts of the sample that are constant in time), as the net moment precesses, some spins slow down due to lower local field strength (and so begin to progressively trail behind) while some speed up due to higher field strength and start getting ahead of the others. This makes the signal decay. A 180 degree (π) pulse is now applied so that the slower spins lead ahead of the main moment and the fast ones trail behind. Progressively, the fast moments catch up with the main moment and the slow moments drift back toward the main moment. The projection pulse is necessary for our projective readout method which can only measure one particular phase of the echo for each shot. This is unlike standard magnetic resonance experiments where both the in-phase and quadrature echo signals (X and Y) can be captured simultaneously. The amplitude recovery of this sequence is ultimately limited by decoherence of the spin T_2. In this way, τ can be extended to measure the timescale of decoherence of the system. The decay of the Hahn echo signal is a lower bound for the true T_2 of an individual spin; magnetic field fluctuations during the sequence can lead to shorter ensemble decay times.

2.6.4. Other dynamical decoupling pulse sequences

Maintaining a stable magnetic environment for times on the order of seconds is challenging. Often a simple Hahn Echo sequence is less effective than other similar dynamical decoupling pulse sequences which apply refocusing pulses on shorter time intervals. Examples of members of this class of decoupling sequences are Carr-Purcell (CP), Carr-Purcell-Meiboom-Gill (CPMG) and $(XY)^n$ sequences (shown in Figure 2.13) [139], which use repeated combinations of $\{\pi_x, \pi_y\}$ pulses to refocus spins over time intervals shorter than the correlation time of the field fluctuations. Of course the natural concern for such repetitive sequences is the stimulated echoes [140] they generate; the "long tails" give rise to overly optimistic T_2 times [6].

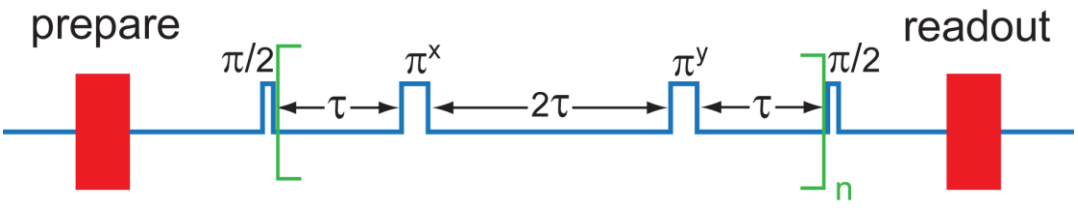

Figure 2.13: Pulse sequence of the XY decoupling experiment.

The most significant error present in a single-qubit operation is in the rotation angle, arising from spatial inhomogeneity in the pulsed RF field. Fortunately, a number of approaches to tackling different classes of systematic errors have been developed in the art of NMR, employing composite rotation sequences [141-143]. Among them, pulses sequences known as $XY16 = XYXYYXYX\overline{XYXYYXYX}$ and XY16-BB1, which has the five-pulse composite rotation known as BB1 for minimizing error in the rotation angle [144], were found to be the most effective for our system and they have been used in this thesis to produce extremely long coherence times. The reason behind choosing these specific pulse sequences is that they preserve the coherence of the system independent of the input state, unlike CP or CPMG. Protecting the dynamics of coupled quantum systems from decoherence due to the environment is a key challenge for solid-state quantum information processing [145, 146].

3. Materials, Methods and Apparatus

This chapter presents details about the samples and the experimental setup. The first section discusses the materials used to prepare the samples and explains the process of sample preparation. This is followed by a section giving an overview of photoluminescence (PL), photoluminescence excitation (PLE) and photoconductive (PC) spectroscopy of the donor bound exciton (D^0X). This section also describes in detail the version of optically detected magnetic resonance that we refer to as Auger-electron-detected magnetic resonance (AEDMR) including initialization, manipulation and the readout mechanism for neutral and ionized ^{31}P in ^{28}Si. This ends with an explanation of the experimental setup and technical means used to carry out the optical NMR experiments at constant cryogenic temperature and also at variable temperatures up to room temperature.

3.1. Materials

Semiconductors like silicon are some of the purest materials known to man, with concentrations of most impurities of less than 1 part per billion (1 ppb), so it is useful to know the common techniques for growing such materials. Two main growth techniques for crystalline silicon are known as the Czochralski (CZ) and Float Zone (FZ) methods. The advantage of the FZ method over the CZ method, which is commonly used in the electronics industry for growing large silicon single crystals, is that in the FZ method, the absence of a container used to hold the polysilicon melt results in single crystals of much higher chemical purity [147]. The lower concentrations of carbon and oxygen are especially important in the optical spectroscopy of silicon, as high concentrations of these impurities have been shown to severely broaden optical transitions [148].

The main samples used in the present study and called Avogadro samples (refered to as ^{28}Si-Avo), were provided by the group involved with International Avogadro

Project[7] [149]. The isotopically enriched ^{28}Si crystal was produced from isotopically purified silane gas ($^{28}SiH_4$) which was initially enriched by centrifuge in St Petersburg, Russia and then used to grow high purity polycrystalline silicon. The polysilicon was converted to single crystal silicon using the FZ method in Berlin, Germany. A polysilicon rod is mounted inside a growth chamber which is under vacuum or purged with an inert gas such as Ar. A RF heating coil melts a narrow region of the polysilicon rod, establishing a liquid molten zone. To start the growth, the ^{28}Si seed crystal at the bottom of the growth chamber is moved up to make contact with the molten silicon, and a necking process is carried out to establish dislocation-free growth before the boule is allowed to increase in diameter. The shape of the molten zone and the diameter of the boule are adjusted by changing the RF power of the coil and the travel speed, and are monitored by infrared sensors [150].

3.1.1. Isotopically purified ^{28}Si Samples

The ^{28}Si-Avo sample, which is p-type with a higher concentration of the shallow acceptor boron than of the shallow donor phosphorus, is currently the most isotopically and chemically pure ^{28}Si sample available. It is enriched to 99.995% ^{28}Si, and contains 46 ppm ^{29}Si (2.3×10^{18} cm^{-3}), less than 10^{13} cm^{-3} oxygen and less than 10^{14} cm^{-3} carbon (detection limit). The n-type ^{28}Si:P 3.3.X (x=1 to 9) samples, which were specifically grown for the experiments in this lab, were produced from the same 99.995% enriched ^{28}Si used to grow p-type ^{28}Si samples, except were intentionally doped with phosphorus by introducing a dilute mixture of phosphine gas (PH_3) in Ar carrier gas to the growth chamber during the final floating zone growth of the dislocation free single crystal. The resulting crystal had a gradient in ^{31}P concentration, but the results presented in this project for n-type ^{28}Si:P were obtained only from the 3.3.2 and 3.3.6 slices. The samples used for the experiments presented in this study are listed in Table 3.1, along with their phosphorus and boron concentrations as measured by the photoluminescence spectroscopy method (example in the Results chapter, section 4.1). This is a standard

[7] An approach for redefinition of the mass SI unit, Kilogram, by accurate determination of Avogadro constant.

technique for the determination of shallow donor and acceptor concentrations in silicon [100, 151-154].

Table 3.1: ***^{28}Si samples used in this study are listed with their ^{31}P and B concentration.***

Sample name	n/p type	^{31}P Concentration (cm^{-3})	B Concentration (cm^{-3})
^{28}Si Avo	p-type	5 x 10^{11}	5 x 10^{13}
^{28}Si:P 3.3.2	n-type	3 x 10^{14}	7 x 10^{13}
^{28}Si:P 3.3.6	n-type	7 x 10^{14}	4 x 10^{13}

The samples listed in Table 3.1 and shown in the Figure 3.1, came from single crystal boules grown along the [001] direction, which were later cut into disks with (001) faces, with the exception of the ^{28}Si-Avo sample, which is a quarter disk cut from segment Si28-10Pr11.02.2 taken from the seed end of the Avogadro crystal [109]. Later, two different size samples, named small ^{28}Si-Avo (11.8 x 4.5 x 1.7 mm^3) and very small ^{28}Si-Avo (5 x 4.7 x 1.7 mm^3) were cut from the ^{28}Si-Avo sample for specific (constant cryogenic temperature and temperature ramp) experiments in this study. The n-type ^{28}Si:P sample discs (3.3.2 and 3.3.6) are approximately 1 cm in diameter and 1 to 1.5 mm thick.

3.1.2. Sample preparation

The samples are usually received with as-cut surfaces, and often need to be recut into smaller pieces before use. The surface damage from saw cutting strains the sample, and this surface damage has to be removed before high resolution spectroscopy is possible. The sample was held by Crystalbond adhesive for cutting, was washed repeatedly in acetone to dissolve the adhesive and organic contamination, then washed in methanol and finally rinsed with distilled water. In the next step, the sample must be chemically etched in a 1 part hydrofluoric acid (HF) in 10 part nitric acid (HNO_3) solution usually for ~1 minute in a fume hood to remove the oxide layer and any surface damage which would otherwise strain the sample and consequently could split and broaden the optical transitions.

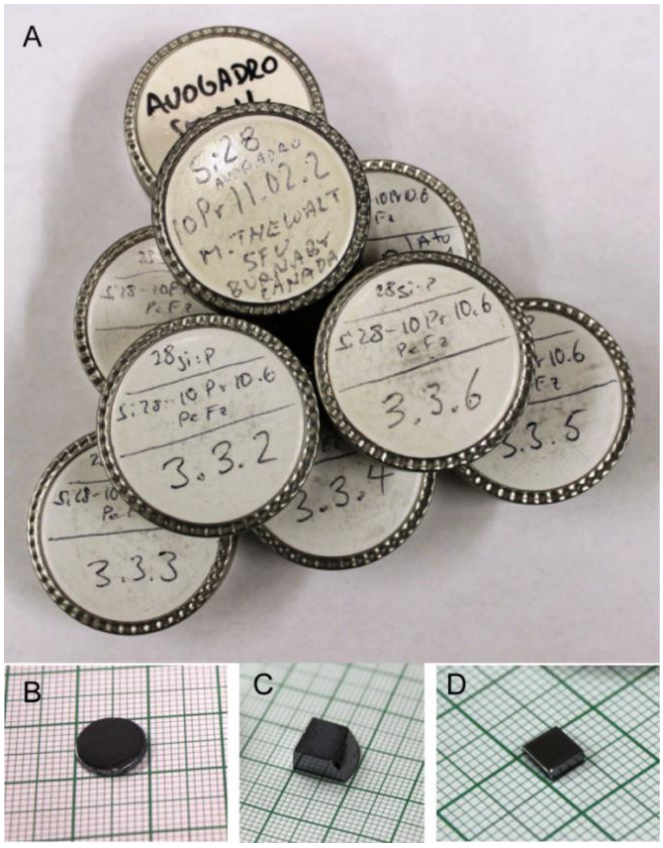

Figure 3.1: ***(A) Some of the samples used for this research project. (B) A ^{28}Si:P 3.3.x disc after P doping, (C) a quarter piece of a disc ^{28}Si-avo, (D) a ^{28}Si small piece cut from ^{28}Si-Avo original sample for the NMR experiment.***

3.2. PL, PLE and PC spectroscopy method

Photoluminescence (PL) is a process in which a substance absorbs photons and then re-radiates photons. Quantum mechanically, this can be described as an excitation of an electron to a higher permissible energy state (excited state) and then a return to a lower energy state (ground state) which may be accompanied by the emission of a photon (a radiative process) or may not (a nonradiative process).

PL spectroscopy is of great significance in fields of analysis of semiconductors because it is a contactless, non-destructive method of probing the electronic structure,

the purity and crystalline quality of semiconductors. In this study, a Bomem DA8 Fourier transform spectrometer [155] was used with a quartz beam splitter to obtain the PL spectra. The instrumental resolution of our Fourier transform PL apparatus, having the highest resolution available in the spectral region of any commercially available system, is ~ 0.0024 cm^{-1} = 0.3μeV (see [155] for more detail). In order to achieve even higher resolution, the photoluminescence excitation (PLE) spectroscopy, using a tunable single-frequency laser source with sub-MHz linewidth, capable of providing a significant increase in resolution (~0.4 neV) was demonstrated in a previous study [93] to resolve the hyperfine states of D^0.

In PLE spectroscopy, unlike PL spectroscopy where above band gap excitation is used to generate free excitons (FEs) which in turn form bound excitons (BEs), a resonant laser source is scanned across the no-phonon BE transitions, and the very weak absorption in which BEs are created in their ground state. The resulting recombination and subsequent photon emission is then observed by detecting the relatively strong corresponding TO phonon assisted transition, which is well separated in energy from the no-phonon region [93]. In other words, in the PLE method, the transition is studied in absorption rather than in emission.

Figure 3.2 shows schematic of the D^0 and D^0X ground states, together with their Zeeman splittings for the case of B || [001], including the hyperfine splitting of the D^0 ground state resulting from the I = ½ nuclear spin but ignoring the negligible nuclear Zeeman energy in the D^0X states. Note that the bare nuclear Zeeman energies are small at these low fields, and the contact hyperfine interaction with the D^0X hole is vanishingly small. Figure 3.2 also shows the 12 dipole-allowed transitions between the four D^0 hyperfine states and the four D^0X states are labeled from 1 to 12 in order of increasing energy. Our PLE measurements are essentially absorption measurements, connecting D^0 initial states and D^0X final states, so the relative intensities give directly the relative populations in the four D^0 hyperfine states when comparing transitions having the same selection rules, such as for example lines 5, 6, 7, and 8 [137].

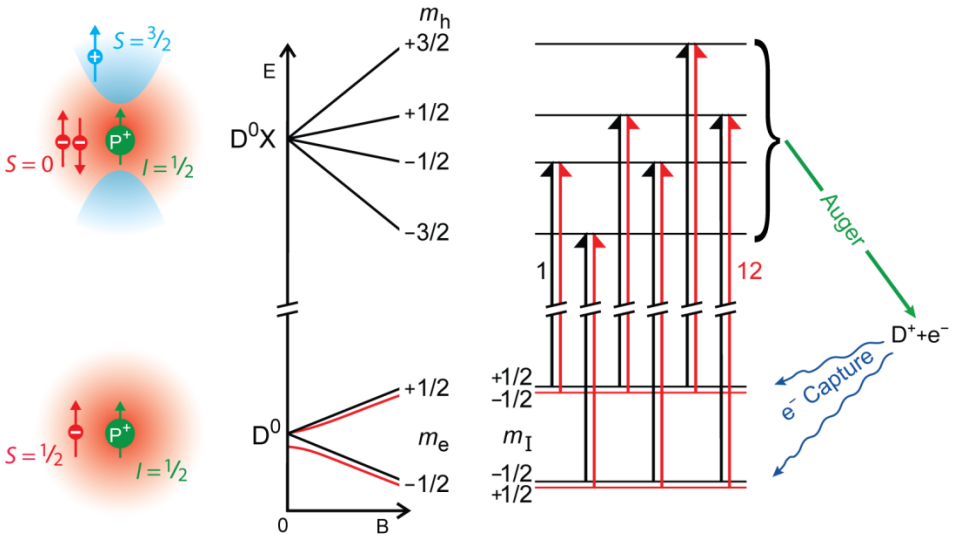

Figure 3.2: ***The ground states of the phosphorus D^0X and D^0 and their splittings under a magnetic field, showing the origin of the 12 dipole-allowed absorption transitions, labeled from 1 to 12 in order of increasing energy.***

The D^0X in indirect-gap semiconductors such as Si have a property that is usually considered disadvantageous but that is central to our PC methods. The indirect band gap results in long radiative lifetimes, and D^0X recombination is dominated by nonradiative Auger decay, in which D^0X decay to ionized donors (D^+) and energetic free electrons (e^-), which are eventually recaptured to return D^+ to D^0. This results in very low luminescence quantum efficiencies, ~10^{-4} for the phosphorus D^0X (i.e. every 10,000 D^0X decays give one photon and 9,999 free electrons as a result of Auger recombination), limiting the use of luminescence to monitor the D^0X population as done in our previous studies [62, 65, 137]. However, we can instead detect the electrons produced with ~100% (near unity) efficiency by the Auger decay process [103] to monitor the resonant creation of D^0X by measuring the capacitance change of the sample in the middle of parallel plate capacitor (photoconductive method).

3.3. The optical NMR technique for D^0 and D^+ experiments

In the next three subsections we describe in more detail the stages of the Hahn Echo experiments for neutral and ionized ^{31}P donors (D^0 and D^+). We combined hyperpolarization (subsection 3.3.1), coherent manipulation of the nuclear spin (subsection 3.3.2), and readout (subsection 3.3.3) by AEDMR to make measurements of coherence times (T_{1n}, T_{2n} and T_{2n}^*).

3.3.1. Preparation / Initialization (Hyperpolarization schemes)

In the context of ensemble quantum computing, the purity of the initial state is often the principal corrupting contribution to the result of a quantum algorithm. Identifying and understanding hyperpolarization schemes for donors in silicon is therefore of fundamental computational interest. There are a number of known methods for hyperpolarizing donors in silicon using indirect processes, which exploit the asymmetry in cross relaxation strengths. These schemes often fall under the broader category of dynamic nuclear polarization (DNP), which was first identified by Overhauser in 1953 [156]. DNP results from transferring spin polarization from electrons to nuclei, thereby aligning the nuclear spins to the extent that electron spins are aligned; so most of the DNP demonstrations in ^{28}Si:P have been performed in a regime of high electronic polarization (either at low temperatures, high magnetic fields or both). The upper bound for this class of processes is where the nuclei attain the initial polarization of the electrons which is, however, very small at our low magnetic fields. An alternative method which drives spin-dependent bound exciton transitions relies upon selective ionisation and relaxation to attain a high degree of nuclear polarization (see Fig. 3.3); this process is independent of the electron's initial polarization. This significantly faster optical hyperpolarization process makes use of the very narrow optical linewidths of ^{28}Si:P to achieve selective excitation of the donor ground state into a BE state [65]. The BE is generally short-lived; one of the two electrons quickly recombines with the hole and the other electron is excited into the conduction band (Auger decay). After the ionised donor recaptures a spin-up or spin-down electron the cycle is complete. This cycle effectively removes electrons from systems with a given spin orientation and substitutes an electron spin with a random spin state.

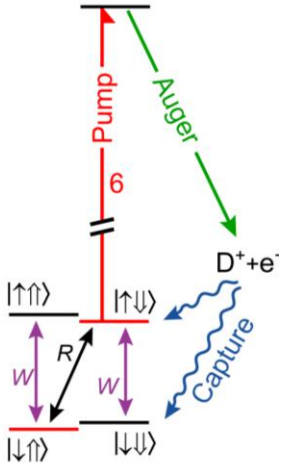

Figure 3.3: ***Schematic of the original selective optical polarization mechanism with only the pump laser tuned to line 6. R and W label relaxation processes [65] and the |↓⇓⟩ state is the most populated state after this selective polarization process.***

In the original hyperpolarization schemes as outlined in the Figure 3.3, with only the high power polarizing laser tuned to line 6, the Auger process ionizes donors in state $|\uparrow\Downarrow\rangle$, with some of the thermalized electrons being recaptured with opposite spin into $|\downarrow\Downarrow\rangle$. The D^0 in $|\uparrow\Uparrow\rangle$ and $|\downarrow\Uparrow\rangle$ transfer via the "W" and "R" relaxation processes [65], which are very slow in the dark but more rapid in the presence of free carriers, to $|\uparrow\Downarrow\rangle$ where they are rapidly ionized; so $|\downarrow\Downarrow\rangle$ state is primarily populated after this process has finished. Nuclear polarizations of up to 76% for n-type material have been observed after 1 second of illumination at low fields (0.043 T) and low temperatures (1.4 K) [65].

In a p-type sample (^{28}Si-Avo) in equilibrium at cryogenic temperature, one expects all the donors to be D^+ and an equal number of acceptors to also be ionized (A^-), making resonant D^0X creation impossible. Weak above-gap radiation, here supplied by a 1047-nm laser, generates a sufficient concentration of electrons and holes to photoneutralize the D^+ and A^-. The necessity of having above-gap excitation at 1047 nm to achieve donor photoneutralization in the p-type sample required changes to the previous method of donor hyperpolarization [65], which was used in the preliminary study of optically hyperpolarized/detected NMR of ^{31}P in n-type ^{28}Si [137].

Figure 3.4 shows the improved hyperpolarization scheme for the specific case of a high-power polarizing laser on line 6, which has the effect of pumping D^0 from state $|\uparrow\Downarrow\rangle$ to state $|\downarrow\Downarrow\rangle$ (the D^0X ionizes with near-unity probability, and some of the thermalized electrons are recaptured with opposite spin into $|\downarrow\Downarrow\rangle$). We simultaneously applied an NMR field $RF_{\uparrow}$, such that D^0 in $|\uparrow\Uparrow\rangle$ were pumped to $|\uparrow\Downarrow\rangle$, as well as a low-power "readout" laser tuned to line 4, pumping population from $|\downarrow\Uparrow\rangle$ to $|\uparrow\Uparrow\rangle$ (this could also be achieved by applying a microwave field at the $|\downarrow\Uparrow\rangle \leftrightarrow |\uparrow\Uparrow\rangle$ energy). The result is that the D^0 population is pumped into state $|\downarrow\Downarrow\rangle$, where both electron and nuclear spin are in the spin-down state.

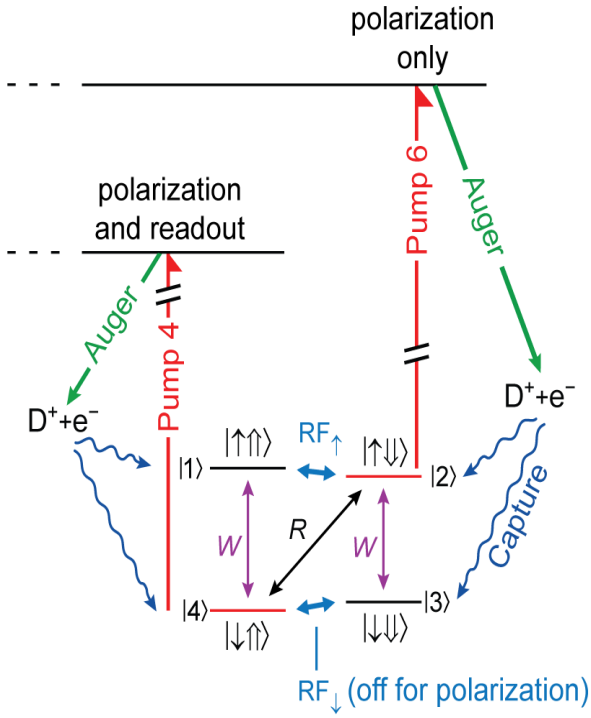

Figure 3.4: ***The improved hyperpolarization scheme used here polarizes D^0 into the hyperfine state $|\downarrow\Downarrow\rangle$, with polarizing laser on line 6, readout laser on line 4, and RF applied at $RF_{\uparrow}$.***

This fast and efficient hyperpolarization scheme based on combination of optical pumping and RF provides an initialization mechanism for these spin qubits (details on the amounts of electron and nuclear polarization will be presented in the Results section 4.5).

3.3.2. *Manipulation*

For the case of neutral ^{31}P donors (D^0) as shown in Figure 3.5, the 500-ms polarizing stage hyperpolarizes the system into state $|\downarrow\Downarrow\rangle$ ($|3\rangle$) (see Fig. 3.4), with magnetization in the +Z direction. The NMR manipulation occurs in the dark (no laser present) and begins with a $\pi/2$ preparation pulse, which rotates the initial polarization into the XY plane. After the τ-π-τ Hahn refocusing sequence, a second $\pi/2$ pulse projects the remaining coherent magnetization back into the Z direction for readout. All RF pulses are of the same phase (nominally X). If the nuclear spin has remained coherent, all population is returned to state $|\downarrow\Downarrow\rangle$ ($|3\rangle$); otherwise it becomes equally (and incoherently) distributed between states $|\downarrow\Downarrow\rangle$ ($|3\rangle$) and $|\downarrow\Uparrow\rangle$ ($|4\rangle$). The 1047-nm laser and then the readout laser are turned on, generating a photoconductive transient with area proportional to the population in $|\downarrow\Uparrow\rangle$ ($|4\rangle$). A π pulse then swaps the $|\downarrow\Uparrow\rangle$ ($|4\rangle$) and $|\downarrow\Downarrow\rangle$ ($|3\rangle$) populations, producing a second photoconductive transient proportional to the population previously in $|\downarrow\Downarrow\rangle$ ($|3\rangle$). The readout stage therefore measures the difference between the areas of the $|\downarrow\Downarrow\rangle$ ($|3\rangle$) and $|\downarrow\Uparrow\rangle$ ($|4\rangle$) photoconductive transients.

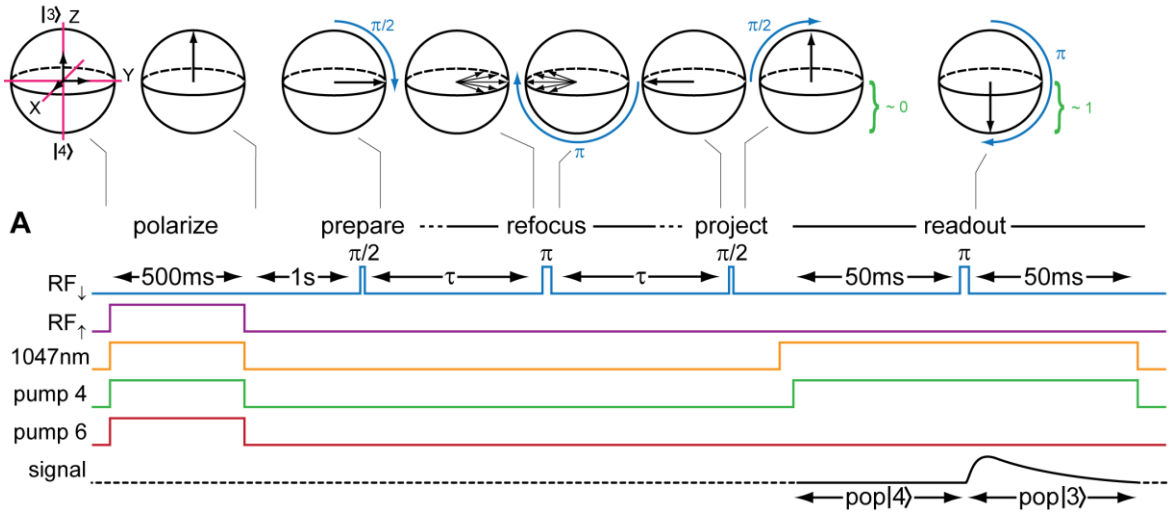

Figure 3.5: ***The optical and RF pulse sequence for a Hahn echo measurement of neutral P (D^0) including hyperpolarization and readout pulse sequence protocols.***

Figure 3.6, the modified version of Fig. 3.4, shows the optical and NMR transitions used to hyperpolarize the nuclear spins (to $|\downarrow\Downarrow\rangle$ state using lines 4, 6 and $RF_{\uparrow}$), fully ionize the donors (to $|\Uparrow\rangle$ state using line 4), coherently manipulate the ionized donors (D^{+}) nuclear spin (by RF^{+}), reneutralize the D^{+} donors (using 1047-nm shown by blue arrows in Fig. 3.6), and read out the resulting spin populations (using both lines 4 and 5).

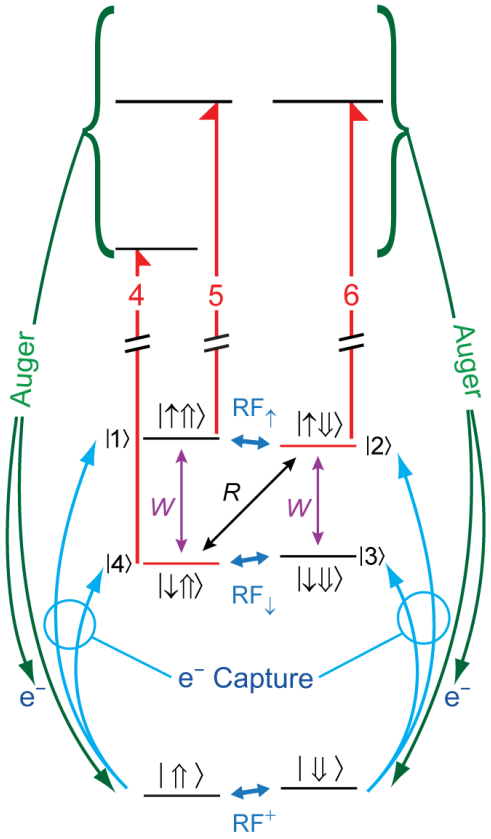

Figure 3.6: ***The specific optical transitions (lines 4, 5, and 6) and nuclear magnetic resonance transitions ($RF_{\uparrow}$, $RF_{\downarrow}$, and RF^{+}) used here to hyperpolarize, manipulate, and read out the nuclear spins for ionized donors. The magnitude of the D^{+} Zeeman splitting (RF^{+}) has been exaggerated to show the ordering of the D^{+} states. Although the energy differences between the D^{0} and $D^{0}X$ levels are precisely fixed in ^{28}Si, the D^{+} energy is not well defined because of the kinetic energy of the e^{-}.***

For the study of D^+ as shown in the Figure 3.7, with reference to the transitions shown in Figure 3.6, step {1} hyperpolarizes the donor nuclear spins (the same process used previously for the study of neutral ^{31}P). The 500-ms hyperpolarization time is much longer than what is required to obtain a good polarization, but is kept long so as to remove all history of the previous state of the sample. The 1047-nm laser is on to photoneutralize the donors, and the laser on line 6 quickly converts D^0 in state $|\uparrow\Downarrow\rangle$ into D^0X, which Auger ionize to give e^- and D^+ in state $|\Downarrow\rangle$. Electron capture produces either $|\uparrow\Downarrow\rangle$ or $|\downarrow\Downarrow\rangle$, resulting in a buildup of population in $|\downarrow\Downarrow\rangle$. In a similar way, the laser on line 4 moves population from $|\downarrow\Uparrow\rangle$ to $|\uparrow\Uparrow\rangle$, and $RF_\uparrow$ flips the nuclear spin, moving population from $|\uparrow\Uparrow\rangle$ to $|\uparrow\Downarrow\rangle$, where it is quickly ionized by the laser on line 6. At the end of step {1}, almost all of the donors are either in state $|\downarrow\Downarrow\rangle$ or state $|\Downarrow\rangle$. Since there is no laser tuned to ionize $|\downarrow\Downarrow\rangle$, we instead flip $|\Downarrow\rangle$ to $|\Uparrow\rangle$ in step {2}, $|\downarrow\Downarrow\rangle$ to $|\downarrow\Uparrow\rangle$ in step {3}, and then use the laser on line 4 to ionize $|\downarrow\Uparrow\rangle$ to $|\Uparrow\rangle$ in step {4}. By step {5} we estimate that over 90% of the donors are both ionized and polarized into state $|\Uparrow\rangle$, based on our inability to observe any NMR response above the noise level from the other states.

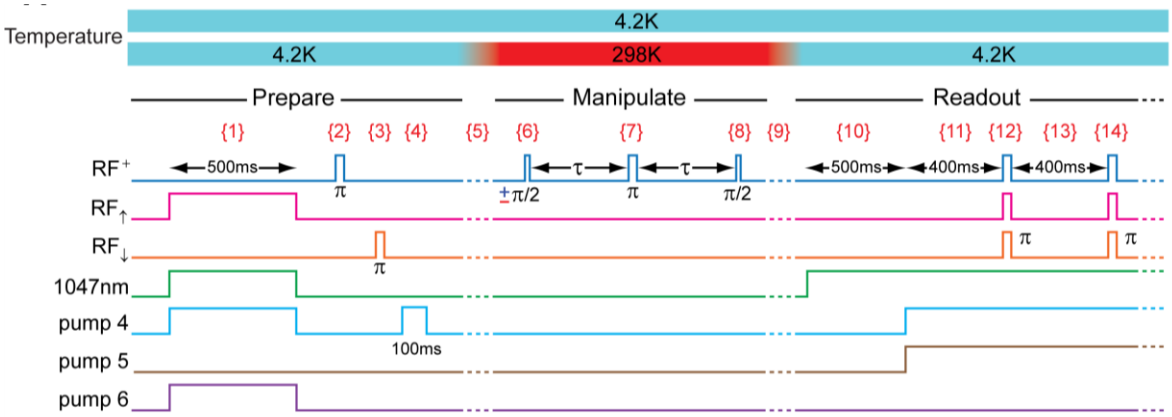

Figure 3.7: ***The laser and RF sequences used to prepare D^+ in the $|\Uparrow\rangle$ state (steps {1} to {4}), manipulation of D^+ spins for the case of a Hahn echo ({6} to {8}), and readout of the resulting Z component ({10} to {14}…). At the top are the two temperature profiles: either a constant temperature ≤4.2 K or 4.2 K during preparation and readout, with a ramp up to 298 K taking ~6min {5}, a constant 298K during the D^+ manipulation period, and a ramp down to 4.2 K taking ~4 min {9}. Each measurement was performed twice, with opposite signs of the initial $\pi/2$ pulse {6}.***

The manipulation section ({6} to{8}) of Figure 3.7 shows a simple Hahn echo sequence, where the $+\pi/2$ pulse at step {6} places the system in a coherent superposition with nominal phase X, the π pulse at {7} refocuses any constant dephasing, and the $\pi/2$ pulse at {8} projects the remaining coherence into a $|\Downarrow\rangle$ population. This is repeated with a $-\pi/2$ pulse at {6}, resulting in a $|\Uparrow\rangle$ population after projection at {8}, so that a difference measurement can be made between the readouts generated by the two phase-cycled initial states.

For T_1 measurements, the π pulse of the Hahn echo sequence (step {7}) is removed and the two $\pi/2$ pulses (steps {6} and {8}) are placed close together in time, with the evolution of the system occurring after these pulses, between steps {8} and {9}. For the $+\pi/2$ pulse at step {6} this is equivalent to a $+\pi$ pulse, leaving the system in state $|\Downarrow\rangle$ at the end of step {8}, while for the $-\pi/2$ pulse at {6} it is equivalent to no operation, leaving the system in state $|\Uparrow\rangle$ after step {8}, again allowing for a difference measurement after the two readouts. The Ramsey fringe measurement to determine T_2^* is very similar to the T_1 measurement, but the time evolution occurs between the two $\pi/2$ pulses, and the RF frequency is offset from the actual resonance frequency by a known amount in order to produce fringes with a suitable period.

We used two different temperature profiles to measure T_1 and T_2, as shown above Figure 3.7; either a fixed temperature at or below 4.2 K, or at room temperature (298 K), with the polarization and readout steps at 4.2 K. The measurement RF pulse sequence is shown for a simple Hahn echo ($\pi/2 - \pi - \pi/2$). The temperature is changed only while the D^+ nuclear spin is in an eigenstate in the Z basis (i.e., in the $|\Downarrow\rangle$ or $|\Uparrow\rangle$ state). This ensures that the nuclear spin is sensitive only to T_1 relaxation processes while the temperature is changing. Later we explored a third profile, changing the temperature while the nuclear spin was in a superposition state.

The Hahn echo sequence can only refocus the effects of inhomogeneities which are essentially static, and longer coherence times can be obtained using periodic refocusing, or dynamic decoupling, with a series of π pulses which can eliminate the effects of low frequency noise and drift [157, 158]. We have shown that a repeated, relatively simple series of $\pm\pi$ rotations around the X and Y axes, known as XY-16 [159],

is remarkably resistant to degradation due to pulse errors, and can protect an arbitrary coherent initial state against decay [54]. For all the results shown here the delay between the π pulses in the XY-16 sequence was 8 ms (more detail in the Results chapter, section 4.10).

3.3.3. Readout

At a temperature of 4.2 K (or below in the case of the all-cryogenic measurements), the ionized donors are neutralized in step {10} of Figure 3.7, but the neutralizing electrons have negligible polarization, so for example $|\Uparrow\rangle$ polarized D^+ would result in equal $|\downarrow\Uparrow\rangle$ and $|\uparrow\Uparrow\rangle$ populations. Our original readout scheme [54] for studying D^0 was optimized for measuring the population of a single hyperfine state, and therefore only reads out half the polarized D^+ after neutralization. The previous readout scheme, shown in the Figure 3.4 and 3.5, also suffers from strong transients, since the readout laser on line 4 moves population from $|\downarrow\Uparrow\rangle$ to $|\uparrow\Uparrow\rangle$ during step {11}, and again after the single π pulse at $RF_{\downarrow}$ (step {12}), moves population from $|\downarrow\Downarrow\rangle$ to $|\downarrow\Uparrow\rangle$ during step {13}. We have improved on this scheme, shown in the Figure 3.6 and 3.7, for these D^+ studies by adding a readout laser on line 5, so that both the $|\downarrow\Uparrow\rangle$ and $|\uparrow\Uparrow\rangle$ populations are read out simultaneously, doubling the signal and eliminating the transients. Also, since the electron state of individual donors is arbitrary during the readout in our new scheme, π pulses at all three NMR frequencies are applied at step {12} to flip all ^{31}P nuclear spins.

Maximum magnitude detection

When using a simple Hahn echo pulse sequence, a problem known as phase noise often appears at long delay times. This occurs because either the RF frequency or the B_0 field varies between the first half and the second half of the Hahn echo sequence, so that the phase of the nuclear spin echo becomes uncorrelated with the RF phase at readout. In standard magnetic resonance experiments this can be easily remedied, since both the in-phase and quadrature echo signals (X and Y) can be captured simultaneously, allowing an echo magnitude to be calculated [53]. Our projective readout can only measure one particular phase of the echo for each shot, precluding this approach. However, even with a completely random phase, the absolute value of the projective readout will be within 98% of the maximum possible echo signal

for 10% of the readouts. We implement this by taking 40 measurements at each delay and averaging the 4 largest absolute values to obtain our echo strength. This method is not needed when using decoupling sequences such as XY16, which minimized the effects of slow drifts in the NMR frequency.

3.4. Experimental apparatus

A schematic of the apparatus is shown in Figure 3.8. We begin by describing those components which are common to both the constant cryogenic temperature and temperature-ramp experiments, paying particular attention to improvements which have been made to the apparatus used for D^0 measurements [54, 137]. Then, the discussion of the temperature ramping apparatus will conclude this chapter.

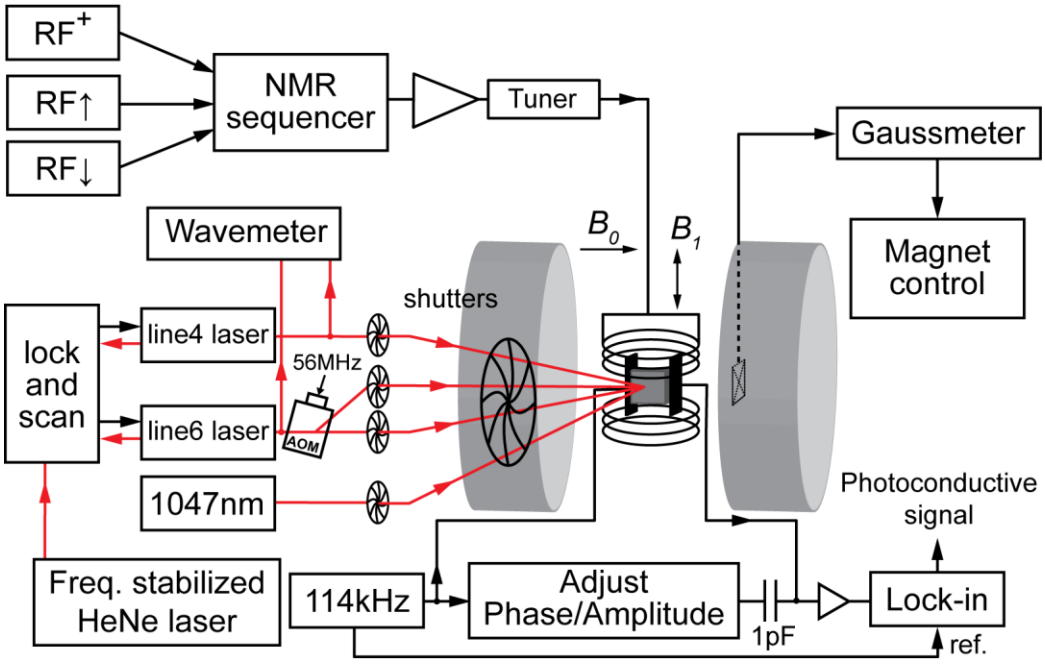

Figure 3.8: ***A block diagram of the experimental apparatus. A schematic of the hyperfine-resolved optical hyperpolarization and photoconductive readout apparatus used to detect NMR of dilute ^{31}P in highly enriched ^{28}Si. The electromagnet system used for the constant temperature cryogenic experiments is shown.***

The three main parts of an optical NMR system are the sample, the NMR spectrometer, and readout data collection as shown in Figure 3.8 which will be described in detail in the following subsections. The spectrometer itself consists of RF electronics, which is made of the computer controlled direct digital synthesis (DDS) board used as a NMR pulse generator/sequencer, switch and amplifier, RF coil, matching and tuning circuits, the optical excitation sources plus shutters, and a magnet in which static z oriented B_0 magnetic field is carefully trimmed by shimming the magnet poles to be uniform over the sample volume. An orthogonal Helmholtz or solenoid coil lying in the transverse plane allows small, oscillating B_1 magnetic fields (RF pulses) to be applied along the perpendicular to B_0 in order to manipulate the nuclear spin states.

Here is the place where the difference between our version of NMR and ordinary NMR becomes clear. In the ordinary NMR experiment, the same coil is also part of the tuned circuit which is used to pick up the RF signal generated by the precessing nuclear spin (much like how a spinning magnet inductively generates an alternating current in a nearby coil). In our NMR method, the effect on the state of the nuclei will be measured through the change in conductivity of sample during the specific excitation condition.

3.4.1. Sample holders and RF electronics

Figure 3.9 shows how the samples were mounted in different sample holders for specific experiments. In the sample holder (as seen in Figure 3.9 A) of our preliminary NMR with n-type ^{28}Si:P, a slot was cut into the plastic to accommodate the sample and, then covered by thick piece of glass, through which the excitation and PL emission take place. The samples were loosely held in the cavities, with their own weight being the only force on them to avoid any mechanical strain, in the center of a copper coil which can be tuned and matched to present a 50 Ω load at either RF frequency. The RF field was perpendicular to the static field and parallel to the direction of laser excitation and PL detection. Figure 3.9 B shows alternative RF coil configuration (Helmholtz) for better B_1 field homogeneity and to accommodate contacts for capacitive PC measurement for the p-type samples (typical photoconductivity measurement arrangement is shown in Figure 3.9 C). Finally, our more complex sample holder (Figure 3.9 D) for the temperature ramp experiment includes heater, sensors and mini glass Dewar which

thermally isolates coils from the sample/ heater (schematic illustrated in detail in section 3.4.5).

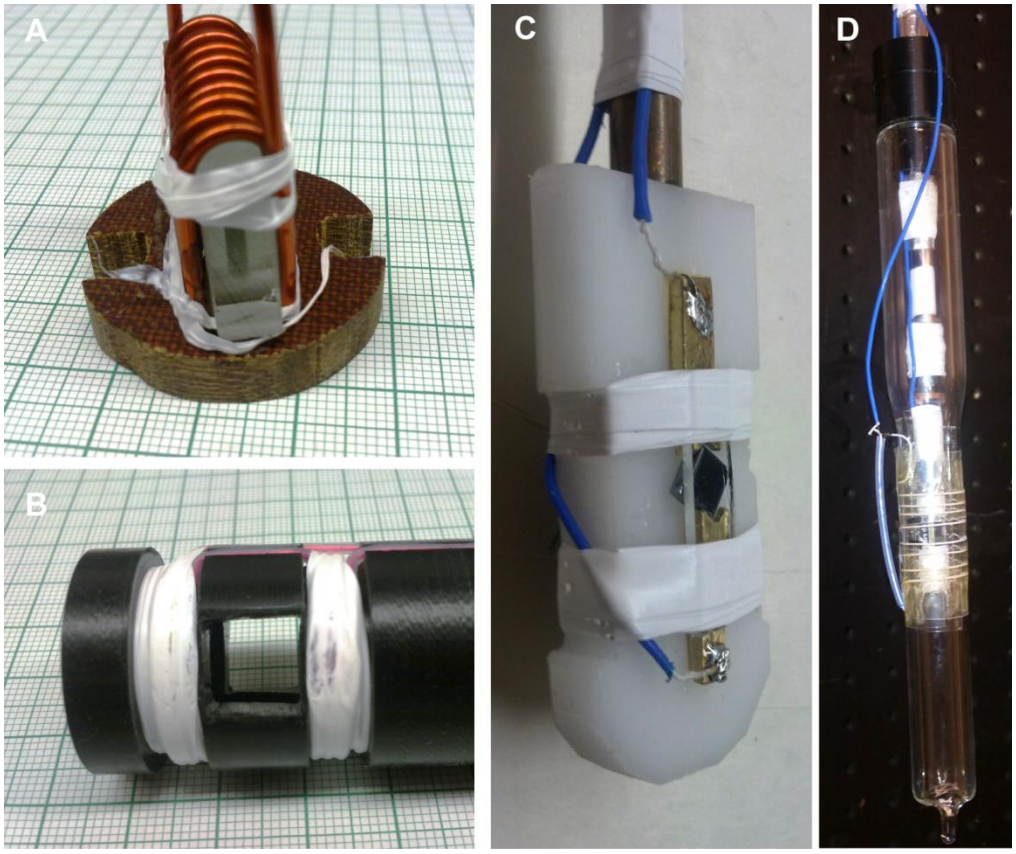

Figure 3.9: ***Different sample holders for PLE, PC and NMR experiments, (A) solenoid coil for preliminary n-type D^0 experiment, (B) Helmholtz coil configuration for better B_1 field homogeneity across the sample, (C) typical photoconductivity measurement setup, (D) sample holder for the temperature ramping form 4.2K to room temperature experiment.***

According to Figure 3.9 A, the RF magnetic field B_1 is orthogonal to B_0, and produced by a 10 turn Cu coil with an approximate cross section of 20x40 mm^2, and length of 40 mm. The coil was matched to 50 Ω by a tuning circuit external to the He dewar at 58.75 MHz, half way between the ~55.847 MHz $RF_{\uparrow}$ and ~61.677 MHz $RF_{\downarrow}$ frequencies. The RF excitations were provided by signal generator/synthesizer (Agilent E4420B). Part way through these studies the frequency accuracy and stability was improved, to better than one part in 10^{10}, by providing a 10 MHz reference from a GPS-

conditioned Rb clock. For all preliminary studies of n-type ^{28}Si samples, the output of the synthesizer was used without amplification, and for pulsed NMR it was switched on and off using high isolation electronic switches driven by pulses of adjustable widths and delays generated with a Spincore Pulseblaster pulse generator.

In the next stage of improvement to our D^+ NMR setup in order to generate and apply more accurate RF pulses (at frequencies $RF_\uparrow \cong 55.847$ MHz, $RF_\downarrow \cong 61.677$ MHz and $RF^+ \cong 1.4567$ MHz) with flexible arbitrary phases, the Agilent signal generator was replaced with a Spincore Pulseblaster DDS NMR synthesizer locked to an external Rb clock for stability, and amplified to the 10 W level. A multifrequency tuner external to the dewar was used to match the 6 turn RF coil (Figure 3.9 D) to the 50 Ω output of the amplifier at both 1.43 MHz and ~59 MHz (half way between $RF_\uparrow$ and $RF_\downarrow$). Since the B_0 field at the sample could not be set precisely, the three resonance frequencies were determined before every experiment by collecting Ramsey fringe scans, and the three π pulse lengths were determined by collecting Rabi oscillation scans. Typical π pulse lengths were 150 to 160 μs for $RF_\uparrow$ and $RF_\downarrow$, and 90 μs for RF^+. The homogeneity of the RF field generated by a coil which must be orthogonal to the static magnetic field is crucial and any inhomogeneity can lead to imperfect control of the nuclear system.

3.4.2. Cryostat and Magnet

Two main liquid He dewars were used in these studies: A liquid He immersion cryostat (with quartz windows) between the pole faces of the iron-core electromagnet with 15.2 cm diameter pole faces separated by 9.5 cm for the fixed cryogenic temperature (≤4.2 K) experiment and a high homogeneity split-pair superconducting magnet system (capable of operating up to 7 Tesla) with a Vari-Temp style sample chamber which allows liquid He to be either brought in from or pushed back to a storage reservoir, for the results involving ramping the sample temperature between 4.2 K and room temperature (for ionized donors).

The sample sits loosely in a cavity immersed in liquid He coolant. Sufficient gaps were included in the sample holder to ensure He contact of the samples at all times. The temperatures given here are those of the He bath as inferred from the vapor pressure above the bath (which was not closely regulated). Most spectra were recorded

at temperatures below the λ-point in superfluid He which has an advantage of improved signal-to-noise level as compared to helium at 4.2K. In the superfluid state, helium boil-off bubbles disappear and do not interfere with the optical path. In addition, thermally activated excitations in the sample were reduced to a minimum. The reduced He vapour pressures as low as ~1mmHg (Torr) which corresponds to a temperature of T=1.3 K were achieved with a mechanical vacuum pump (the vapor pressure of 1 atm, corresponds to a temperature of 4.2 K).

In the first dewar, the sample is centered between the pole faces of the iron-core electromagnet which supplies the static magnetic field B ~ 845 G (the field at which $RF_{\downarrow}$ is at a minimum and $RF_{\uparrow}$ is at a maximum, greatly relaxing the homogeneity and stability constraints on B). For stabilization purposes, B_0 is monitored at the center of one pole face with a Hall probe Gaussmeter (Group3 DTM-151). While the stated value of ~845 G is corrected for the difference of B between the pole face and sample location, the exact field at the sample is not known. The stability and reproducibility of B were better than 0.1 G. The exact resonance frequencies at B_0 [137] and the Si band gap energy [160], and thus the D^0X transition energies, have a small dependence on T and He vapor pressure, which had to be taken into account when changing the sample temperature. There are many important practical issues which lead to imperfections. For example, spatial inhomogeneities in the static magnetic field cause nuclei in different parts of the sample to precess at different frequencies.

Shim usage in magnetic resonance spectrometry

A shim is a device used to adjust the homogeneity of a magnetic field. Originally, shims have their name from the purely mechanical shims that are used to adjust position and parallelism of the pole faces of an electromagnet. In NMR and MRI, shimming is used prior to the operation of the magnet to eliminate inhomogeneities in its field. There are two types of shimming: active and passive. Active shimming is done using coils with adjustable current. Passive shimming involves pieces of steel with good magnetic qualities. The steel pieces are placed near the permanent or superconducting magnet. They get magnetized and produce their own magnetic field. In both cases, the additional magnetic fields (produced by coils or steel) add to the overall magnetic field of the magnet in such a way that the total field becomes more homogeneous.

Figure 3.10 shows how using the ring shims (passive shimming) on the electromagnet poles improves the homogeneity of the magnetic field around the sample. The homogeneity of magnetic field is improved roughly 10 times by shimming.

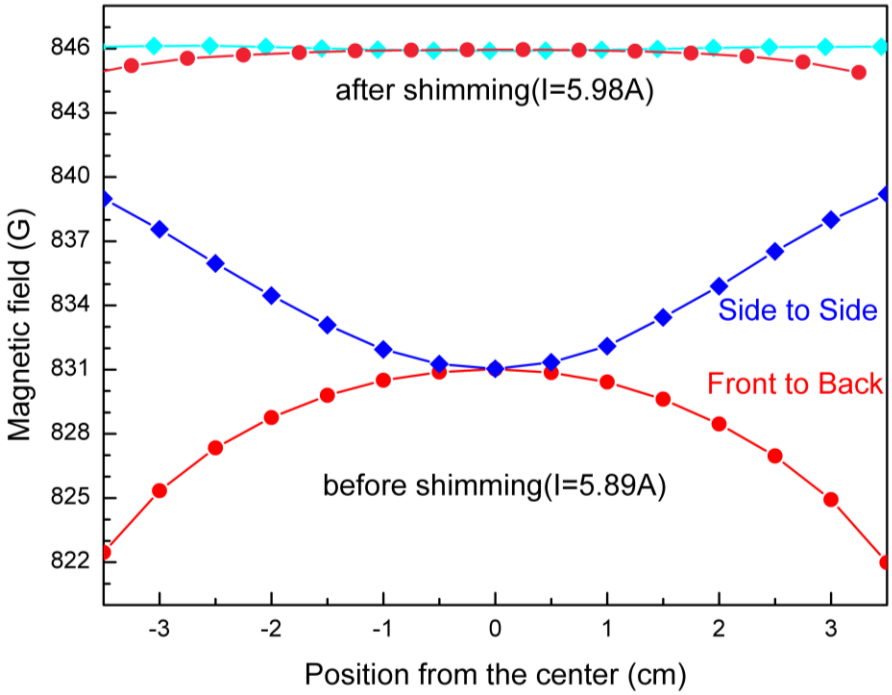

Figure 3.10: Magnetic field mapping of the electromagnet.

All experiments were done at the same $B_0 \cong 845.3$ G used in our previous study of $^{31}P^0$ [54, 137]. This is an advantageous field for studying the nuclear spin of $^{31}P^0$, since at this field $\partial RF_{\uparrow}/\partial B_0 = \partial RF_{\downarrow}/\partial B_0 = 0$, making them clock transitions and greatly relaxing the requirements for B_0 field homogeneity and stability [137]. There is no such advantage for $^{31}P^+$, since $RF^+ = \gamma_n B_0$, where γ_n is the gyromagnetic ratio for $^{31}P^+$, 17.23 MHz/T [85]. For experiments at or below 4.2 K the previous electromagnet system was used, with the addition of a more precise NMR gaussmeter to stabilize B_0 instead of the previous Hall Effect gaussmeter. For experiments above 4.2 K, a Vari-Temp style dewar was needed so that liquid He could be moved back and forth between a storage reservoir and the sample chamber, and this was provided by a high homogeneity split pair superconducting solenoid dewar, operated at $B_0 \cong 845.3$ G in persistent current mode.

3.4.3. Excitation sources

Optical excitation is provided by three lasers through computer-controlled shutters. Above-gap excitation, which is required to generate the free e^- (and holes) needed (for p-type samples) to photoneutralize the donors during initialization and readout, is provided by a 1047nm diode-pumped Nd-YLF (Neodymium doped Yttrium Lithium Fluoride) laser, with a nominal intensity of 200 mW. The two resonant optical excitation sources are tuneable, single-frequency distributed-feedback Yb-doped fibre lasers centered on ^{31}P D^0X transition (~1078nm), both manufactured by Koheras, followed by Yb-doped fibre amplifiers capable of providing up to 1 W of output power. For the preliminary transient measurements of D^0 these lasers are tuned to line 4 (readout laser) and line 6 (polarizing laser) of the D^0X absorption transitions with typical powers at the sample of 10 mW cm^{-2} and 250 mW cm^{-2} respectively. We have improved the system for the task of D^+ readout by adding a third optical beam tuned to line 5, which is derived from the line 6 laser by downshifting a portion of the beam by 56 MHz (~$RF_\uparrow$) using an acousto-optic modulator (AOM). The two Yb-doped fiber lasers are locked and scanned with respect to a stable reference cavity (made of two mirrors and quartz tube inside a copper pipe), which is itself locked to a frequency stabilized HeNe laser. The cavity's temperature control feedback loop guarantees that the cavity's length will not change over time, giving a long term laser frequency stability and repeatability of a few MHz [93]. The four laser beams are turned on and off using fast electromechanical shutters, and a fifth global shutter was added to minimize and block any above-gap (background) light from reaching the sample during the NMR manipulations and the temperature ramps.

For the 4.2 K preparation and readout used in the temperature ramp experiments, the excitation intensities at the sample were approximately 90 mW cm^{-2} for the line 6 laser, 7 mW cm^{-2} for the line 4 and line 5 lasers, and 0.02 mW cm^{-2} for the above-gap 1047nm laser. At temperatures below 4.2 K the optimum 1047nm laser power and the readout transient times were found to be temperature dependent, which we ascribe to the capture of e^- onto D^0 and free holes onto A^0 to form D^- and A^+ centers, since these centers have the ~2 meV binding energies which would explain strong thermal dissociation at 4.2 K and binding at lower temperatures [161].

At a given preparation/readout temperature the 1047nm above-gap laser power was adjusted to the minimum needed for efficient photoneutralization, since excess 1047nm laser power has two deleterious effects. First, by generating more e^- and free holes it 'shorts out' the sample, making the impedance changes from the resonantly created e^- more difficult to observe. Second, by creating free excitons which can bind onto D^0 to form D^0X, the above-gap excitation enables a process, which under our low field conditions where the e^- and donor electrons are essentially unpolarized, drives the nuclear polarization towards equilibrium, counteracting our resonant hyperpolarization [68]. Capture of the unpolarized e^- generated by the above-gap excitation onto D^+ could also reduce the achievable hyperpolarization.

3.4.4. Data collection

The basic PLE apparatus used in this study is almost the same as the one used in previous studies [65, 93] with a small modification in the data collection part. The liquid nitrogen cooled Germanium detector was replaced with a photomultiplier tube due to higher sensitivity useful for the samples with low ^{31}P concentrations (very weak PL) and faster response for studying fast transient processes. The apparatus is still configured to collect any resonantly generated D^0X luminescence from the sample, as used previously [62, 65, 137] to monitor D^0X creation, but the low ^{31}P concentration in the p-type ^{28}Si–Avo sample made this luminescence almost impossible to detect (even with the photomultiplier tube module). Instead, the change in conductivity resulting from Auger electrons was detected using a noncontact, capacitive photoconductivity approach, which is a form of electrically detected magnetic resonance (EDMR) we have referred to as Auger electron detected magnetic resonance (AEDMR). This noncontact approach eliminated any possibility of straining the sample, and also eliminated the need for ohmic contacts. As shown in Figure 3.8, the sample was an element in a parallel plate capacitor, with no direct electrical contact between the sample and electrodes. A 114 kHz sine wave, with amplitude of 20 V PP, was applied to one electrode, and the other electrode was connected to a high gain, high impedance amplifier. A phase-shifted and attenuated signal was coupled to the same input through a 1 pF capacitor, forming an impedance bridge which allowed the signal coupled through the sample to be cancelled under any particular illumination conditions. The out-of-balance bridge signal

was then fed to a lock-in amplifier, with the output being the photoconductive signal of interest. For the collection of spectra the readout laser was additionally chopped at 40 Hz, and a second lock-in amplifier was used to process the photoconductive signal and detect only the component resulting from the chopped readout laser.

3.4.5. Temperature ramping

Experiments requiring the initialization of the sample at 4.2 K followed by raising it to room temperature (e.g. for T_{2n} measurements), and returning it to 4.2 K for readout required the construction of a new sample holder, which is shown in Figure 3.9 D and Figure 3.11. A small evacuated glass mini-dewar, which is a snug fit in the Vari-Temp sample chamber tube, surrounds the sample holder so that it could be warmed to room temperature without needing to warm the entire sample tube/window block/RF coil. This reduces the effect of temperature on the coil to keep the π pulse length as stable as possible. At the top of the sample holder is a standard Cu heater block, with a bifilar-wound 25 Ohm heater and a rectangular Cu stub pointing downwards. The sample holder itself is made of four strips of sapphire and a strip of high purity natural Si, all 5mm wide, which are glued to each other and to the Cu stub on the heater block using thermally conductive epoxy (Stycast 2850 FT). The sample fits loosely into the sample compartment formed by the four sapphire strips, sitting on the bottom strip under its own weight, and with ~150 microns between each 5x4.7 mm^2 face and the sapphire. Two temperature sensors are attached to the sapphire using the same thermally conductive epoxy, one at the heater end (sensor1) and one below the sample compartment (sensor2). The two open sides of the sample compartment are covered by brass shim strips which both enclose the sample compartment and also act as electrodes for the capacitive photoconductivity measurement. The sample and sample holder are immersed in liquid He at 4.2 K for initialization and readout.

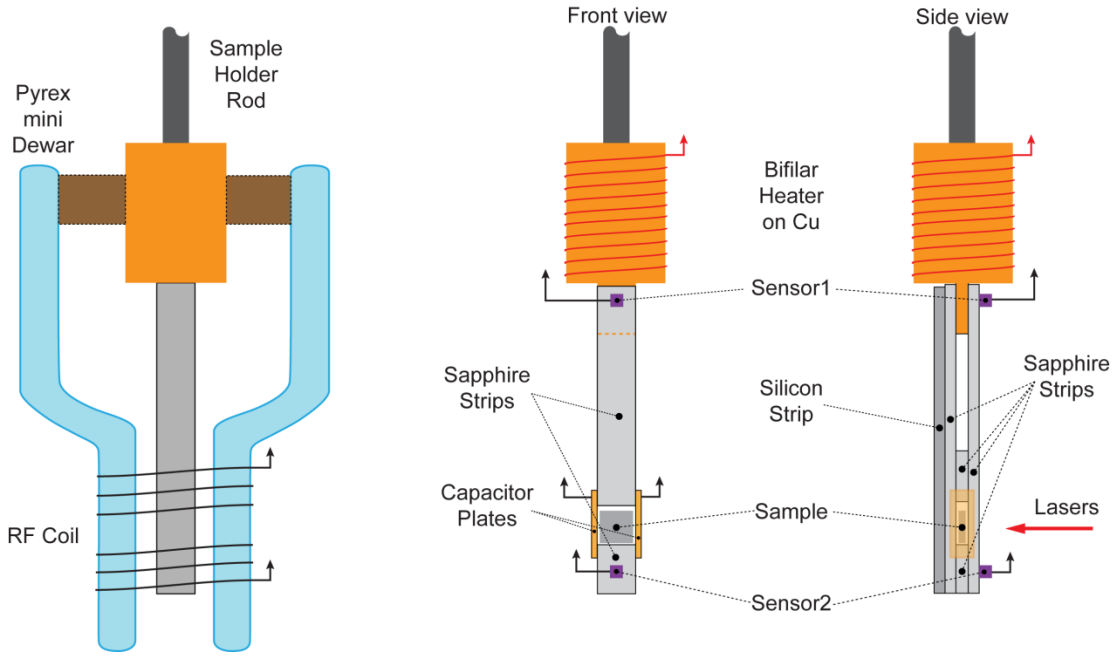

Figure 3.11: ***The sample holder and mini-dewar assembly used for the temperature ramp experiments.***

The first step of a temperature ramp is to pressurize the sample chamber and open the He needle valve, thus pushing the liquid He from the sample chamber back into the He reservoir. After this the needle valve is closed and the sample remains under 1 atmosphere of He gas. A proportional temperature controller set to 298 K and controlled by sensor2 is then turned on, initially providing 25 W to the heater. The sample holder temperature rises very quickly at first due to the low heat capacities at low temperature, but as this slows down an increasing temperature gradient occurs along the length of the sample holder, and sensor1 throttles the heater power so that the temperature at the heater end of the sample holder never rises above 350 K (see Figure 3.12). The temperature difference between sensor1 and sensor2 rises to ~150 K during the temperature up ramp, but decreases as the bottom of the sample holder approaches room temperature and proportional control based on the sensor2 temperature takes over. Two minutes after sensor2 first reaches room temperature the gradient along the sample holder has dropped to ~20 K, and at this point the manipulation of the nuclear spins begins. Mounting a temperature sensor directly to the sample is not feasible since our optical ensemble measurement is highly sensitive to strain, but we calculate the

thermal time constant of the sample coupled to the sample holder through He gas to be seconds at room temperature. Given the positioning of sensor2, the ~6 minute ramp up time, and the 2 minute wait time at room temperature before any measurement, we are confident that the sample is at or slightly above 298 K during measurement. During cooldown, the heater power is turned off and the needle valve is opened a controlled amount, so that an overpressure on the He reservoir transfers liquid He to the sample chamber slowly enough that the boiloff He gas is used to efficiently cool the sample holder. After ~4 minutes the sample, sample holder and both sensors are immersed under liquid He, at which point the readout process can begin.

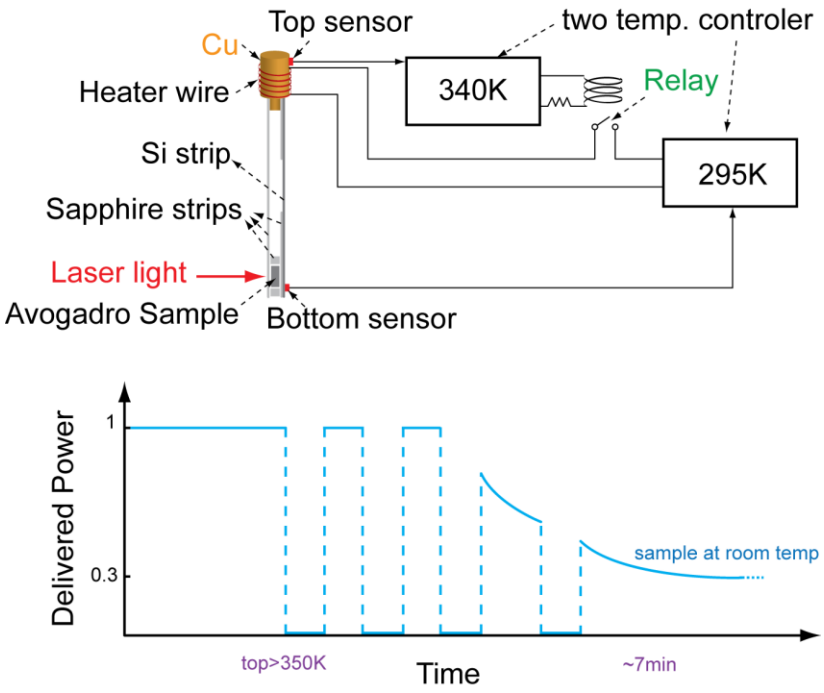

Figure 3.12: ***Schematic of feedback control loop and the time it takes to ramp the temperature of the sample between 4.2K and room temperature.***

The reason behind using Sapphire in the Vari Temp sample holder

The main reason is transparency and extremely high thermal conductivity of sapphire. Sapphire is not only highly transparent to wavelengths of light between 150 nm (UV) and 5500 nm (IR) but it is also significantly (5 times) stronger/tougher than glass (tempered glass/any other optical material) and ranks a 9 on the Mohs Scale. Also

sapphire has a quite low conductivity for electricity, but a much-higher conductivity for heat. Thus, sapphire provides good electrical insulation, while at the same time doing a good job at helping to conduct away the significant heat that is generated in the heater to the sample very quickly.

4. Results and Discussion

In this chapter, a typical PL spectrum and derived impurity concentrations of n-type ^{28}Si samples is presented. By examining PLE spectra of D^0X in the n-type and p-type ^{28}Si-Avo samples, the dependence of the D^0X transition linewidth on temperature, B field and 1047-nm above band gap light is investigated. Then, the electron and hole g-factor variations with respect to the orientation of B field along sample are extracted. Next, using the mechanism illustrated in the previous Chapter, hyperpolarization results are given. The results of huge electron and nuclear polarization are followed by an investigation of the dynamics of neutral P donor populations in the four hyperfine ground states to find T_1. Finally, optical NMR results of D^0 and D^+ related to the quantum coherence time measurement using decoupling techniques are shown in detail along with a discussion of the decoherence channels.

4.1. Photoluminescence spectroscopy of ^{28}Si

One of application of PL spectroscopy is determining the acceptor and donor impurity concentration in silicon. We have used this technique to map out the concentrations of the main impurities in our P-doped n-type ^{28}Si samples cut from “Si28-10Pr10.6.1PeFz3” crystal. The PL spectrum using 532-nm green laser excitation on each side of each slice is collected and the intensity ratio of phosphorous or boron bound exciton (BE) to free exciton (FE) is extracted. Figure 4.1 shows a typical PL spectrum.

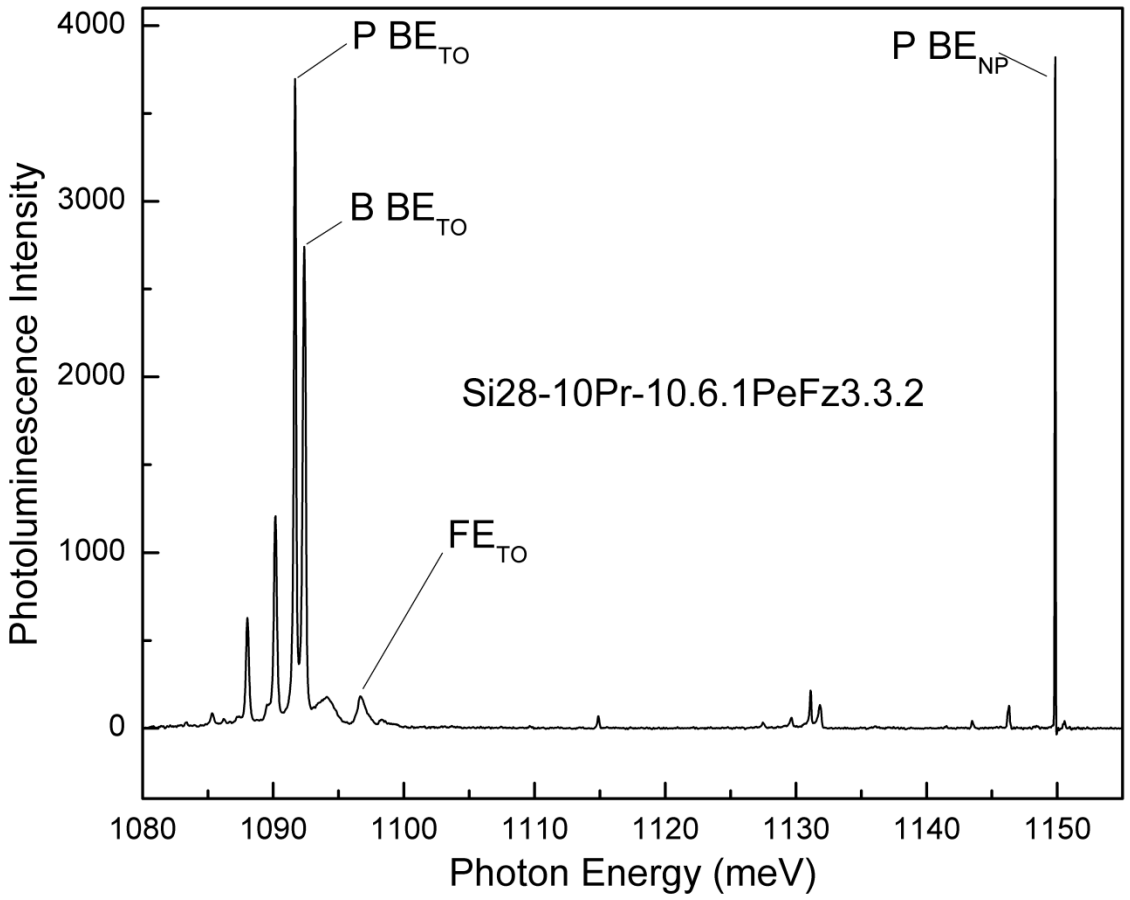

Figure 4.1: ***PL spectrum showing the no-phonon (NP) and transverse-optical (TO) phonon –assisted P and B bound exciton (BE) transitions for the ^{28}Si:P 3.3.2 n-type sample at T=4.2K.***

The main difference between ^{28}Si:P (P-doped n-type) and ^{28}Si-Avo (p-type) samples' PL spectra is the much larger FE_{TO} peak in the ^{28}Si-Avo due to the lower impurity concentration of the Avogadro material. Using calibration factors ($1.3x10^{13}$ cm^{-3} for P and $4.2x10^{12}$ cm^{-3} for B), the BE to FE ratios can be translated to the [P] and [B] concentrations [100] of the 13 slices that make up part of "Si28-10Pr10.6.1PeFz3" crystal which is shown in Figure 4.2.

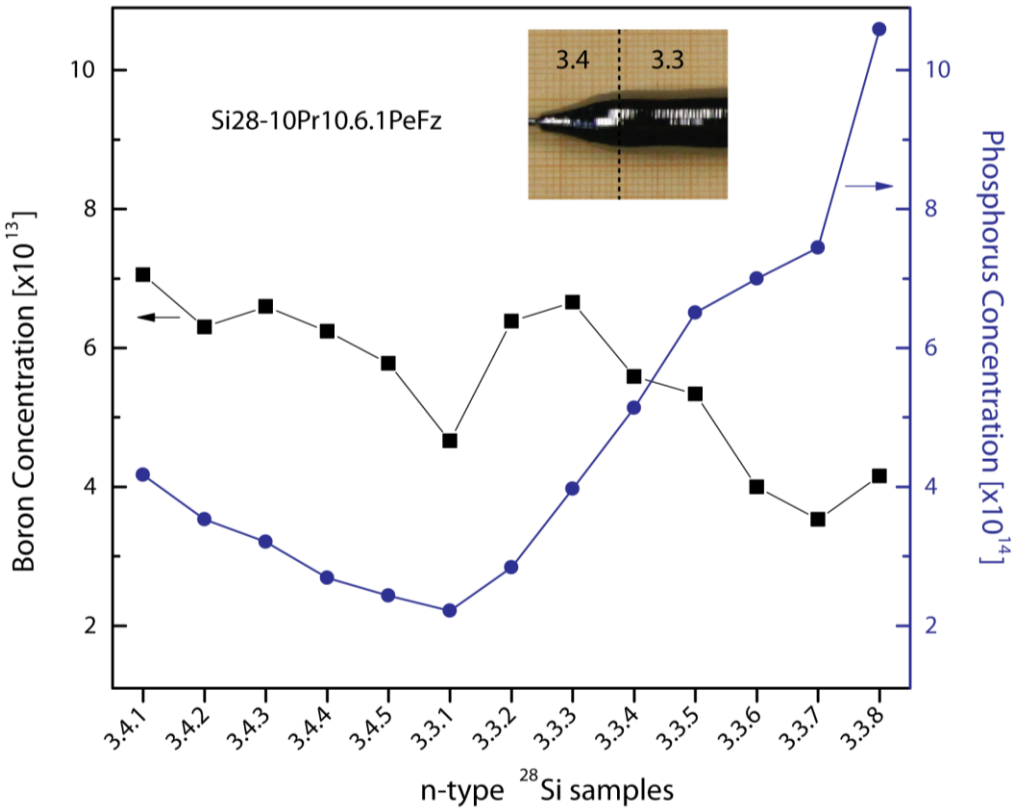

Figure 4.2: ***The P and B concentration map of an n-type ^{28}Si sample. All slices were cut from the Si28-10Pr10.6.1PeFz3 crystal. The concentration of Boron should almost be the same/uniform along the crystal (~6x10^{13}). The phosphine gas is turned on right after crystal got to the final diameter (the dashed line shown in the crystal picture) for P-doping.***

In fact, this is not a very accurate way to determine the concentrations of impurities in silicon, and the Boron concentration results below 5x10^{13} cm^{-3} are not reliable due to high concentration of P. Usually the electrical conductivity (or resistivity) of the silicon crystal ingot is measured to figure out the impurity concentration in the Si manufacturing industry. However, the conductivity (≡ (Ω.cm)$^{-1}$) measurement only gives N_A-N_D and cannot give information about the specific types of impurities (n-type or p-type) or the degree of compensation.

4.2. PLE spectroscopy of ^{28}Si

As mentioned in the previous chapter, the PLE spectroscopy method (pumping NP lines and monitoring TO phonon replica), using a tunable single-frequency laser source with sub-MHz linewidth, provides a huge increase in instrumental resolution compared to the Fourier transform PL method and can resolve all the D^0X transitions of ^{28}Si under a moderate magnetic field. The Zeeman split hyperfine P D^0X lines under low magnetic field can be resolved and Figure 4.3 compares PLE spectra of our n-type ^{28}Si with the ^{28}Si-Avo sample. It is clear that hyperfine doublet lines are better resolved in the Avogadro sample due to lower impurity content which results in reduction of inhomogeneous broadening.

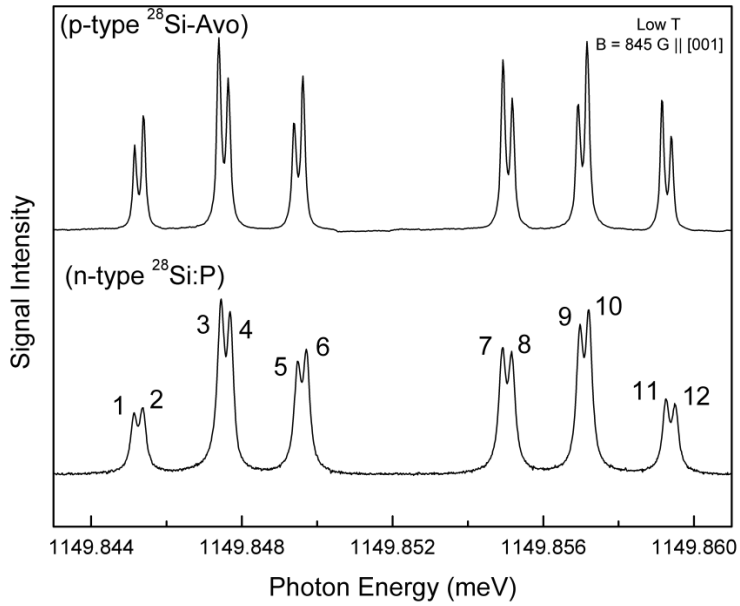

Figure 4.3: ***Typical unpumped (unpolarized) PLE spectra showing the 12 NP transition of P D^0X hyperfine components under the magic B_m field. Lines are labeled from 1 to 12 in order of increasing energy as in Fig. 3.2.***

As mentioned earlier, shallow P donor BEs in Si have very low radiative quantum efficiencies due to the dominance of nonradiative Auger recombination [103], which is a drawback for using optical readout of the P donor spin state [73]. However, the near-unity efficiency of the Auger process of these BE transitions suggests a mechanism

(detecting the free electrons created in the Auger process) for reading out the nuclear spin of individual ^{31}P impurities [62].

4.3. Unpolarized PC spectra of $^{31}P^{0}X$ under different conditions

In Figure 4.4, PC spectra of the small ^{28}Si-Avo sample at constant temperature (T=4.2K) under different static magnetic fields show no change in the $D^{0}X$ transition's linewidth. It indicates that the hole lifetime (homogeneous broadening of holes) does not depend on magnetic field in this range of field as shown in the Figure 4.4. B field values are calculated from the electron splittings extracted from the PC spectra as measuring the static magnetic field at the sample position is difficult because a Gaussmeter is only able to measure outside of the cryostat. Instead these spectra provide more accurate value of the field at the sample so these PC spectra can be used for magnetic field calibration.

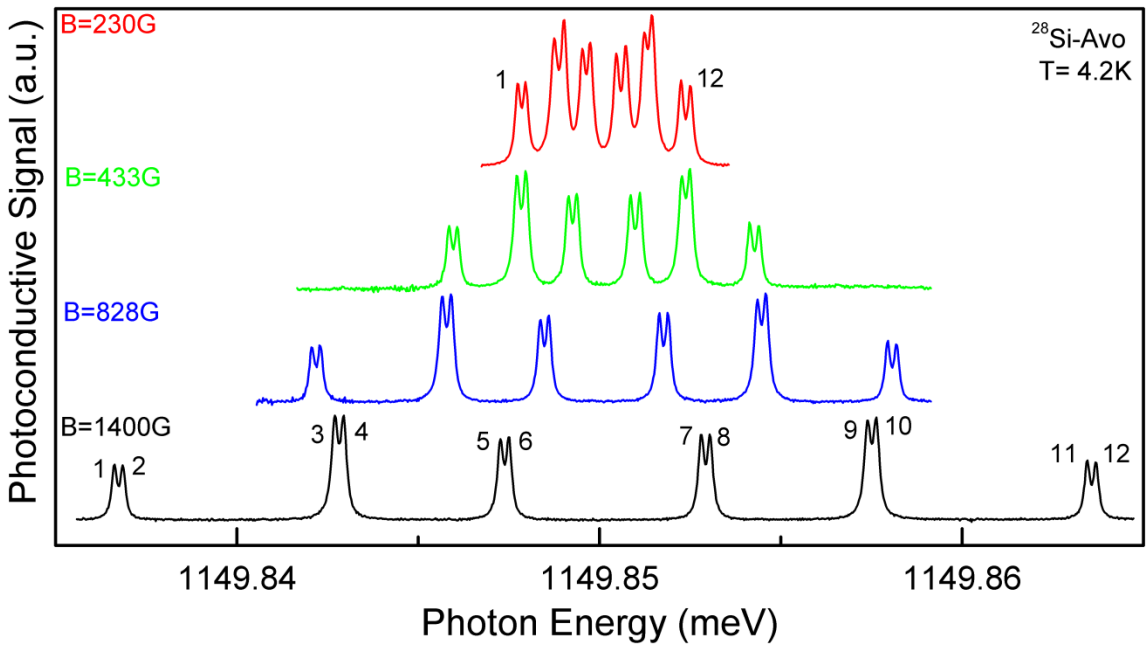

Figure 4.4: ***PC spectra of ^{31}P $D^{0}X$ transitions under different magnetic fields. Lines are labeled from 1 to 12 in order of increasing energy as in Fig. 3.2.***

On the other hand, the resolution of hyperfine splitting changes drastically with the temperature as shown in the Figure 4.5 based on their full width at half maximum (FWHM). The FWHM decreases from 190 neV (46 MHz) to 120 neV (29 MHz).

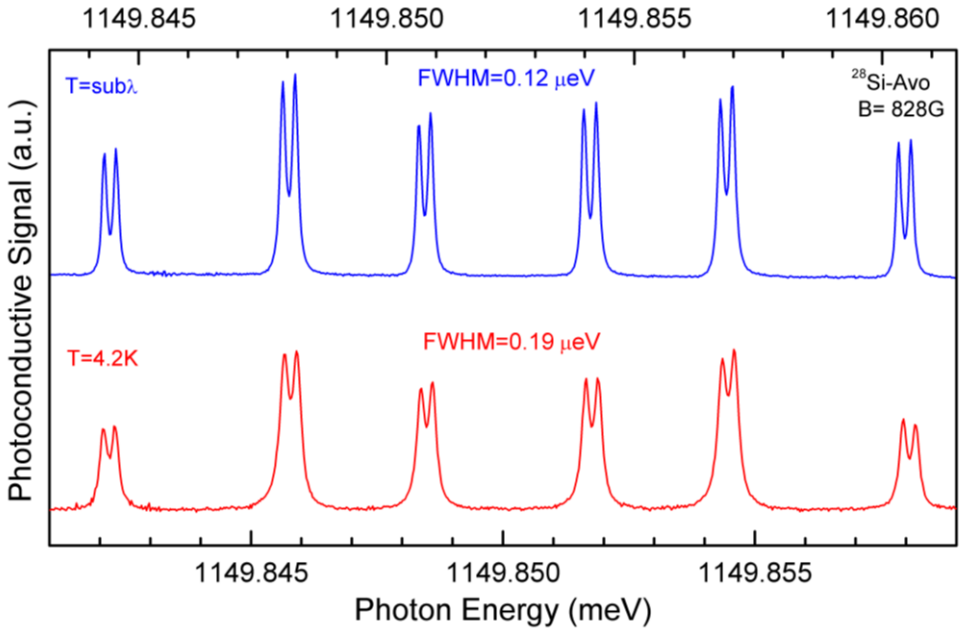

Figure 4.5: PC spectra of ^{31}P D^0X transitions at different temperatures. The T=subλ refers to the LHe temperatures below superfluid transition.

The temperature dependency of these D^0X optical transitions is studied in more detail in Figure 4.6. We pumped on the liquid He (LHe) in the cryostat to reduce the He vapor pressure and reduce the temperature of the sample. The He vapor pressure of 1 atm and ~1mmHg (Torr) corresponds to temperatures of 4.2 K and 1.3 K respectively. As the LHe is cooled down through 2.17 K (superfluid transition point known as λ point), the boiling suddenly becomes violent, and then stops completely below the λ point. In the superfluid state, the thermal conductivity of liquid He is extremely large. This causes heat in the body of the liquid to be transferred to its surface so quickly that vaporization takes place only at the free surface of the liquid. Thus, there are no gas bubbles in the body of the sub-λ liquid He in contact with the sample which could act as a tiny strain and broaden the optical transition lines.

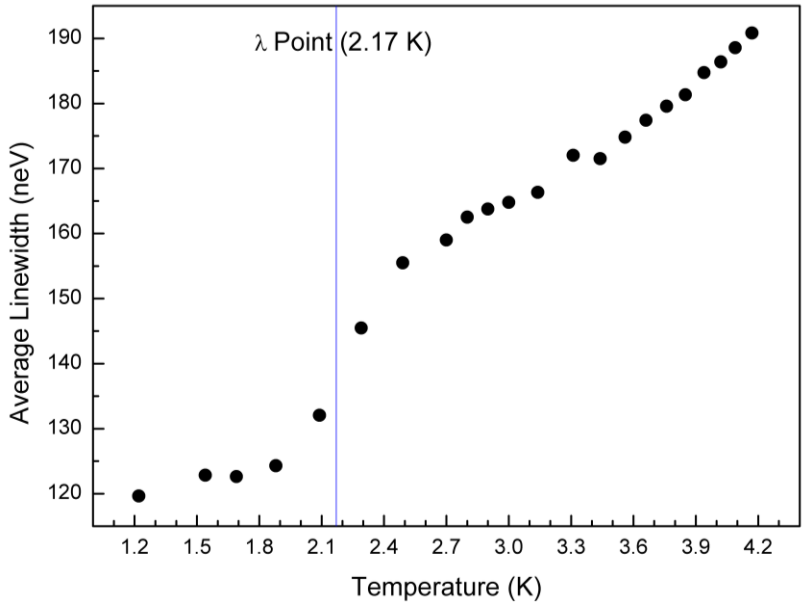

Figure 4.6: Average linewidth of ^{31}P D^0X transitions in ^{28}Si-Avo at different temperatures

PLE spectroscopy has previously been applied to experimentally determine the band gap dependence on temperature in the limit of T→0. By measuring the temperature shift of the remarkably sharp BE transitions in ^{28}Si across the liquid-He temperature region, the low-T behavior of the silicon band gap was determined to vary as T^4 [160].

Apart from going to superfluid temperatures, the power ratio of the resonant laser and nonresonant above band gap 1047nm laser excitation is important in achieving the best resolution for unpolarized PC spectra with the narrowest linewidth for the D^0X transitions. As illustrated in Figure 4.7, a drawback of not using enough above-gap 1047nm excitation is that the transition lines are slightly broadened. The above band gap excitation both produce photoneutralization, reducing Stark broadening and also act to equalize the donor hyperfine population, reducing the saturation effcect produced by resonant laser.

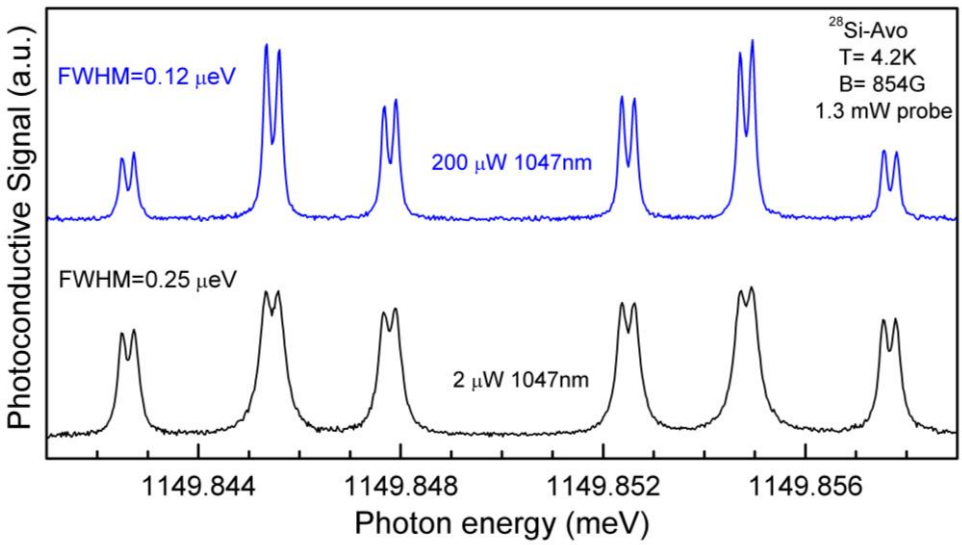

Figure 4.7: Effect of above band gap light on the D^0X spectrum of ^{28}Si-Avo

4.4. Angular dependence of electron and hole g-factor

A g-factor, also called a dimensionless magnetic moment, is a proportionality constant that relates the observed magnetic moment μ of a particle to the appropriate angular momentum quantum number and the appropriate fundamental quantum unit of magnetism, usually the Bohr magneton or nuclear magneton. In order to investigate its angular dependence, PC spectra (examples shown in Figure 4.8) of the sample are collected at different orientations with respect to the static magnetic field. The energy splitting of the electron, light hole (j_h=1/2) and heavy hole (j_h=3/2) can then be extracted and plotted in Figure 4.9. The light and heavy hole splittings, which are responsible for the spacing between the doublets in the D^0X spectrum depend on the orientation of the sample crystal with respect to the static magnetic field B_0. Three different orientations are shown in Figure 4.8.

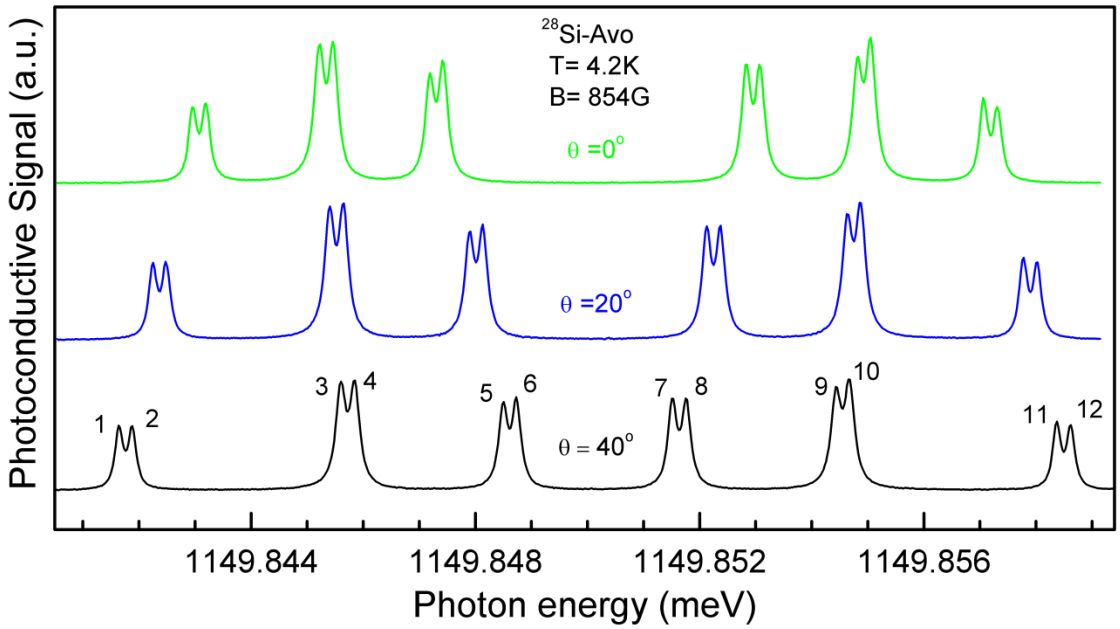

Figure 4.8: ***PC spectra of ^{31}P D^0X transitions at different orientation of crystal with reference to [001] along the B field. Lines are labeled from 1 to 12 in order of increasing energy as in Fig. 3.2.***

Once the *B* field is accurately determined, one can calculate the electron and hole g-factors from the D^0X PC spectra. For example, to measure the light hole splitting, the simplest way is to subtract the energies of transition lines 1(2) and 5(6) from the electron spin up branch, or lines 7(8) and 11(12) from the electron spin down branch, which have the same ground states but are excited into the different ±1/2 light hole states. Similarly, the electron splitting can be measured by subtracting energy of lines 1(2) from 7(8) or 5(6) from 11(12) which have different ground state but same hole states. However, determination of the 3/2 heavy hole splitting cannot be calculated directly from the D^0X transition lines due to forbidden transitions.

From Figure 4.10, it can be seen that the heavy (light) hole g-factor is maximum (minimum) when *B*||[100] and minimum (maximum) when *B*||[110]. It is obvious from Figure 4.9 and 4.10 that the electron splitting is independent of the sample orientation and only depends on the amplitude of the B_0, as expected. Unlike the hole g-factors, the electron g-factor (~1.998) is insensitive to the sample orientation inside the static magnetic field.

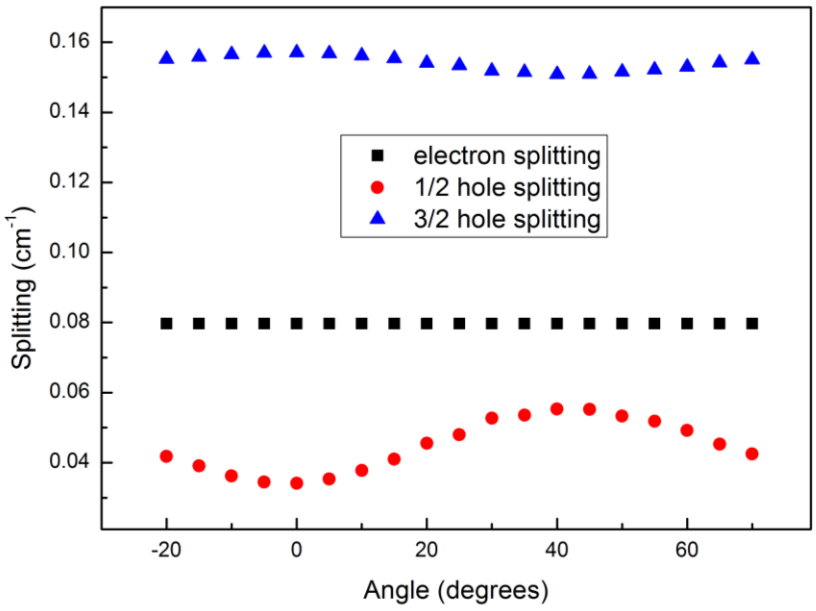

Figure 4.9: Angular dependence of electron and hole splitting

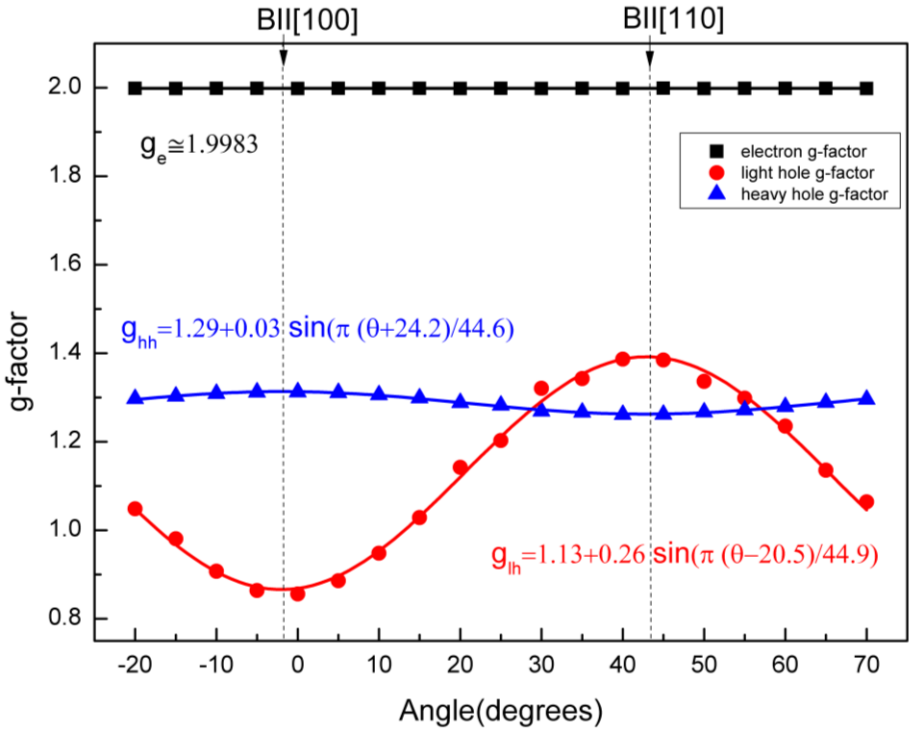

Figure 4.10: Angular dependence of the g-factors (g_{lh} and g_{hh})

As shown in the Table 4.1, the hole g-factors, as determined from the spectra, for *B*||[100] are in good agreement with earlier studies of the phosphorus BE at much higher fields [162]. The g-factors of the holes can be represented in the following form if *B*||[001] then $g_{1/2h} = g_1+(1/4)g_2$ and $g_{3/2h} = g_1+(9/4)g_2$ [163]. Table 4.1 compares our g_1 and g_2 values extracted from our fits to the g_{lh} and g_{hh} according to [163] with earlier results.

Table 4.1: Comparison between our hole g-factor results and earlier studies for B||[100].

Source	g_{lh} or $g_{1/2h}$	g_{hh} or $g_{3/2h}$	g_1	g_2
Our results	0.87	1.32	0.81	0.23
Kaminski et. al.	0.86	1.33	0.80	0.24

4.5. Hyperpolarization of the D^0X spectra

Previous PLE studies of the P BE transition under an applied magnetic field led to optical pumping experiments which produced hyperpolarization of electron and nuclear spins of ^{31}P donors [65]. In our NMR experiments, hyperpolarizing the system is a prerequisite to manipulating the populations in the four hyperfine states. The simplest way of optically polarizing the system is fixing the pump laser on a specific line (usually pumping line 6 or 8 gives us stronger hyperpolarization [65]). Figure 4.11 shows two spectra of ^{28}Si-avo sample under the same magnetic field; on the bottom is an unpumped spectrum, showing the 12 D^0X hyperfine components and the expected absence of significant equilibrium electron or nuclear polarization. Above is the hyperpolarized spectrum relevant to this study, showing a large electron and nuclear polarization obtained by pumping line 8 (shown by arrow), which hyperpolarizes the system into the pure state $|\uparrow\Uparrow\rangle$.

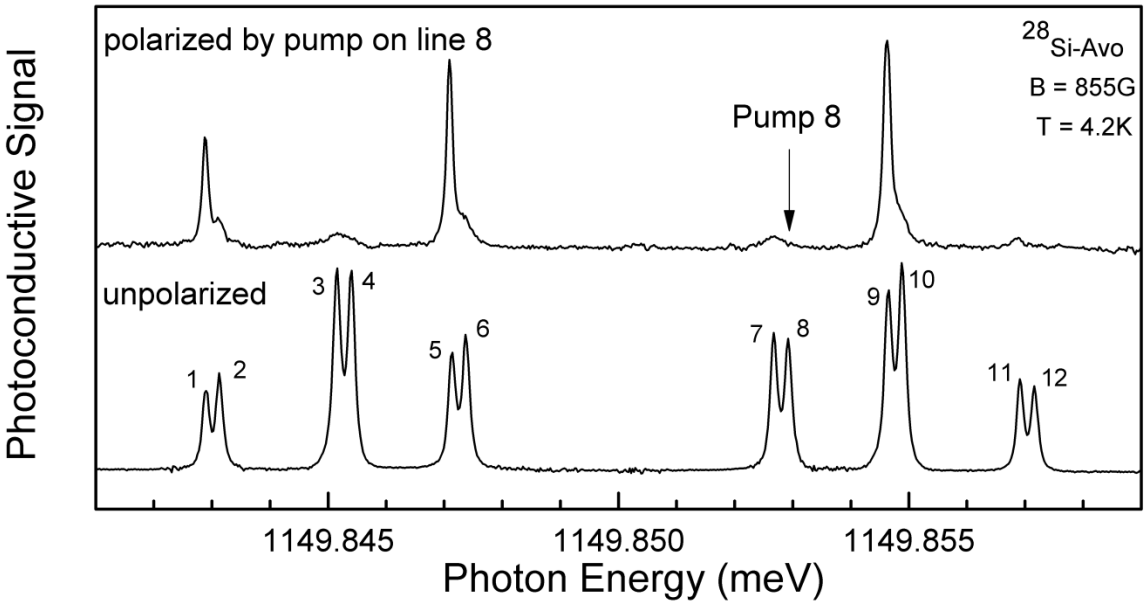

Figure 4.11: Effect of optical pumping: comparing unpolarized PC spectrum with the hyperpolarized spectrum by pumping on line 8.

Figure 4.12 shows the difference between unpolarized (bottom) and polarized (top) spectra of n-type and p-type (^{28}Si-Avo) samples that have been collected by two different methods. Because the ^{31}P concentration in the p-type ^{28}Si-Avo sample is 3 orders of magnitude lower than in the n-type samples, a PLE spectrum of p-type ^{28}Si-Avo sample would be too noisy and not feasible. The two hyperpolarized spectra relevant to this study, showing the large electron and nuclear polarization obtained by pumping line 6, which hyperpolarizes the system into the pure state $|\downarrow\Downarrow\rangle$ are shown in Figure 4.12 (top).

The reason there is less nuclear hyperpolarization in the p-type sample (Figure 4.12B) compared to the n-type sample (Figure 4.12A) is the necessity (will be explained later) of using a small amount of 1047nm above band gap light when taking the spectrum of the p-type sample in order to photoneutralize the positively ionized donors. It should be noted that although n-type spectra are collected at much lower temperature (at 1.3K) than p-type ^{28}Si-Avo sample spectra (at 4.2K), the resolution is worse (due to higher impurity concentrations in the n-type sample).

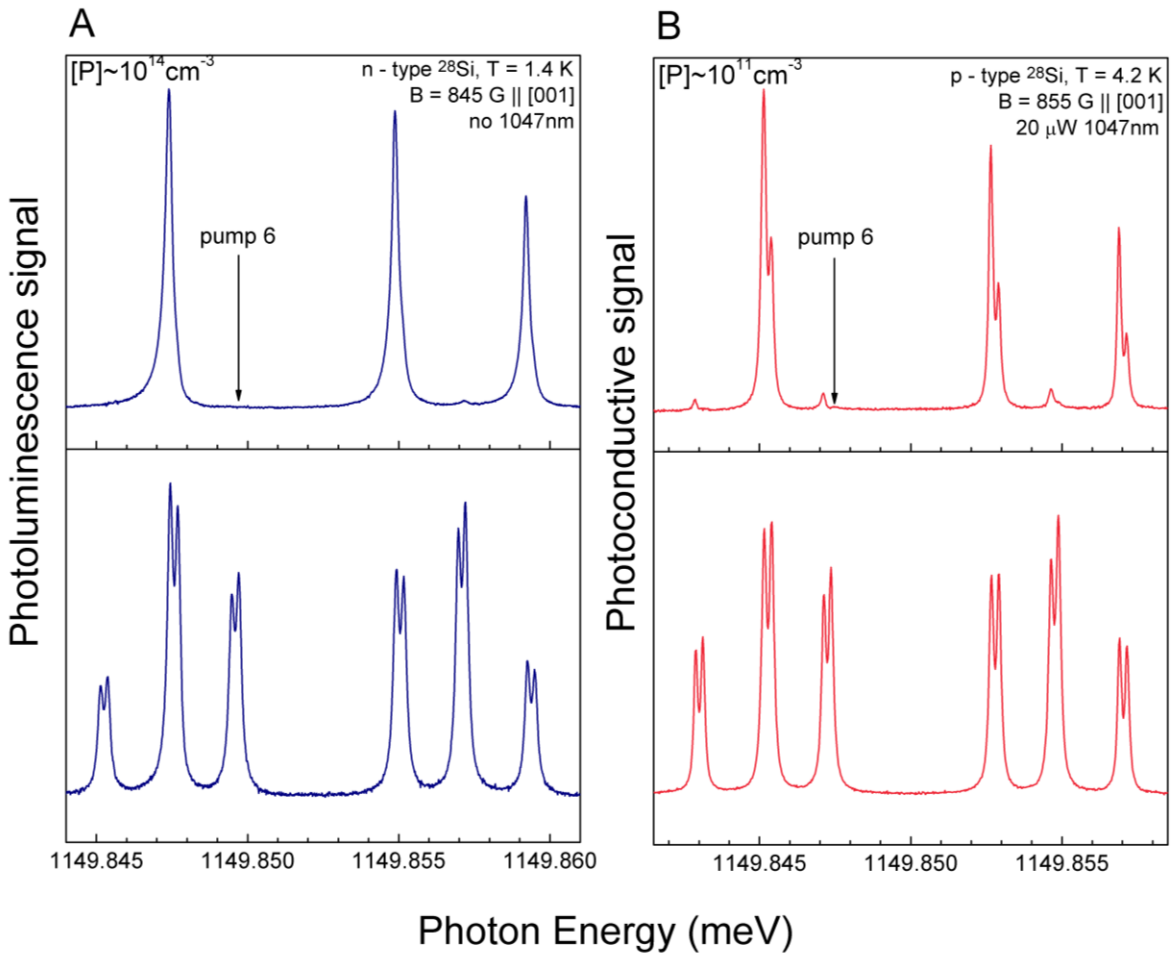

Figure 4.12: ***Comparison of hyperpolarization of D^0X spectra in the n-type (A) and p-type (B) samples.***

The reduced nuclear (and electronic) hyperpolarization in the presence of above-gap excitation results from both the increased speed of relaxation processes induced by the free carriers, and the Auger ionization of D^0 in each of the four hyperfine states by the formation of D^0X via the random capture of free excitons onto D^0. In order to compensate for smaller hyperpolarization in the p-type ^{28}Si-Avo sample, as explained in the previous chapter, we have modified our hyperpolarization schemes by adding NMR frequencies during the polarization step.

Figure 4.13 (top right) demonstrates how choosing the wrong NMR frequency (applying $RF_{\downarrow}$~61MHz while pumping $|\uparrow\Downarrow\rangle$ state) can hurt the degree/amount of nuclear hyperpolarization.

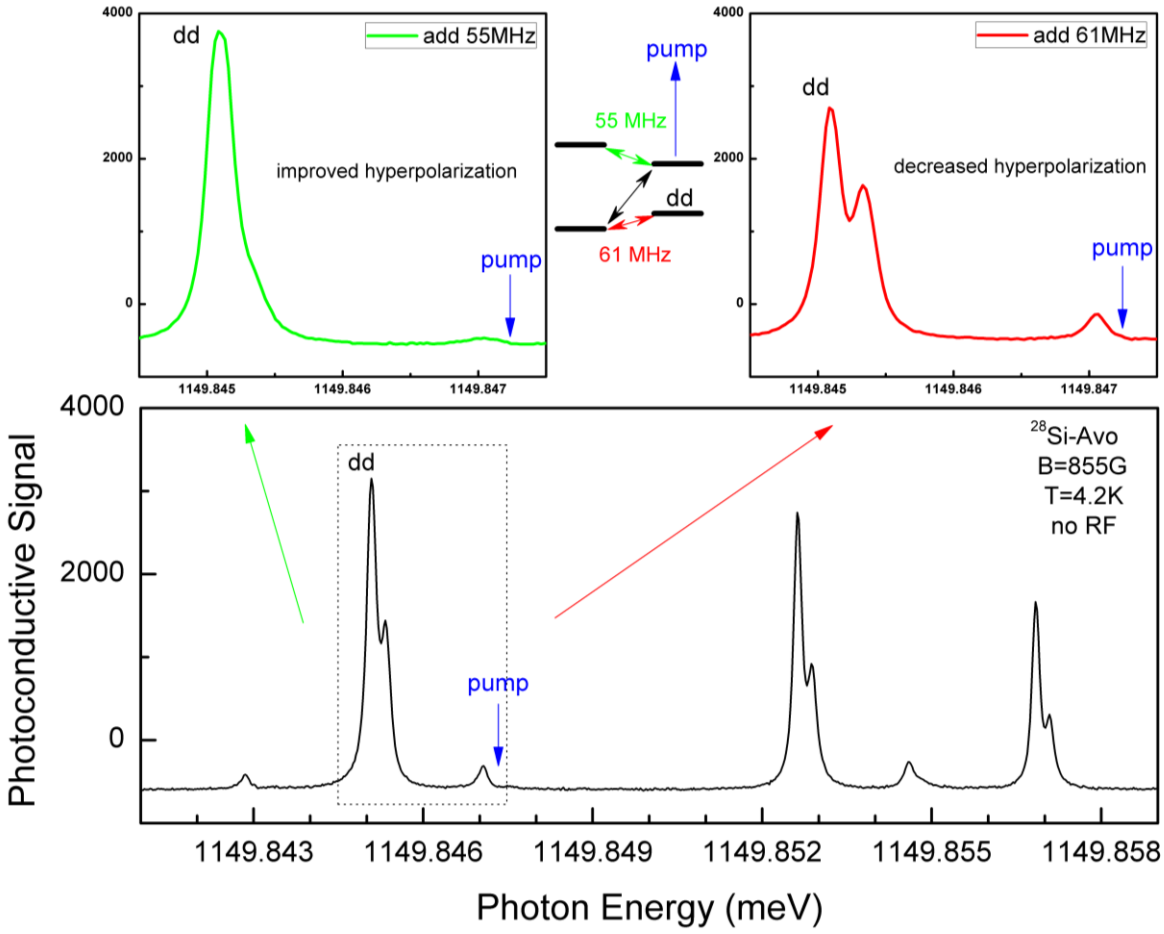

Figure 4.13: ***Shows effect of adding specific NMR frequency, $RF_{\uparrow}$ (top left) or $RF_{\downarrow}$ (top right) on the hyperpolarization of D^0X spectrum by pumping on line 6 (bottom) scheme.***

The results of the improved hyperpolarization schemes explained in Chapter 3 were measured by a noncontact photoconductive detection method as the readout laser was scanned across the 12 D^0X transitions (low-power above-gap excitation is present in all cases) (Figure 4.14 at 4.2K and Figure 4.15 at 2.1K).

From the relative intensities in Figure 4.14, we find that 95% of D^0 are pumped to $|\downarrow\Downarrow\rangle$ ($|3\rangle$), resulting in a net electron polarization $P_e = 0.99$ and nuclear polarization $P_n = 0.90$ (Table 4.2). At this magnetic field and temperature, the electron equilibrium spin polarization is 0.013, so the hyperpolarization enhancement is 76; the nuclear equilibrium spin polarization is 4×10^{-4}, so the hyperpolarization enhancement is 2,250.

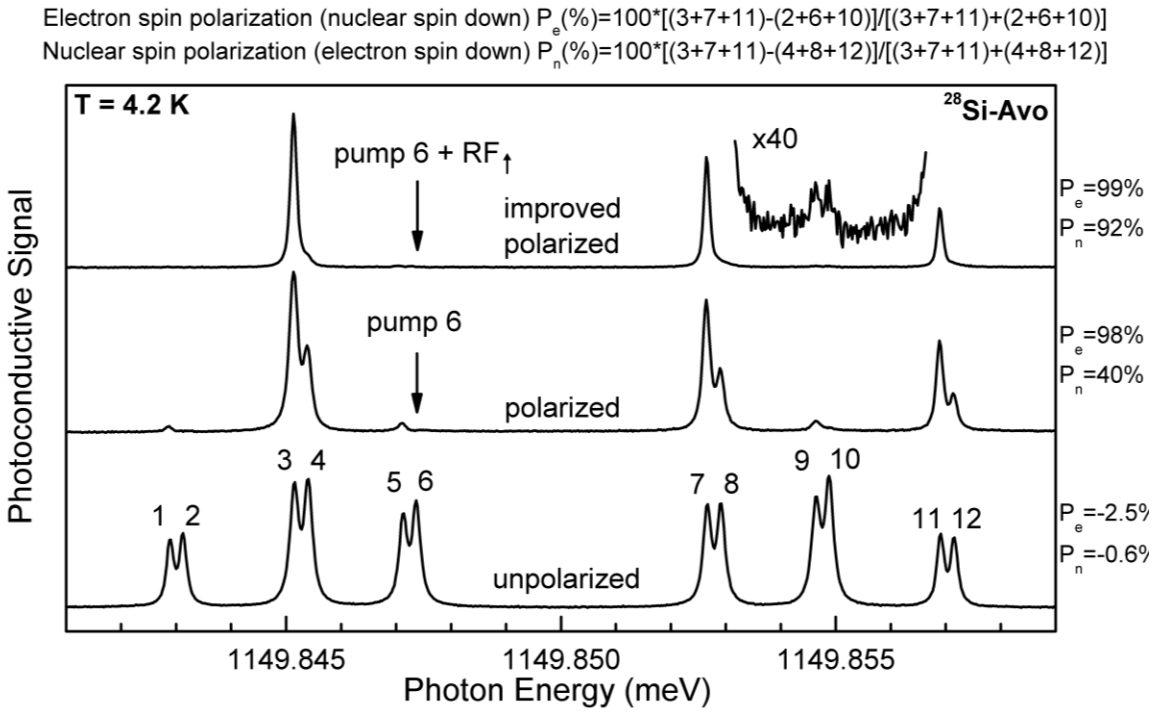

Figure 4.14: ***Photoconductivity D^0X spectra of ^{28}Si-Avo sample at T = 4.2 K and B = 845 G, for the largely unpolarized equilibrium case (bottom) and using the original hyperpolarization scheme (middle) and improved hyperpolarization scheme (top). The relative intensities of lines 3, 4, 9, and 10 give directly the relative populations of D^0 states $|\downarrow\Downarrow\rangle$ ($|3\rangle$), $|\downarrow\Uparrow\rangle$ ($|4\rangle$), $|1\rangle$, and $|2\rangle$, respectively.***

In addition, the new polarization scheme also shortened the polarization time from ~1 s to 100 ms. Therefore, this method is much faster and more effective than any previous [60, 64, 137] nuclear polarization scheme for impurities in semiconductors.

Electron spin polarization (nuclear spin down) $P_e(\%)=100*[(3+7+11)-(2+6+10)]/[(3+7+11)+(2+6+10)]$
Nuclear spin polarization (electron spin down) $P_n(\%)=100*[(3+7+11)-(4+8+12)]/[(3+7+11)+(4+8+12)]$

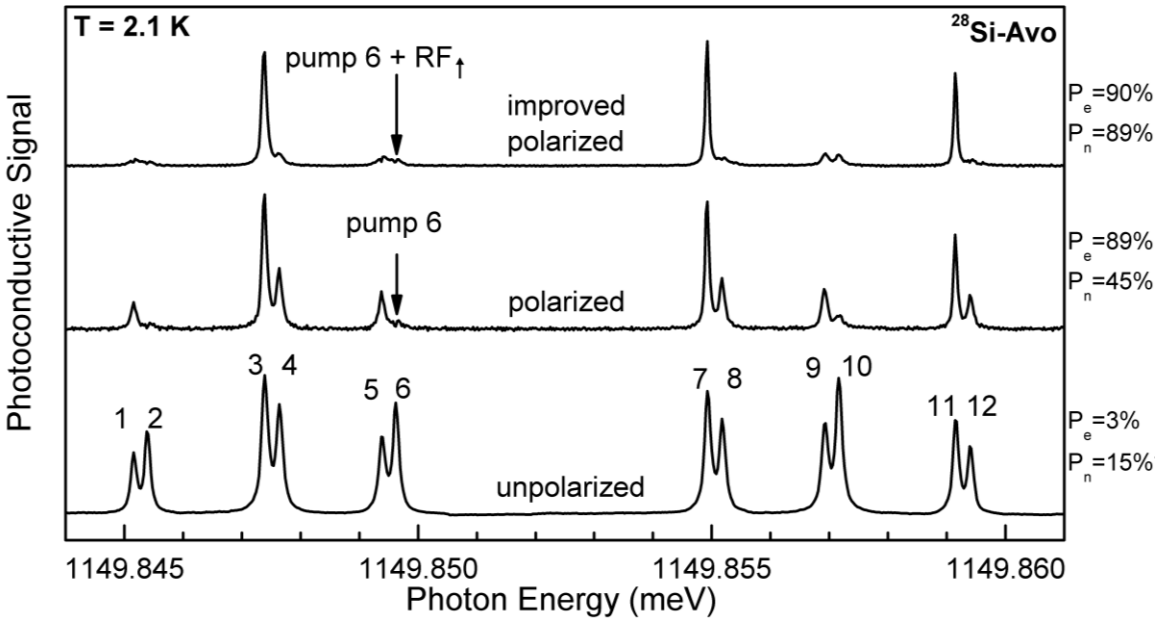

Figure 4.15: Photoconductivity D^0X spectra of ^{28}Si-Avo sample at T = 2.1 K and B = 845 G, for the unpolarized equilibrium case (bottom), using the original (middle) and improved hyperpolarization scheme (top).

The reason why experimental polarization values for the unpolarized case do not match with the calculated equilibrium polarization is because of the presence of above band gap excitation and also any nonresonant excitation from the probe laser during the scan can induce small nonresonant polarizations.

Table 4.2: Showing the experimental values of the electron and nuclear polarizations compared to their calculated equilibrium polarizations at 4.2K and 2.1K.

Polarization (%)	Calculated equilibrium	Experimental Unpolarized	Experimental Polarized (pump 6 only)	Experimental Improved Polarization
Electron (4.2K)	1.3	-2.5	98	99
Nuclear (4.2K)	0.04	0.6	-40	-90
Electron (2.1K)	2.6	3	89	90
Nuclear (2.1K)	0.07	-15	-45	-89

From the results shown in Table 4.2, it seems that our hyperpolarization method works slightly better at 4.2K (later in time) than at 2.1K (earlier in time); It is possible that our setup and parameters were not optimized when the low temperature data was taken or the higher amount of 1047nm excitation we used/needed in the 2.1K spectra compared to the 4.2K spectra, is affecting our hyperpolarization efficiency.

Note that the nonresonant optical hyperpolarization method reported [64, 68] for donor nuclear spins would not be useful under the present conditions, since it requires a high magnetic field to produce a large equilibrium electron polarization, which is transferred to the nuclear spins via the Overhauser effect.

4.6. Initialization and readout of D^0 and D^+ for optically detected NMR experiments

The following is an attempt to summarize our understanding of what is happening in the Avogadro material during polarization, post-polarization optimization and readout.

Polarization – This refers to the simultaneous presence of the low power X laser on line 4 (pump 4), the high power Y laser on line 6 (pump 6), an optimum level of 1047 nm light (using an ND=3.5 filter at T=1.9 K) and $RF_{\uparrow}$ at ~55 MHz (shown in Figure 4.16 A under D^0 Prep.). Although 100ms seems sufficient, we often use up to 500 ms. The donors get cycled through ionized and neutral states during this period, and at the end virtually all donors, either neutral or ionized, have nuclear spin down ($|\downarrow\Downarrow\rangle$ or $|\Downarrow\rangle$). However, the balance between photoneutralization driven by the 1047-nm light, and photoionization driven by pump 4 and pump 6 lasers results in a near 50-50 split between neutral and ionized donors at the end of the polarization (step {1}). The neutral donors are almost all in $|\downarrow\Downarrow\rangle$ (D^0 prep.). There is no highly efficient way to prepare all the donors as D^0 in $|\downarrow\Downarrow\rangle$.

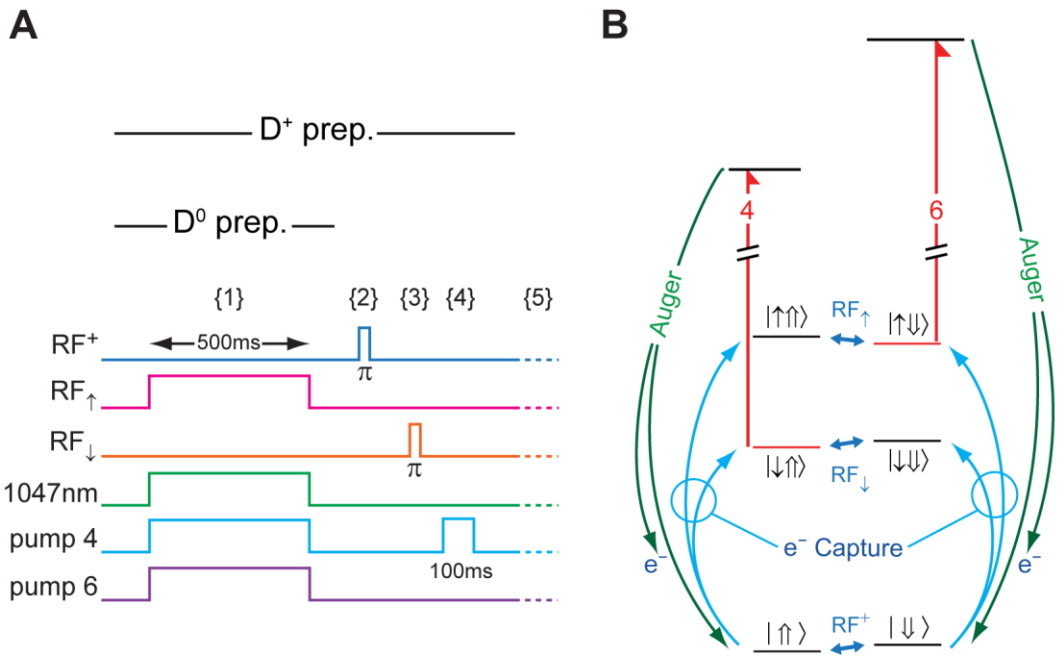

Figure 4.16: ***(A) The laser and RF sequences used to prepare D^0 in the $|\downarrow\Downarrow\rangle$ state (step {1}) and D^+ in the $|\Uparrow\rangle$ state (steps {1} to {4}), (B) The specific optical transitions (lines 4 and 6) and nuclear magnetic resonance transitions ($RF_\uparrow$, $RF_\downarrow$, and RF^+) used here to hyperpolarize the nuclear spins.***

Post-polarization optimization for D^0 – If one is looking for polarized D^0, the polarization procedure can be followed by a brief period of 1047-nm laser exposure to neutralize some of the D^+. Our 'standard' practice has been to use 10 ms of 1047-nm following the polarization stage.

Post-polarization optimization for D^+ – It is actually easier to generate a very pure D^+ $|\Uparrow\rangle$ state than the D^0 $|\downarrow\Downarrow\rangle$ initial state. This is done by applying RF^+ and $RF_\downarrow$ π pulses, which flip the nuclear spins of nearly 100% of the donors, followed by 100ms of pump 4 laser excitation to ionize almost all the D^0 (step {1} to {4}). The result polarizes nearly all the donors into spin up D^+ (D^+ prep.).

Readout – Single-shot readouts of D^+, polarized into either $|\Uparrow\rangle$ or $|\Downarrow\rangle$ and then reneutralized, are shown in Figure 4.17, contrasting our readout method optimized for D^0 (Figure 4.17A) with the improved readout used for D^+ (Figure 4.17B). The fast (~5 ms) buildup transient in Figure 4.17B is the time needed to convert D^0 to D^0X under our

excitation conditions (the D^0X Auger decay time is 272 ns [103]), and the ~ 25 ms decay time is the time taken to recapture e^- onto D^+, giving a $D^0 \rightarrow D^0X \rightarrow D^+ \rightarrow D^0$ cycle time of ~30 ms, in agreement with the transients seen in Figure 4.17A.

We had still been using the old style approach which works well for the NMR experiments, of having a high power polarizing laser (pump) on line 6 and a lower power probe laser on line 4 for readout. This two-laser scheme had the advantage of giving a very strong signal for the nuclear polarization, since the repolarization transient lasted several seconds. However, this scheme was not flexible enough and could not measure everything we need to know, so we switched over to using one laser at a time, pump laser to polarize and probe laser to readout, so we can access the populations in all four hyperfine states in individual, single-shot measurements. There is still enough signal-to-noise for this to work.

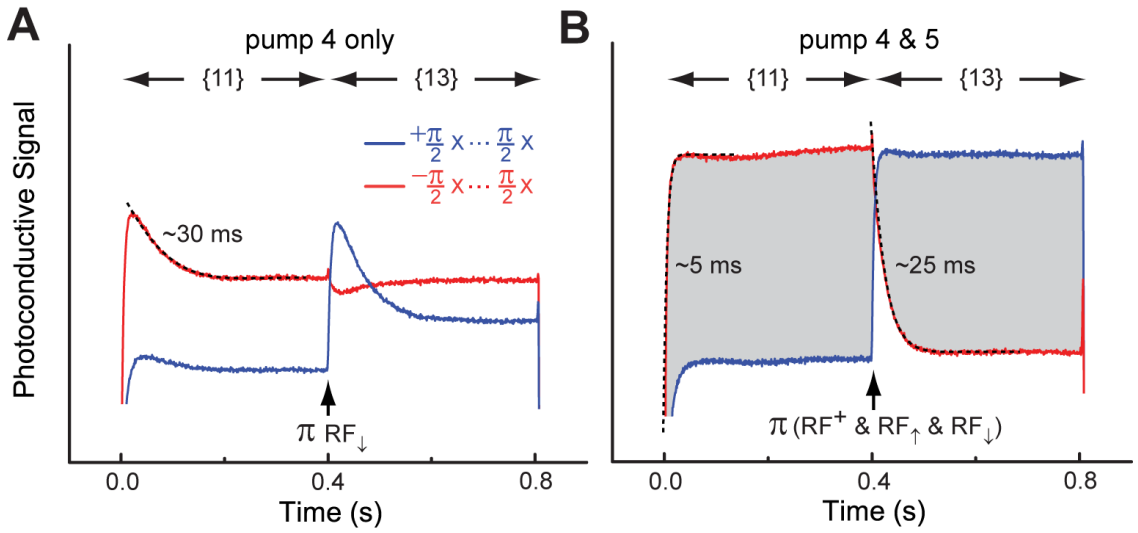

Figure 4.17: ***Comparing readout schemes; (A) Single shot readout of D^+ polarized $|\Uparrow\rangle$ (red) or $|\Downarrow\rangle$ (blue) using our previous method optimized for D^0 readout is compared with (B), the improved scheme for D^+ readout. The detected signal is proportional to the shaded area.***

The Auger decay process is central to both the D^0 hyperpolarization and hyperfine state readout using resonant D^0X photoconductivity, as illustrated in the previous Chapter.

Analysis of the data in Figure 4.17B and 4.18A, shows that the $D^0 \rightarrow D^0X \rightarrow D^+ \rightarrow D^0$ readout cycle can be repeated at least 250 times before the nuclear polarization decays by a factor of 1/e (This 30ms time for the donor measurement cycle was combined with the decay seen in Figure 4.18A to arrive at the estimate of at least 250 D^0X cycles before the nuclear polarization decayed to 1/e.), which is an underestimate given that much of the decay in Figure 4.18A is due to imperfections in the readout π pulses (which are also accumulative). A similar insensitivity of the nuclear spin polarization to repeated donor charge cycles has been reported for the readout of a single ^{31}P nuclear spin [78] and for ensemble measurements using electrically detected magnetic resonance [75]. Figure 4.18B shows the decay of nuclear spin polarization during our continuous readout (40 times) indicating the robustness of our nuclear readout.

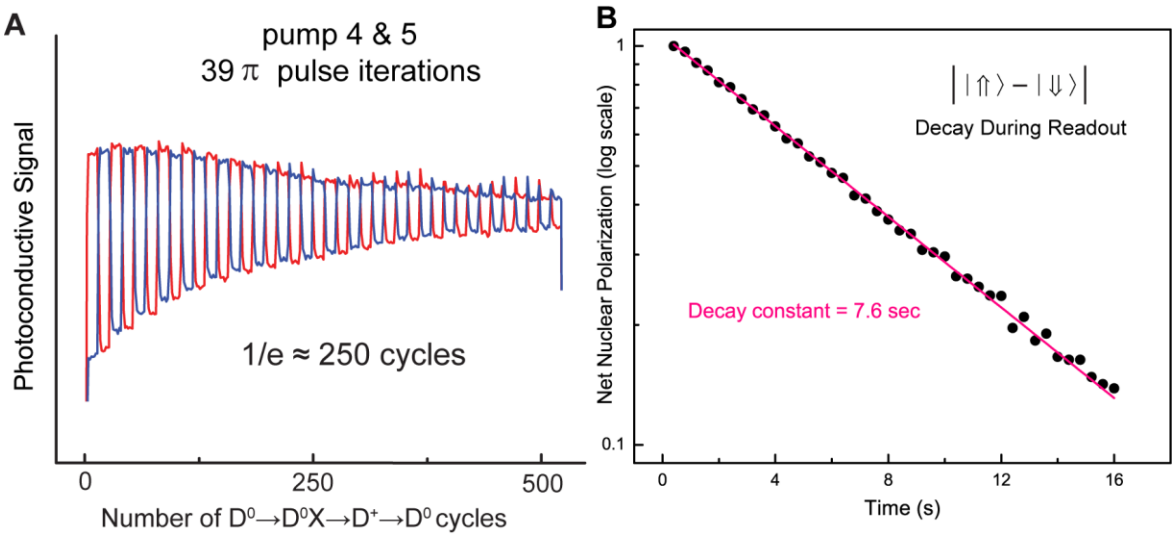

Figure 4.18: The cycle shown in Figure 4.17B extended to 39 π pulse inversions (16 s)

4.7. The T_1 measurements of neutral D^0 and ionized D^+ spins

After hyperpolarizing our system, the simplest experiment is to leave the sample in the dark under the static *B* field and examine the evolution of the population in the four hyperfine levels, resulting in experimental values for T_{1e} and T_{1n}. Our results are in

agreement with a simple model that governs the population of the four hyperfine states assuming there are only two relaxation channels: the electron–electron (e-e) T_E and the flip-flop T_x (cross) relaxation rates.

Labelling the hyperfine states in order of decreasing energy (at B<3T) from state 1 $|\uparrow\Uparrow\rangle$, state 2 $|\uparrow\Downarrow\rangle$, state 3 $|\downarrow\Downarrow\rangle$ to state 4 $|\downarrow\Uparrow\rangle$, we use the following standard procedure: polarize the system into state 3 (10 seconds of pump laser on line 6) or polarize the system into state 4 (10 seconds of pump laser on line 6 + π pulse of ~61MHz RF). We could similarly polarize the system into state 1 or state 2 using pump laser on line10, but polarizing into state 3 is sufficient. We can also completely depolarize the system with 2 seconds of 200mW 1047nm excitation following the initialization. We readout all four populations by repeating the above sequence and using probe laser on line 9 to read out state 1, probe laser on line10 to read out state 2, probe laser on line 3 to read out state 3, and probe laser on line4 to read out state 4.

For the T_1 measurement of neutral D^0 in the n-type ^{28}Si, we have done the above described procedure for dark times of 0, ½ hr, 2 hr and 8 hrs after initializing the system into state 3 (pure state $|\downarrow\Downarrow\rangle$). Next we have repeated the same dark times when initializing the system into state 4.

4.7.1. T_1 results of D^0 in the n-type ^{28}Si sample

The long recovery in the dark scan results from the moderately doped ^{28}Si:P slice 3.3.6 sample at 1.3K after initialization the system into the $|\downarrow\Downarrow\rangle$ pure ($|3\rangle$) state is shown in Figure 4.19. Very long electron and nuclear polarization (P_e and P_N) decays leading to the T_{1e} (8 hours) and T_{1n} (44 hours) results extracted from the data in the Figure 4.19 are shown in the inset of Figure 4.19. We have also verified that initialization to the $|\downarrow\Uparrow\rangle$ mixed ($|4\rangle$) state decays somewhat faster than pure state, which can only be due to the flip-flop channel.

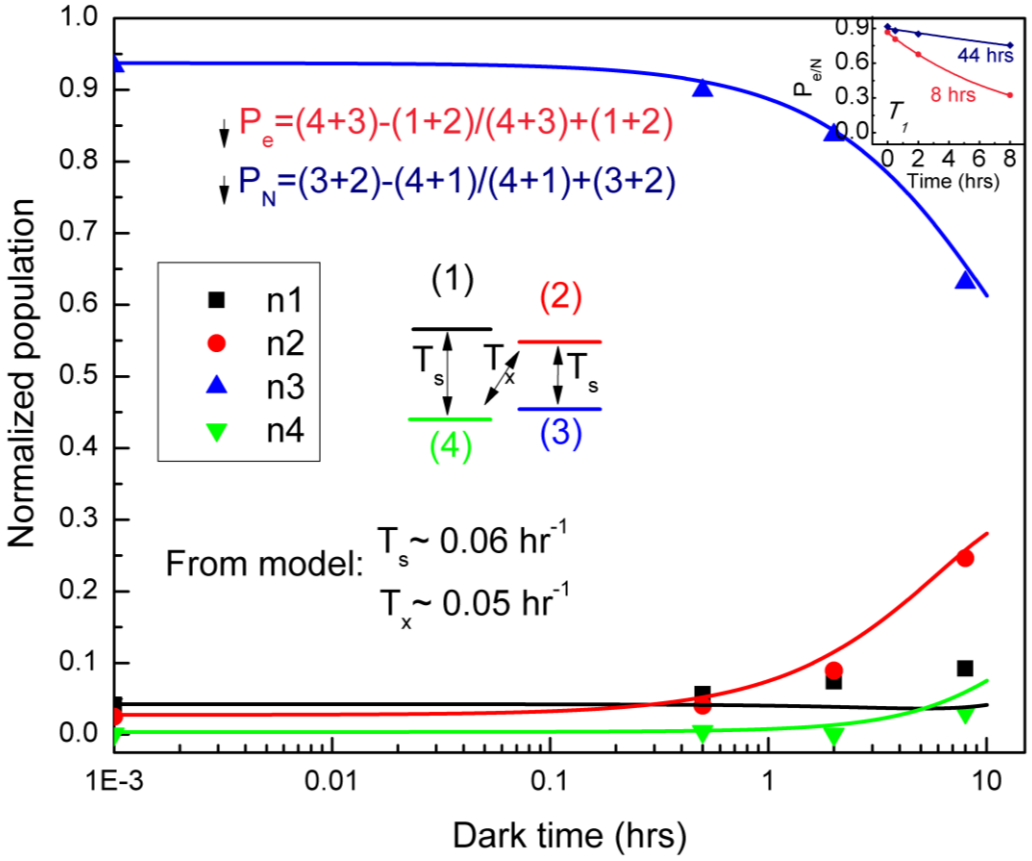

Figure 4.19: ***Evolution of the system polarized into the pure state |↓⇓⟩ (|3⟩) in the dark at T=1.3K for ^{28}Si:P 3.3.6 sample***

4.7.2. T_1 results of D^0 in the p-type ^{28}Si-Avo sample

Figure 4.20 shows the result for the Avogadro sample at 4.2K in which the system is polarized to pure state 3 then followed by the measurement of 4 hyperfine states population after variable dark times. Comparing the T_1 resulted from the data in Figure 4.20 with the T_1 result from the previous section which is hours, clearly indicates the temperature dependency of T_1 relaxation times. In fact, temperature is playing an important role in determining T_1 relaxation times as expected. This short (~22s) T_{1e} at 4.2K, which is in good agreement with an earlier experimental result [84], is the main parameter that puts the $T_{2n} < 2T_{1e}$ limit [60] on the T_2 coherence time of the neutral donor at 4.2K and above. From the data in Figure 4.20, T_{1n} = 450 s, but we know that this is extended to hours at low temperature.

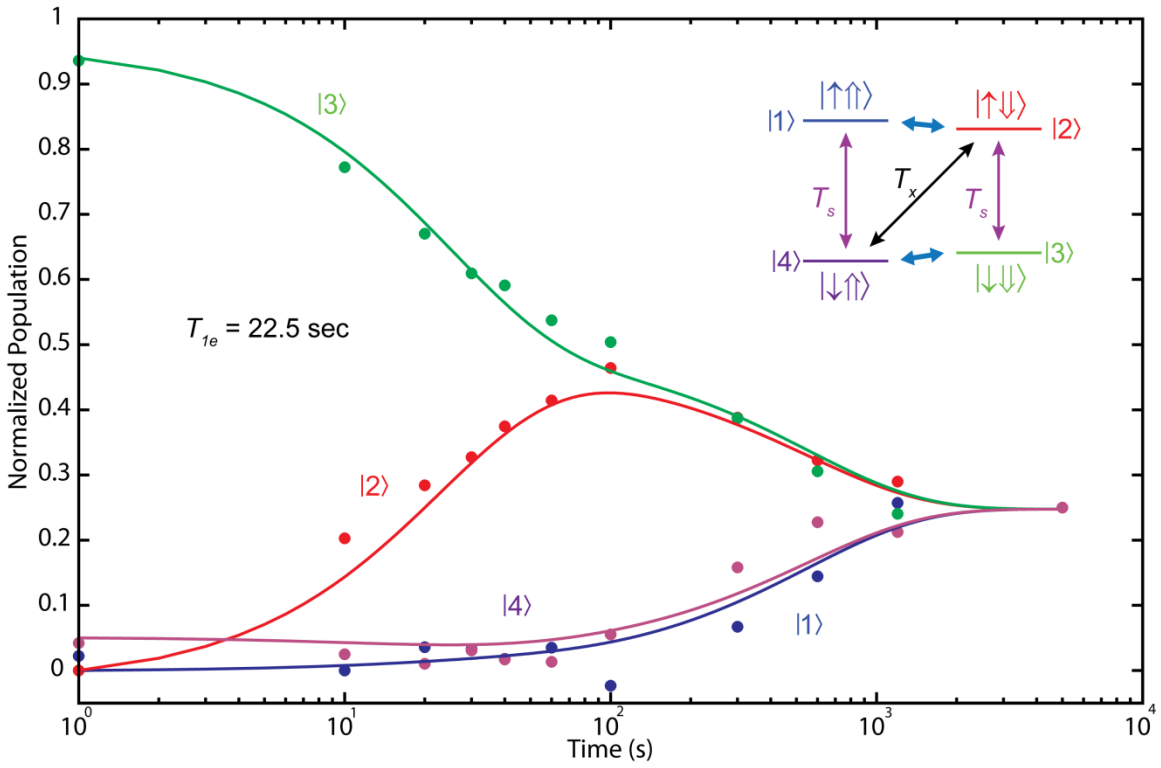

Figure 4.20: Evolution of the system polarized into state 3 followed by dark time at T=4.2K for the ^{28}Si-Avo sample

Discussion:

Performing these measurements made us realize that the simple idea of measuring the 4 populations by looking at the PLE transient at the four different readout laser wavelengths was perhaps not the best method. For one, in the absence of above-gap light the quadratic Stark effect from the ionized donors and acceptors gives asymmetric tails that tend towards low energy and make it more difficult to measure, for example, the intensity of line 3 in the presence of a strong line 4, than it is to measure the opposite. Also, when moving the laser from one line to other there are issues as to whether the laser is exactly tuned to the peak of each line. We realized that when measuring the nuclear polarization the SNR is higher when we have the laser on the high energy component of a doublet (line 4 or line 10) to measure the one component, and then simply flipping the nuclear populations with a π pulse to measure the other component. Thus the precision of the laser tuning to the line peak is irrelevant. We still

retain the advantage of the optical method of measuring populations directly, instead of population differences. Ultimately, if we had the ability to apply microwave (MW) π pulses as well, we would obtain the cleanest result by leaving the laser fixed to line 4, and measuring the signal there with and without the appropriate RF and MW π pulses.

4.7.3. Effect of room light on the ionization of D^0 and neutralization of D^+ in the Avogadro sample

Photoneutralization: At the low impurity concentrations used here, donor-acceptor-pair recombination is very slow [164]. After illumination with above-gap light the majority of the donors and acceptors will remain neutral for very long times in the absence of light capable of photoionizing the impurities, although it is possible that some recombination, and thus loss of D^0 population, takes place during the long dark times. As the temperature was lowered from 4.2K the AEDMR signals rapidly weakened, requiring the application of a small amount of 1047nm radiation during the polarization and readout periods. We believe that this change with temperature resulted from the formation of overcharged acceptor centers (A^+) on the excess boron, since the problem was absent in n-type material, and the A^+ centers have a very small binding energy [161], explaining the temperature dependence.

Note that the lasers tuned to lines 4 and 6 will, in addition to any resonant D^0X creation, also cause a very weak nonresonant photoionization of all D^0 and A^0 via their photoionization continua. The A^+ formed by free hole capture on A^0 would compete with D^+ in capturing e^-, forming acceptor bound excitons (A^0X), and then via Auger recombination A^- and h^+, resulting eventually in all of the donors becoming ionized in the absence of above-gap excitation.

In order to investigate the dynamics of neutral P donors; after preparing the system into the $|\downarrow\Downarrow\rangle$ state we have looked at the change in the neutral signal (through applying phase shifted $RF_\downarrow$ (~61 MHz) $\pi/2$ pulses) and read out the neutral population in the state 3 ($|\downarrow\Downarrow\rangle$) and 4 ($|\downarrow\Uparrow\rangle$) followed by the variation of dark times. We have repeated the above sequence for the read out except this time the systems is prepared in the $|\Uparrow\rangle$ state and the ionized signal monitored by applying phase shifted RF^+ (~1.4 MHz) $\pi/2$ pulses. The results of these experiments are shown in the Figure 4.21.

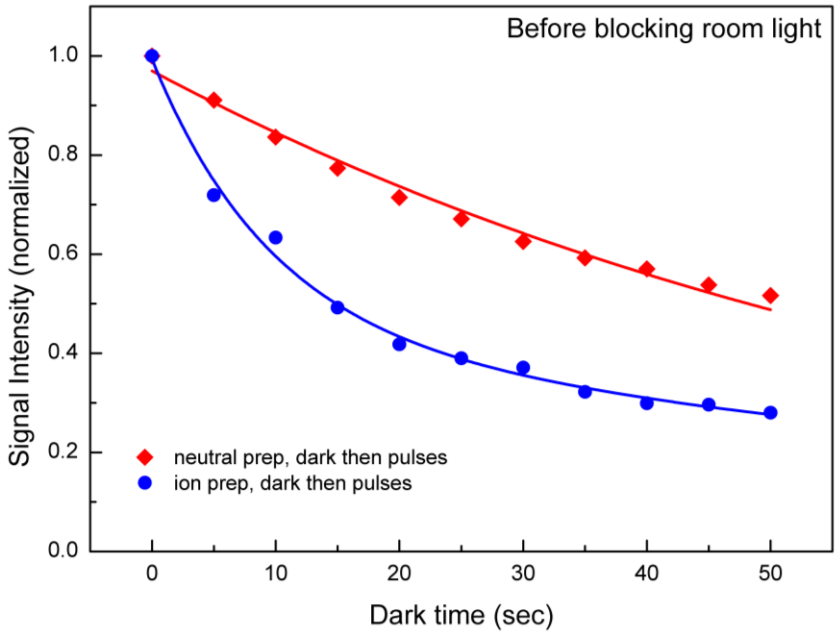

Figure 4.21: P donor's dynamics before solving the room light problem at 4.2K.

It should be mentioned that the above described experiment was done before discovering that even very little room light leakage to the sample is enough to photo-neutralize the ionized donors (D^+) and violate the dark condition.

Since in the Avogadro sample the concentration of boron acceptors is one hundred times that of the ^{31}P donors, one would expect that in equilibrium at temperatures of 4.2 K and below all of the donors would be ionized, along with an equal number of acceptors, but donor-acceptor-pair recombination in Si is a very slow process at such low concentrations [164]. Indeed, during the present study we realized that a significant part of the decay of the neutral donor signal seen in our previous study [54] in fact resulted from this slow ionization of the D^0 (shown in Figure 4.22 red data (2) decay). In our initial efforts to study D^+ we observed a slow loss of the ionized donor population at 4.2K on a similar time scale (shown in Figure 4.21). We discovered that this was due to photoneutralization from very low levels of above-gap light (referred to as room light) reaching the sample, which was eliminated by adding a global shutter immediately in front of the dewar window, and taking other measures (the IR absorber used in the He stack to keep the black body radiation level very low on the sample) to

suppress background light. After these improvements the loss of D^+ at low temperature became undetectable, as seen in Figure 4.22 (blue data (1)).

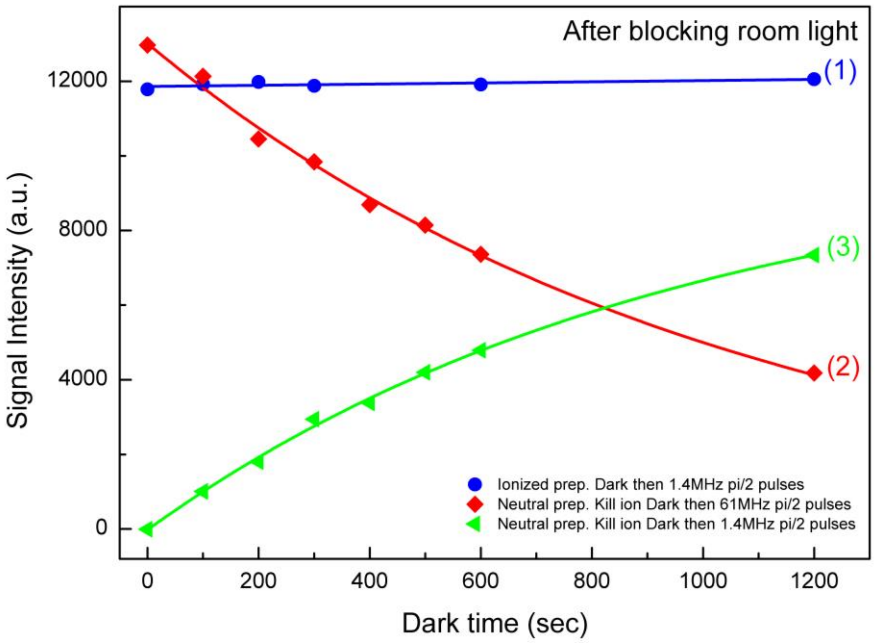

Figure 4.22: P donor dynamics after solving the room light problem at 1.9K for a p-type ^{28}Si-Avo sample

Due to the fact that our neutral P^0 preparation is not as efficient as our ionized P^+ preparation, to see the dynamics of neutral P donors more easily, we added a stage ("kill ionized signal") to suppress the ionized signal to our normal neutral preparation sequence via applying continuous RF^+ frequency for a few milliseconds to scramble the P^+ signal.

The dominant process in the dark is the ionization of D^0 due to donor-acceptor-pair recombination (very sample dependent), resulting in a ~20% loss of D^0 in 300 s (data set #2), even though the actual T_1 is expected to be much longer. Interestingly, the build-up/rise in the ionized signal (data set #3) is equal to the ionization process decay (which is still happening in the dark) of the neutral signal. The 1/e of donor-acceptor-pair recombination is ~17min for our sample in this field and temperature and there is no sign of neutralization of the D^+ (data set #1).

4.7.4. T_1 results of D^+ in the p-type ^{28}Si-Avo sample

In Figure 4.23 we show the D^+ nuclear spin T_1 measured at 1.9 K and room temperature. The Hahn echo sequence is replaced with either no operations, leaving the nuclear spin polarization unchanged, or a π pulse, which inverts it (explained in the Methods Chapter).

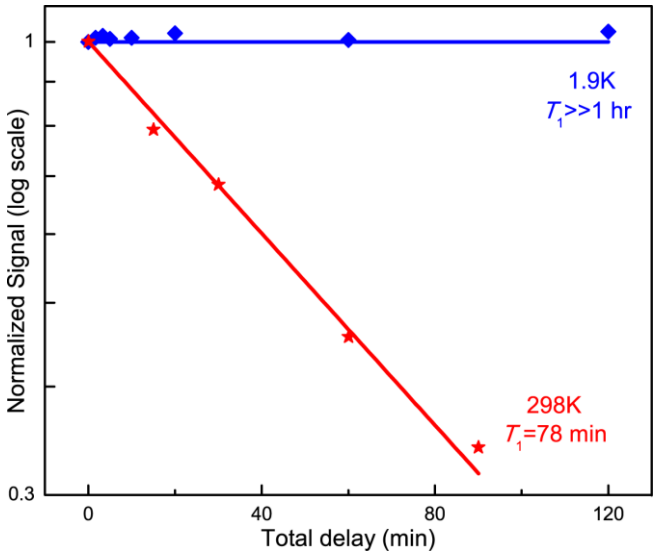

Figure 4.23: The decay of the nuclear spin polarization (along Z), parameterized by T_1, is shown for 1.9 and 298 K.

The D^+ T_1 at cryogenic temperature was so long that no decay could be observed over 2 hours, and at room temperature T_1 was over an hour. Even a short thermal cycle up to room temperature and back resulted in a ~30% loss in nuclear spin polarization as compared to the same measurement at a constant 4.2 K, so all room temperature decay data are normalized to unity for the shortest time (2 min at 298 K).

4.8. Measurement of D^0 and D^+ NMR parameters

Our preliminary investigation of optically polarized/optically detected NMR of neutral ^{31}P donors in n-type ^{28}Si 3.3.6 sample began with the simplest possible arrangement, which we refer to as CW NMR [137]. In this setup, the pump and probe

lasers are set to pump 6 and probe 4 (or pump 8 and probe 10) and left on continuously. The RF signal driving the oscillating *B*-field is also on continuously and is scanned across the expected $RF_{\downarrow}$ ($RF_{\uparrow}$) resonance frequency, while we monitor the PLE signal generated by the probe laser. An example of a CW NMR resonance for the $RF_{\uparrow}$ branch is shown in Figure 4.24. The resonance could be easily detected even when hand scanning the RF frequency across the resonance, but note that very low RF power levels had to be used in order to avoid power broadening of the resonance.

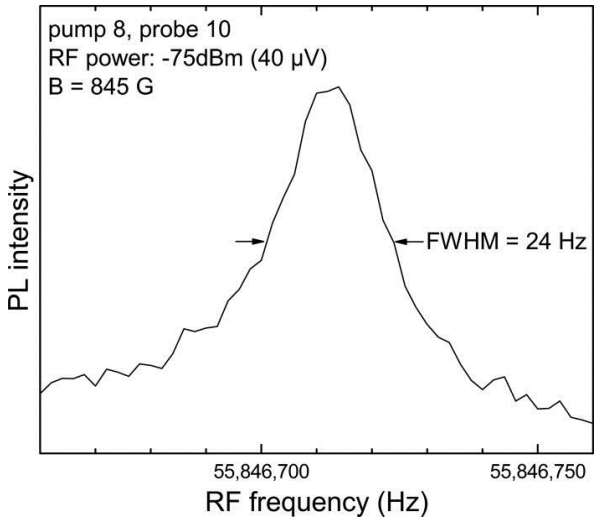

Figure 4.24: Preliminary result of CW optically detected NMR showing an increase in the signal when probing line 10 and pumping line 8 as the frequency of RF field is tuned across the $RF_{\uparrow}$ resonance.

However, we emphasize that the values of $RF_{\uparrow max}$ and $RF_{\downarrow min}$ determined by CW NMR and shown in Figure 4.24 are not as precise as those determined later by pulsed NMR, for several reasons. First, a Rb clock reference was added after the CW NMR measurements. Second, the requirement of very low RF power during the CW NMR measurements resulted in very long scan times, and spectra which were skewed depending on the direction of the RF scan. Finally, having both lasers on during the application of the RF will produce some sample heating, which we will later show may affect the precise value of the hyperfine constant, A.

4.8.1. *Rabi experiment results*

To demonstrate coherent control, we apply a single RF pulse of varying duration to observe Rabi oscillations (Figure 4.25). Usually this simplest pulsed NMR experiment is performed after finding the resonance frequency using CW NMR.

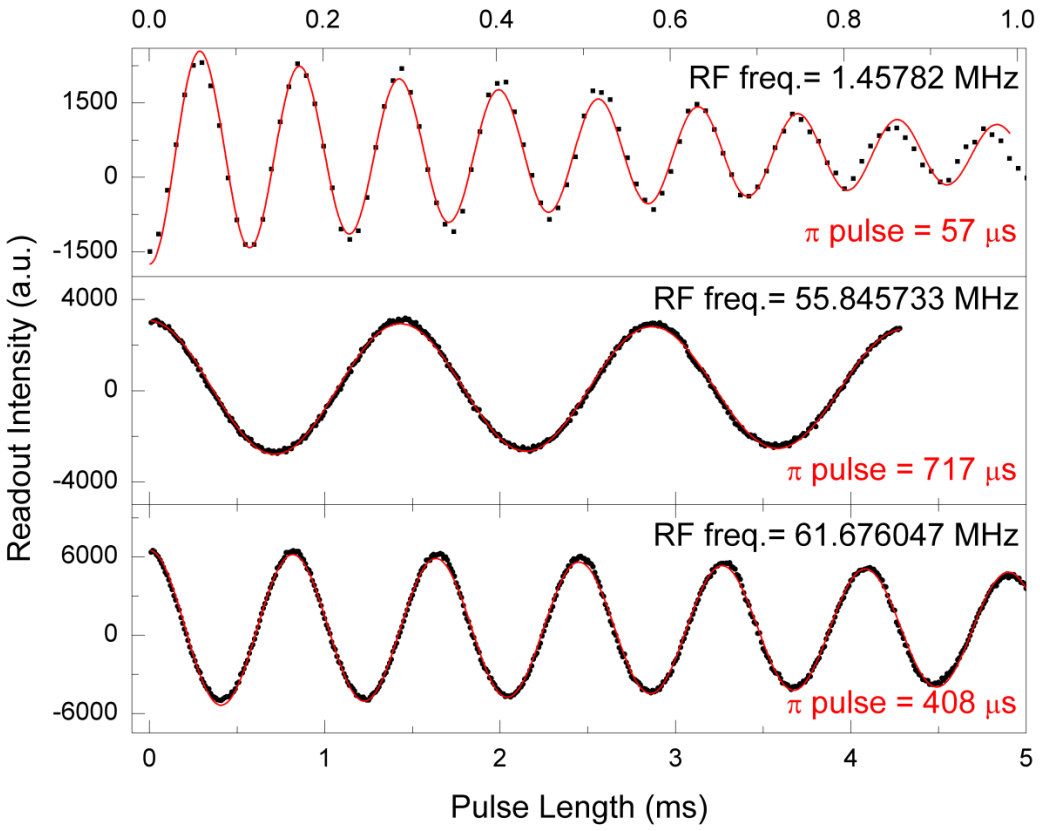

Figure 4.25: ***Shows the Rabi oscillation of three RF frequencies (RF^+ for ionized P^+ (top), $RF_\downarrow$ and $RF_\uparrow$ for neutral P^0 (bottom and middle)) at T=4.2K.***

As explained in Chapter two, from the frequency of the Rabi oscillation, assuming fixed RF power, we can extract the RF π pulse length, while the decay of sinusoidal oscillation will give the inhomogeneity in the RF field. These single shot Rabi oscillation results shown in Figure 4.25 are necessary to fine tune the appropriate π pulse length for use in subsequent experiments (for instance Hahn echo or XY16 decoupling pulse sequences) that measure T_2 coherence times.

Confirmation that these are in fact Rabi oscillations comes from the observed linear dependence of the resonant Rabi frequency with the applied RF amplitude. Figure 4.26B shows the expected linear behaviour with RF amplitude of the Rabi frequencies extracted from the data in Figure 4.26A.

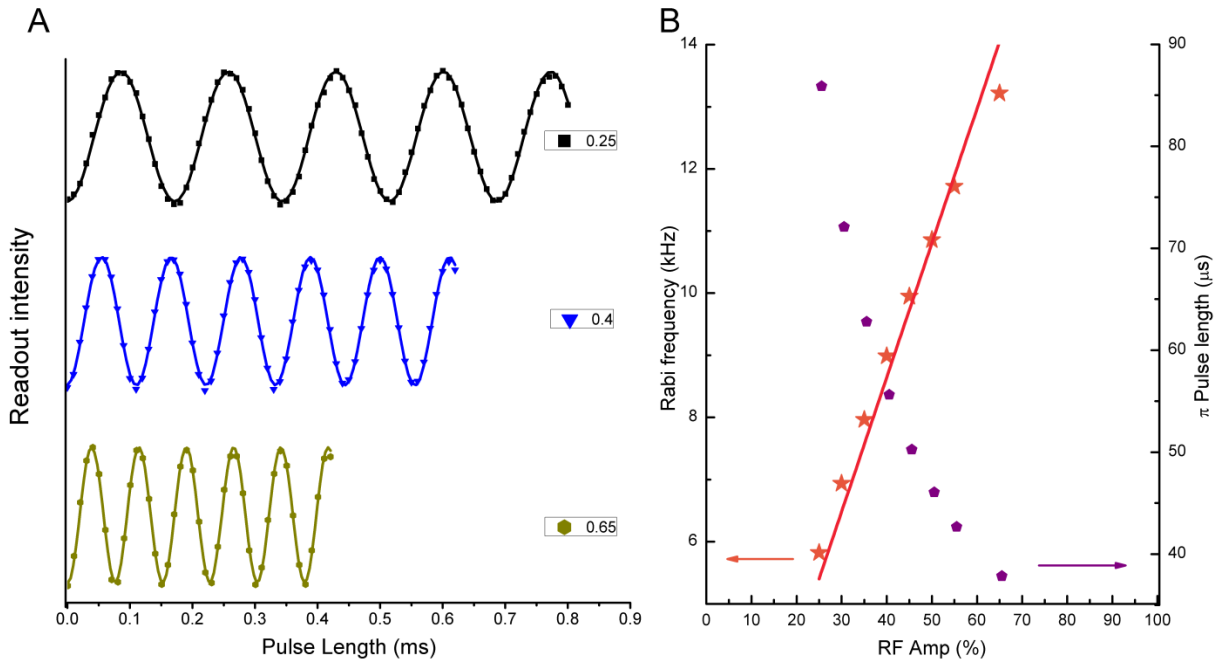

Figure 4.26: ***(A) Ionized P Rabi oscillations and power dependence of the Rabi frequency at T=2.1K, (B) Rabi frequency versus the radio wave excitation amplitude, with a fit displaying the linear relationship.***

Away from resonance, the oscillations have a higher frequency and lower amplitude. The is because off-resonance $\pi/2$ pulse can be thought of as tipping magnetization less than $\pi/2$ rads., so the magnetization vector will precess around a smaller circle on the Bloch sphere, resulting in a smaller projection, as shown in Figure 4.27. Also, Figure 4.27 shows that it is very important to be on resonance before trying to find the π pulse length because as the frequency becomes off resonance, apart from the obvious drop in the signal intensity, the required π pulse length will be smaller too (100μs instead of 125μs) due to the pulse flipping the spins around the smaller angle in the Bloch sphere.

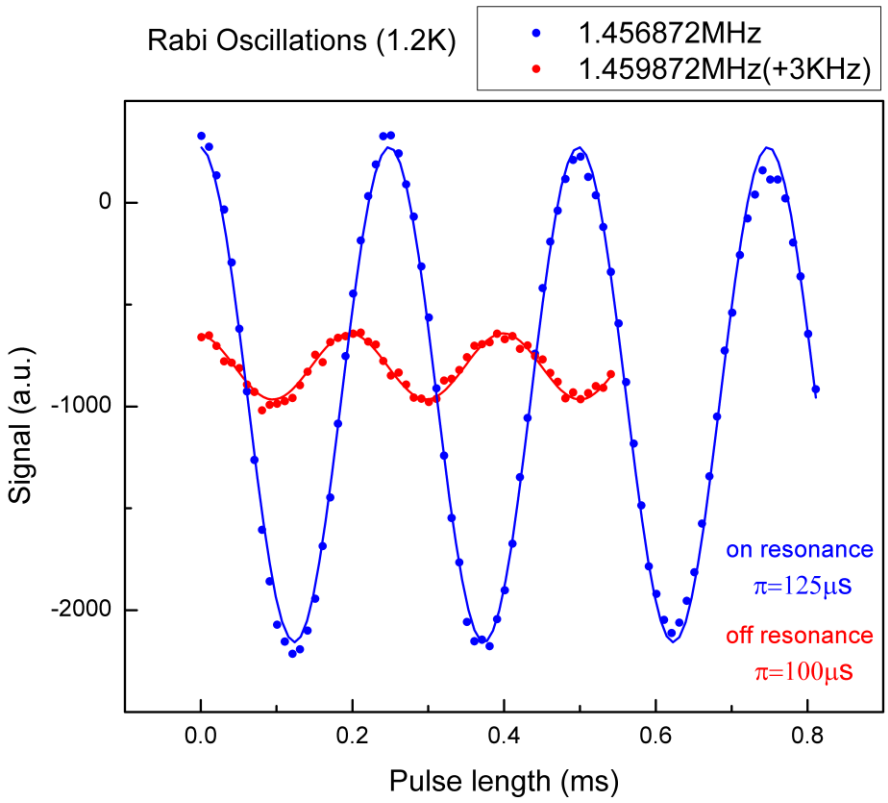

Figure 4.27: Comparison of Rabi oscillations on and off resonance frequency at T=1.2K.

Coil Geometry

In a normal NMR experiment, the sample sits inside a coil which is part of a tuned circuit which delivers RF pulses to the sample and detects the FID from the precessing spins in the sample. The detection method is not the same in our experiment because we are projecting the RF signal onto the polarization axis and are measuring the spin dependent recombination through an impedance change in the sample. The RF fields (B_1) delivered by the coil must be perpendicular to the static magnetic field, B_0. If the coil was big enough or sample was small enough that the RF field seen by the sample was completely homogeneous then there should be no decay in the Rabi oscillations (or a slower decay at least). In Figure 4.28, the beating in the Rabi oscillation is due to inhomogeneities of the RF magnetic field (B_1) felt by the sample.

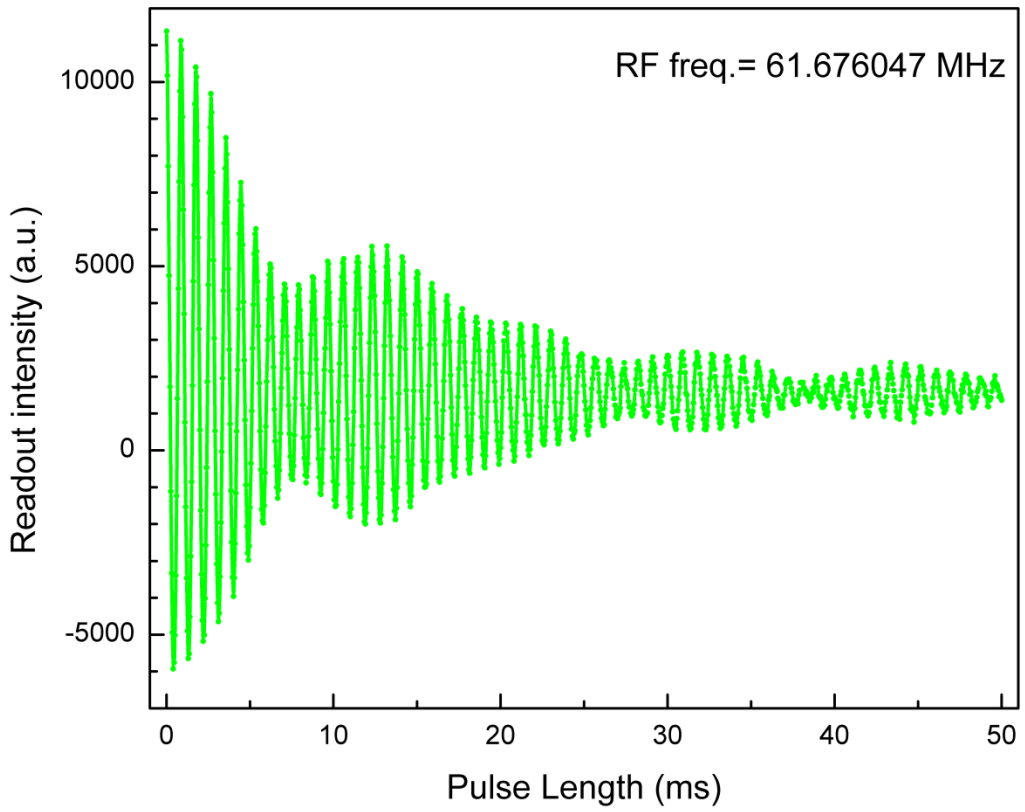

Figure 4.28: Beating in the Rabi oscillations due to inhomogeneities in the B_1 field at T=4.2K.

We then changed the solenoid RF coil to a Helmholtz[8] configuration. As expected, the B_1 homogeneity inside the Helmholtz coil is much better than previous solenoid. Rabi oscillations of P^0 and P^+ in the small ^{28}Si-Avo sample for the Helmholtz coil shielded by copper tube inside the dewar between the shimmed electromagnet are compared with the solenoid ones in Figure 4.29. For further improvement we could have used a Maxwell coil[9] at the expense of more complexity.

[8] A Helmholtz pair consists of two identical circular magnetic coils that are placed symmetrically one on each side of the experimental area along a common axis, and separated by a distance equal to the radius of the coil which is what defines a Helmholtz pair. This arrangement minimizes the nonuniformity of the field at the center of the coils.

[9] A Maxwell coil which has an extra coil in the middle of two Helmholtz pair, is an improvement of a Helmholtz coil; it provides an even more uniform magnetic field than a Helmholtz coil.

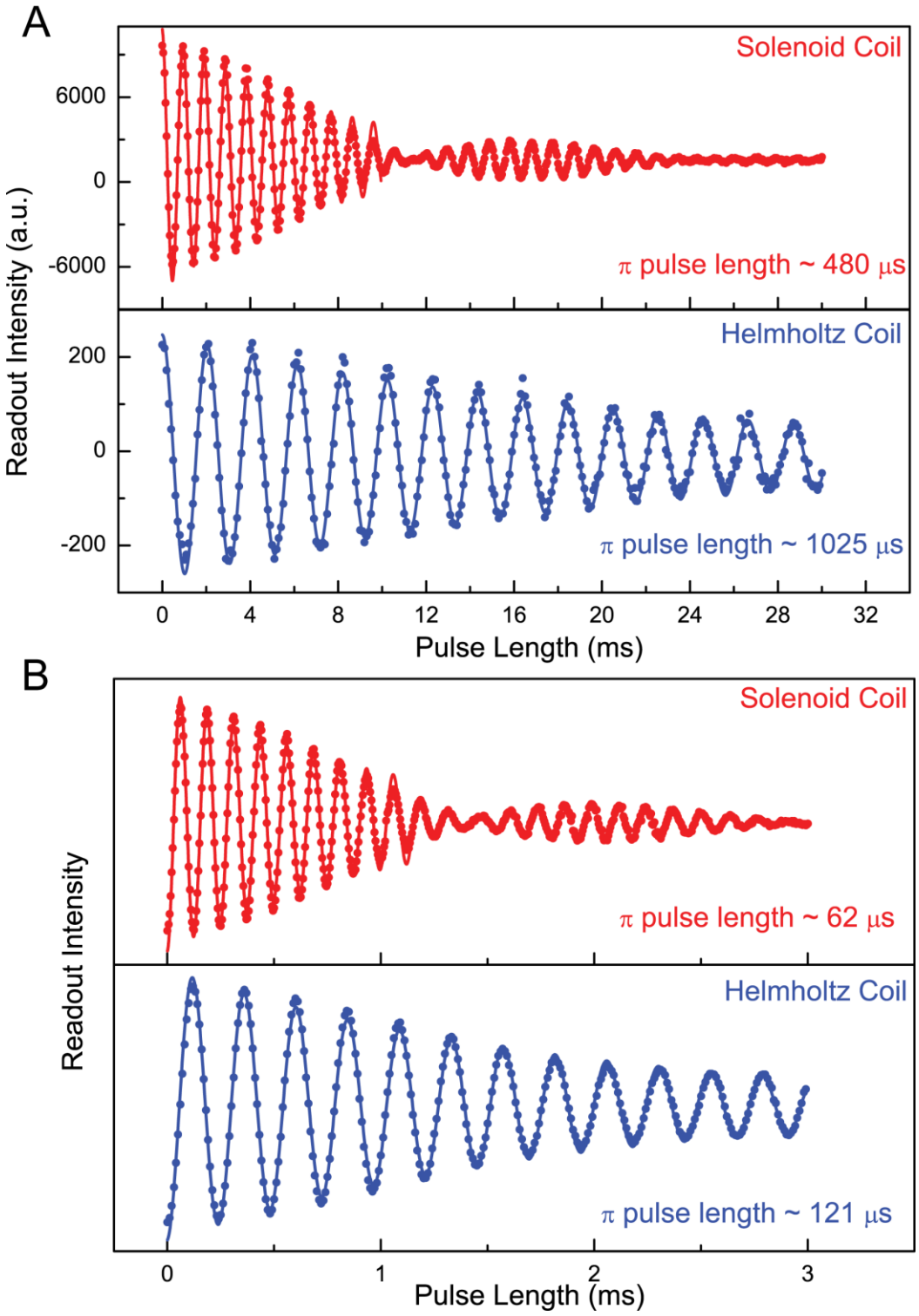

Figure 4.29: ***Effect of coil geometry on the beating of the Rabi oscillations. This is due to inhomogeneities of B_1 field which is the reason for beating in the Rabi oscillations of neutral P^0 (A) and ionized P^+(B).***

4.8.2. *Ramsey experiment results*

The Ramsey fringe measurement to determine T_2^* is very similar to the T_1 measurement, but the time evolution occurs between two $\pi/2$ pulses, and the RF frequency is offset from the actual resonance frequency by a known amount in order to produce fringes with a suitable period. The Ramsey experiment as explained in Chapter two is the simplest two pulse free induction decay (FID) experiment. To perform a Ramsey experiment first we polarize the system into a pure state and then prepare a coherent superposition state by applying a $\pi/2$ pulse. The echo signal (which we are using a second $\pi/2$ pulse to project on to the polarization) is measured for different delay times in order to determine the exact resonant frequency of the transition by examining the frequency of the Ramsey fringes. The decay of the echo signal, shown in Figure 4.30, gives the T_2^* for the system which is not the inherent coherence time by any means for different temperatures.

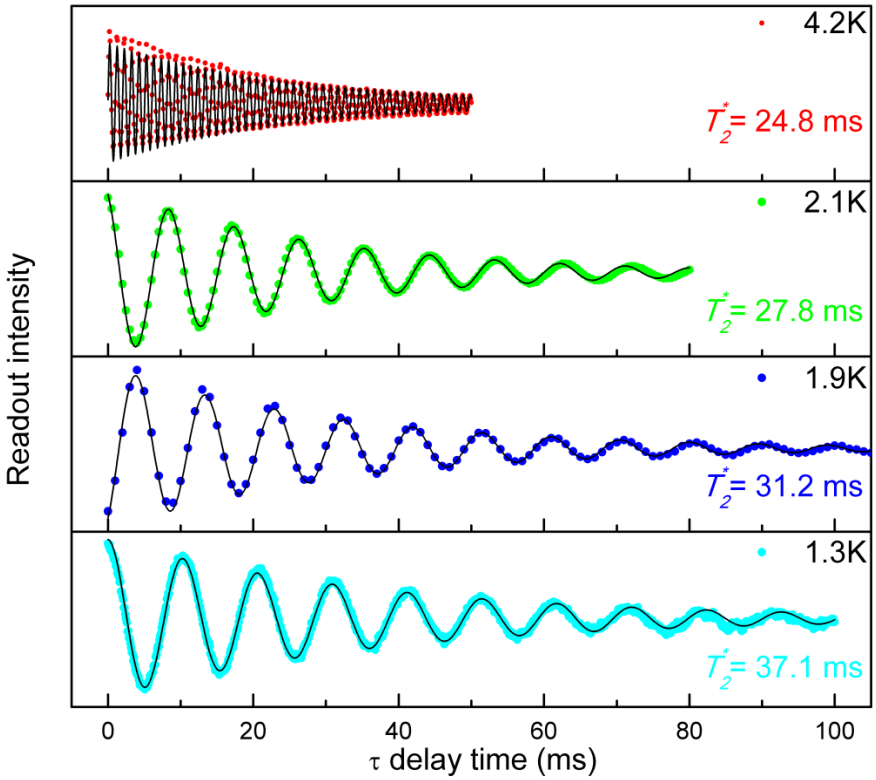

Figure 4.30: Ramsey fringes of the neutral P^0 in the ^{28}Si-Avo sample at different temperatures.

It should be emphasized that each data point in Figure 4.30 comes from a single measurement, with no signal averaging. The reason for the temperature dependence of T_2^* is not completely clear. Yet Figure 4.30 indicates that by reducing the temperature below 4.2K (and the λ point (2.1K)) the T_2^* of the system can be improved. This is something that needs more examination as it is not simply the broadening of the transition lines above the λ point that causes the decrease *of* T_2^*.

It is interesting to note that the T_2^* ratio of the p-type ^{28}Si-Avo sample to the n-type ^{28}Si:^{31}P slice 3.3.6 sample [137] (37.1ms / 16.4ms = 2.26) is in very good agreement with the inverse FWHM ratio of their optical transitions at low temperature (0.0017cm^{-1} / 0.00076 cm^{-1} = 2.24).

Effect of shimming electromagnet on the Ramsey fringe results of P^0 and P^+

Unlike the neutral P case, there does not exist a clock transition for ionized P, so the T_2^* coherence time will be directly affected by the B_0 field homogeneity of the system. Hence, we expected to see a drastic change in the T_2^* values when using different magnets with different static field homogeneities (electromagnet and split pair superconducting magnet).

Comparing the results of our two magnet setup shows that homogeneity of the magnetic field for the superconducting magnet (Ramsey results shown in Figure 4.31) is far worse than our electromagnet after shimming, as expected; optical-access split-pair superconducting magnet dewars are not meant for NMR experiments and the homogeneity is not comparable to NMR magnets.

The fits to the data shown in Figure 4.31 and 4.32 are sinusoidal, which gives the fringe frequency, multiplied by an exponential decay, which gives T_2^*. The applied RF frequency in each case was the nominal expected resonance frequency plus or minus a shift which should equal the observed fringe frequency. The exact resonance frequency under the experimental conditions of the scan is the given by the applied RF frequency minus or plus the observed fringe frequency.

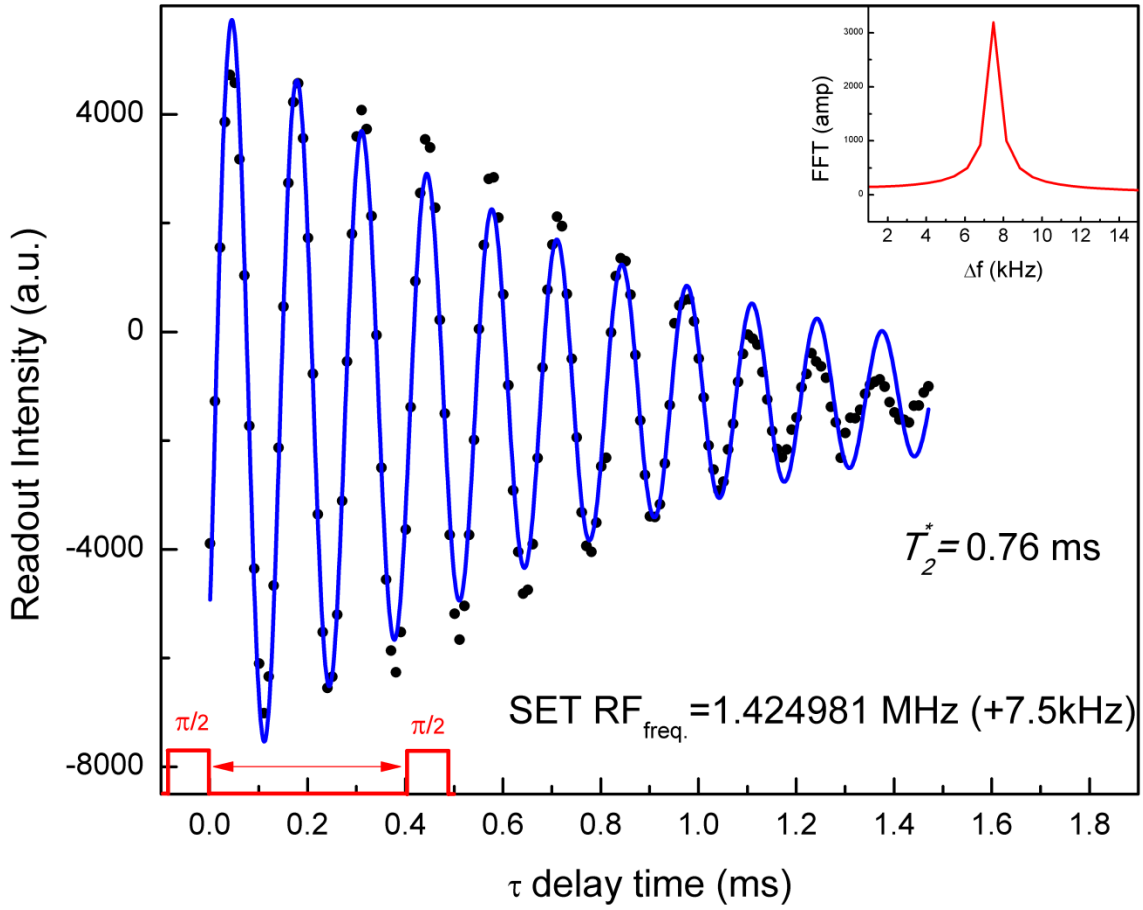

Figure 4.31: Ramsey Fringes for ionized P in the superconducting magnet at T=2.1K.

The increase in T_2^* from improving the B_0 homogeneity by shimming is large for D^+, but negligible for D^0, as the D^0 measurements take place at a clock transition. Comparing the Ramsey fringes of neutral P before and after shimming the magnet (Figure 4.32A,B) shows no significant change in T_2^* (~35ms), confirming that neutral P are protected from magnetic field fluctuations by operating at a B_0 field corresponding to RF clock transitions. The Ramsey fringe decay results of D^+ before shimming show beating (Figure 4.32C) due to poor homogeneity of the B_0 static magnetic field.

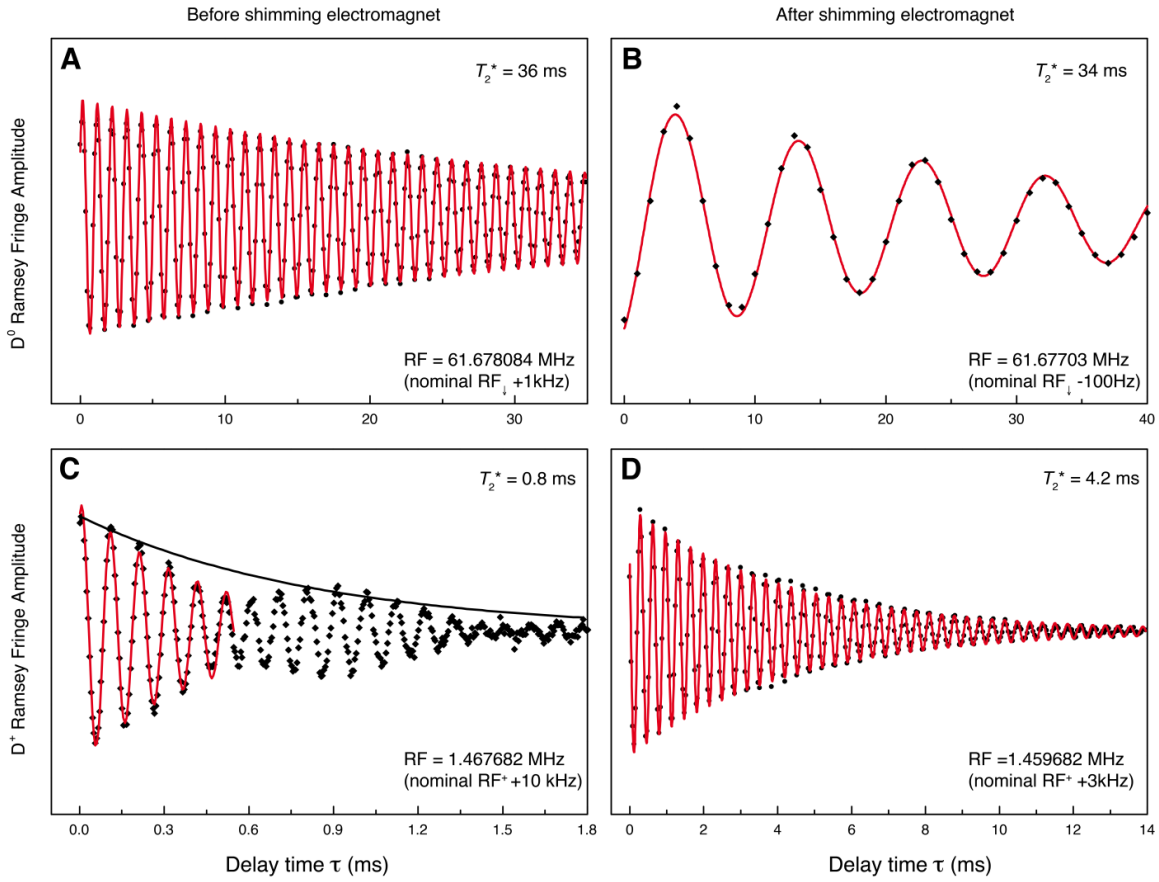

Figure 4.32: ***Ramsey fringe scans for D^0 on the $RF_{\downarrow}$ transition and for D^+ are shown in A to D before and after improving the B_0 homogeneity by placing circular ring shims on the electromagnet.***

4.9. The T_2 coherence time measurements of neutral D^0 and ionized D^+ nuclear spins using the Hahn echo method

In order to remove the effects of static dephasing and measure T_2, we implemented a simple three-pulse Hahn echo measurement, as discussed in Chapter two. For this experiment the RF frequency was set exactly to $RF_{\downarrow min}$ or $RF_{\uparrow max}$ as determined by the previous two-pulse Ramsey measurements, and B was set to B_0. To avoid the drift problems inherent in DC measurements, for each delay two measurements were taken, one with all three pulses having the same RF phase, and

one in which the phase of the first $\pi/2$ pulse was inverted, with the reported signal being the difference between these two measurements.

4.9.1. *Hahn echo T_2 results for D^0 in n-type ^{28}Si samples*

The preliminary results of the Hahn echo measurement on the $RF_{\downarrow}$ branch are shown in Figure 4.33 for two (n-type) P-doped ^{28}Si samples (slice 3.3.2 and 3.3.6 with the latter having higher P concentration).

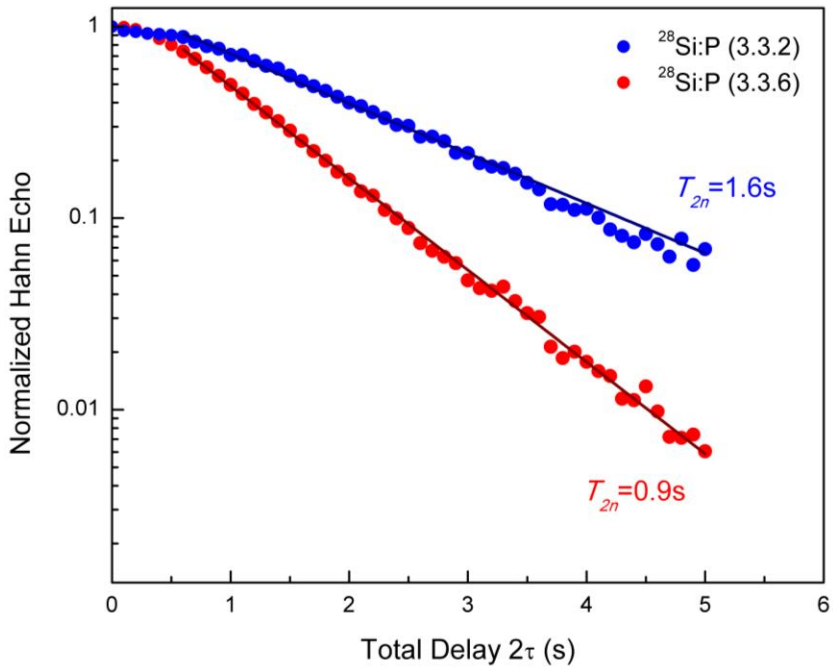

Figure 4.33: ***The preliminary results of a three pulse Hahn echo measurement of the nuclear T_2 on the electron spin down branch at T=1.3K.***

A measurement on the $RF_{\uparrow}$ branch gave identical results within the noise level. The T_2 coherence time was found to be ~900 ms and 1.6 s for n-type ^{28}Si:P 3.3.6 ([P]~7×10^{14}) and 3.3.2 ([P]~3×10^{14}) samples respectively. The T_{2n}=1.75 s reported for ^{31}P in ^{28}Si as measured by an electron nuclear double-resonance (ENDOR) technique at a higher field [60] is consistent with our result for the ^{28}Si:P 3.3.2 sample with similar P concentrations.

4.9.2. *Hahn echo T_2 results for D^0 in ^{28}Si-Avo sample*

The reported T_2 is found to be inversely proportional to the donor density [53]. This motivates the study of coherence lifetimes at even lower donor densities; however, densities of 10^{13} cm^{-3} are at the limit of detection by conventional electron spin resonance (ESR) and ENDOR.

Two RF$_{\downarrow}$ pulses were applied to implement the Hahn echo sequence, with a final $\pi/2$ RF$_{\downarrow}$ pulse for readout. If the nuclear spin has remained coherent, all population is returned to state $|3\rangle$ (where we prepared); otherwise it becomes equally (and incoherently) distributed between states $|3\rangle$ and $|4\rangle$. The readout stage therefore measures the difference between the areas of the $|3\rangle$ and $|4\rangle$ photoconductive transients (Figure 4.34A). By varying the delay τ in the Hahn echo sequence, we obtain a T_{2n} of 44 s at T = 1.74 K (Figure 4.34B).

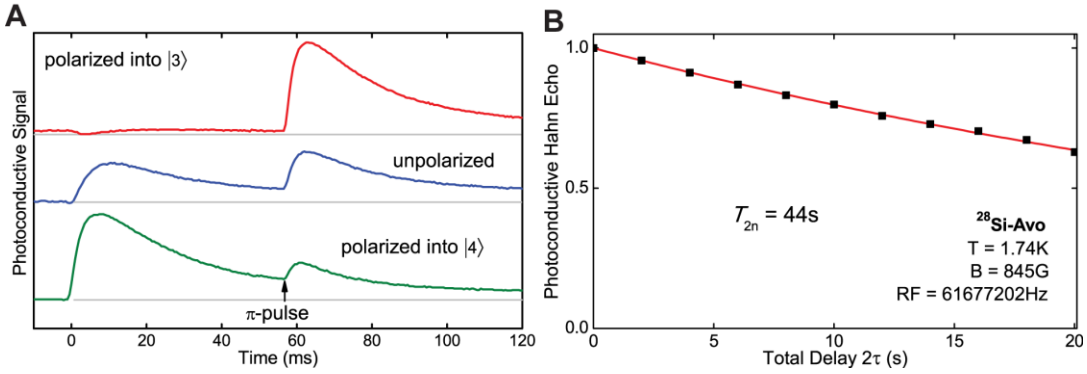

Figure 4.34: ***(A) Single-shot photoconductive readout transients for the system polarized into either states $|3\rangle$ or $|4\rangle$ or unpolarized. (B) Single-shot measurements of the Hahn echo decay at T = 1.74 K, with an exponential fit for p-type ^{28}Si-Avo sample.***

4.9.3. *Hahn echo T_2 coherence time results for D^+ in ^{28}Si-Avo sample*

Figure 4.35 shows single-shot Hahn echo decay data at 4.2K revealing increasing phase noise with increasing delay time, probably arising from low-frequency magnetic field fluctuations. This phase noise was eliminated from the 1.9K data by

using maximum magnitude detection (explained in the previous Chapter). The Hahn echo T_2 of about 30s measured at or below 4.2K is well explained by spectral diffusion due to the residual (46 parts per million) ^{29}Si nuclear spins present in the sample [86]. Also shown is single shot Hahn echo data at room temperature, where the long cycle time made the use of maximum magnitude detection impractical, so that the phase noise could not be eliminated, and the apparent Hahn echo T_2 was reduced to ~8 s.

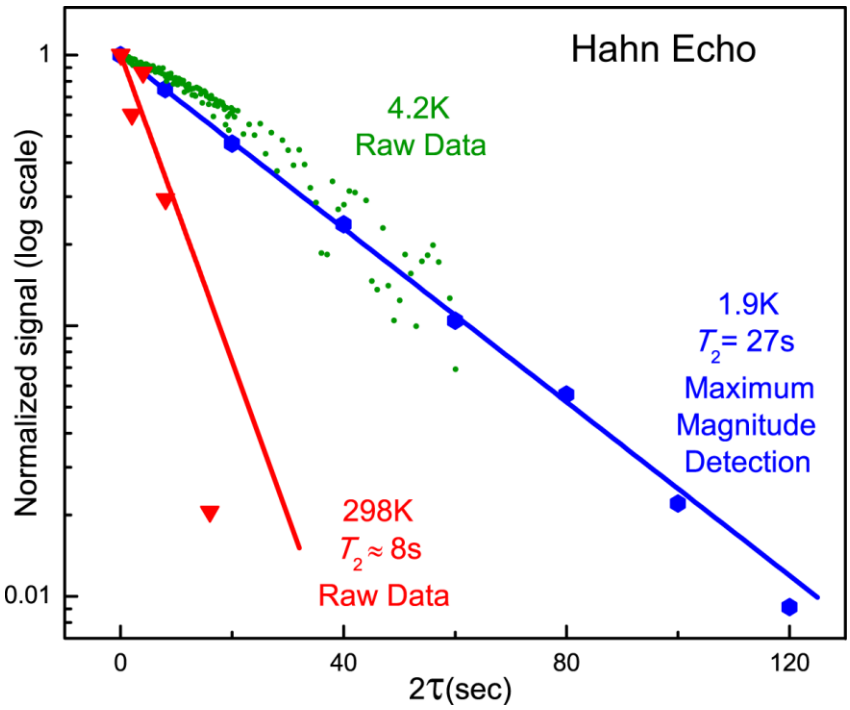

Figure 4.35: ***Single-shot Hahn echo T_2 measurements are shown at 298 and 4.2K, the latter (green dots) showing increasing phase noise with increasing delay. The effect of phase noise can be suppressed by using maximum magnitude detection, as shown for data taken at 1.9K.***

The Hahn echo sequence can only refocus the effects of inhomogeneities which are essentially static, and longer coherence times can be obtained by other techniques as will be discussed in next section.

4.10. T_2 coherence time measurement of D^0 and D^+ using XY16 dynamic decoupling in ^{28}Si-Avo sample

Just as the Hahn echo sequence removes the effects of a static distribution of precession frequencies, dynamic decoupling, through a periodic reversal/refocusing of the spins' interaction with the environment, can mitigate/eliminate the effects of environmental fluctuations on a time scale slower than this period [157, 158, 165]. We have shown that a repeated/periodic, relatively simple series of $\pm\pi$ rotations around the orthogonal X and Y axes with equal delays (τ) between all π pulses, known as XY-16 [159], is remarkably resistant to degradation due to pulse errors, and can protect an arbitrary coherent initial state against decay. Figure 4.36 shows that XY16 sequence compensates for π pulse length error as long as the error is reasonably small.

$$[XY16]^n=[(\pi_x)\tau(\pi_y)\tau(\pi_x)\tau(\pi_y)\tau(\pi_y)\tau(\pi_x)\tau(\pi_y)\tau(\pi_x)(\pi_{\bar{x}})\tau(\pi_{\bar{y}})\tau(\pi_{\bar{x}})\tau(\pi_{\bar{y}})\tau(\pi_{\bar{y}})\tau(\pi_{\bar{x}})\tau(\pi_{\bar{y}})\tau(\pi_{\bar{x}})]^n$$

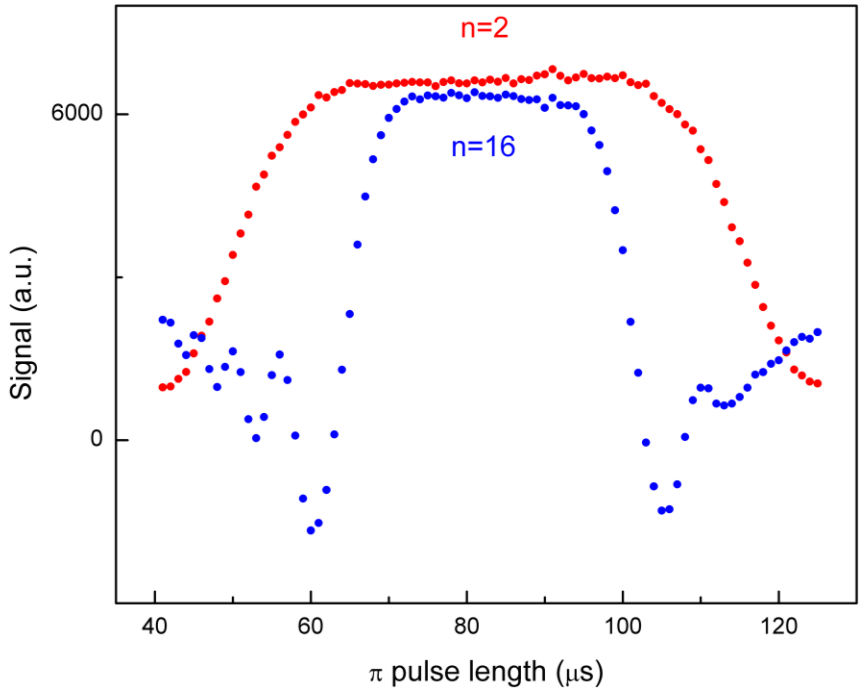

Figure 4.36: Readout signal while scanning the π pulse length in the XY16 sequence with 2 and 16 loops.

Figure 4.36 also shows that by increasing number of XY16 loops (i.e. by using more π pulses), the π pulse length error tolerance of XY16 gets smaller (i.e. the flat area of signal before decaying gets narrower). This means that in order to use more of these π refocusing pulses without introducing the error in the π length to the signal, we need to choose π pulse length more accurately.

Optimizing the parameters in the XY16 pulse sequence

As the time τ between π pulses is reduced, the low frequency B_0 noise is suppressed to an increasing frequency cutoff, but a tradeoff is reached because of the accumulation of pulse errors as the number of pulses grows. For any given XY16 pulse sequence there is an optimal τ delay time between π pulses. It can be obtained by scanning the delay time between the refocusing π pulses in the XY16 sequence, with the fixed number of π pulses (shown in Figure 4.37 for 2 loops of the XY16 which is equal to using 32 π pulses).

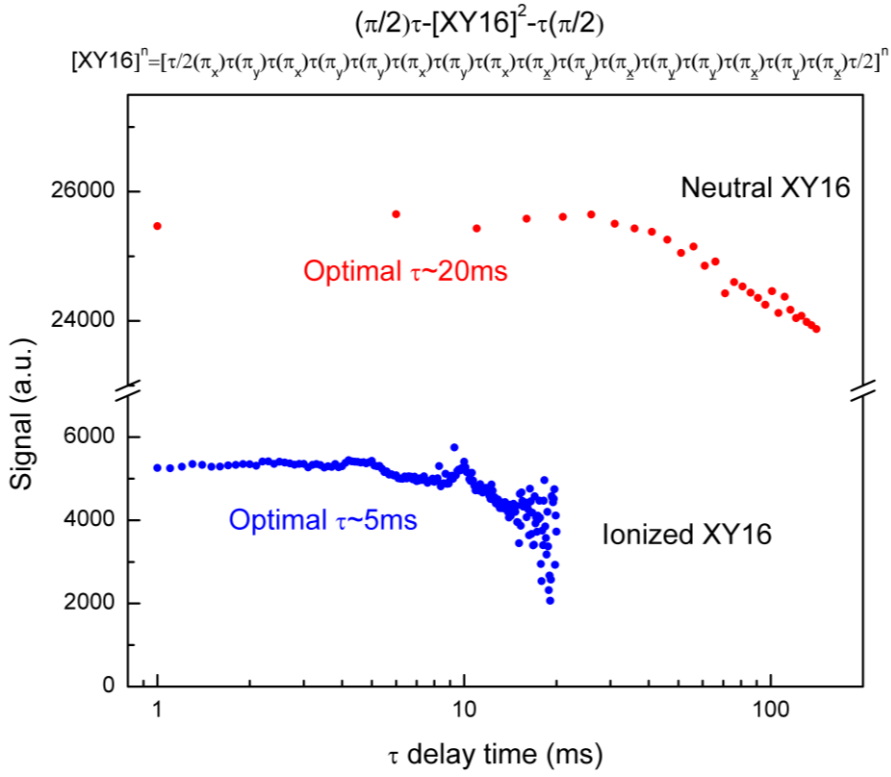

Figure 4.37: The noise profiles of our XY16 sequence for the D^0 and D^+ systems.

4.10.1. T_2 coherence time measurement of D^0 using XY16 pulse sequence

We confirmed (see Figure 4.38) that the XY16 sequence protects arbitrary initial states. The decay of X and Y initial states is seen to be essentially identical. The slower decay of the Z initial state reflects the fact that it is an eigenstate, not a coherent superposition, so it should decay as T_{1n}, not T_{2n}. At this temperature, T_{1n} is many hours, so the observed decay likely results from pulse errors in our XY16 sequence (the 112s delay corresponds to 1120 π pulses), although some loss of D^0 is due to ionization as explained earlier in this Chapter.

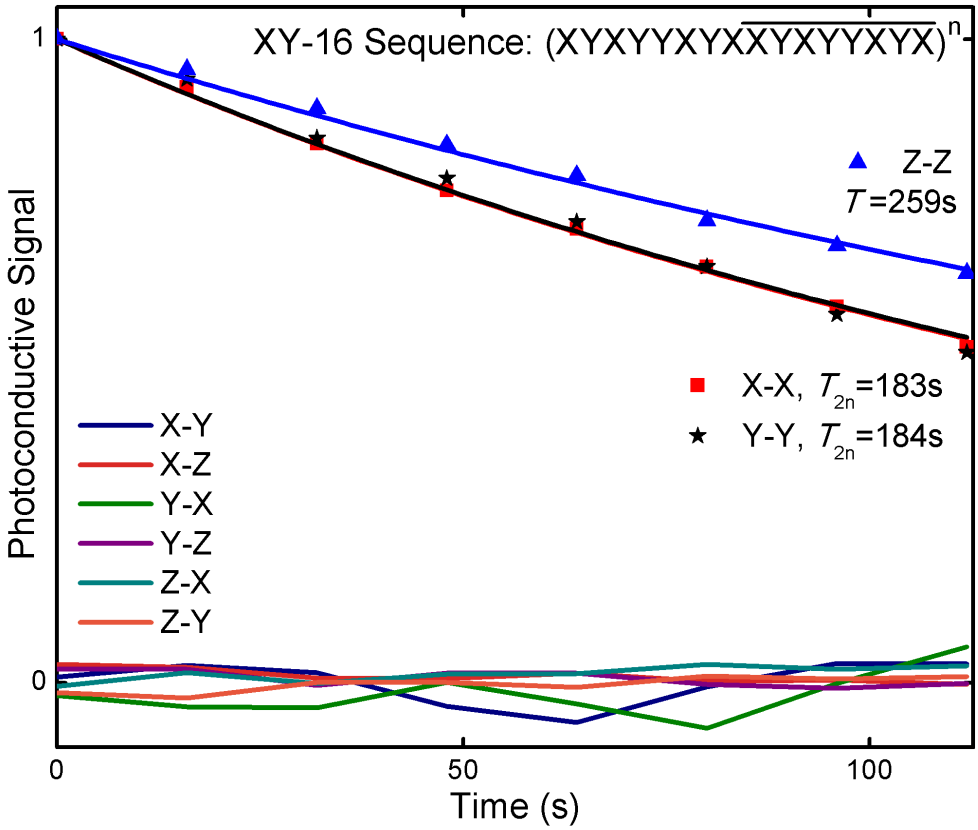

Figure 4.38: ***Evaluating the performance of XY16 dynamical decoupling for D^0 nuclear spins at T = 2.64 K with τ = 50 ms. α and β label the coherent magnetization after preparing the system in state α, dynamically decoupling for some time, and then measuring in the basis of β. The variations in the $\alpha \neq \beta$ data are indicative of the single-shot noise level, not cross-coupling resulting from the XY16 sequence.***

The temperature dependence of the XY16 decoupled T_2 for D^0

The single-shot coherence decays as a function of sample temperature are shown in the Figure 4.39. Because $T_{2n} \leq 2T_{1e}$ [60], the T_{2n} = 44 s at 4.2 K is limited by T_{1e}, which we measure to be ~22 s, in good agreement with earlier studies [84]. Below 4.2 K, T_{1e} rapidly becomes very long [84], and the observed T_{2n} must be limited by other processes, such as the residual ^{29}Si, or P-P dipolar coupling. Nevertheless, the observed T_{2n} becomes as long as 192 s at 1.74 K.

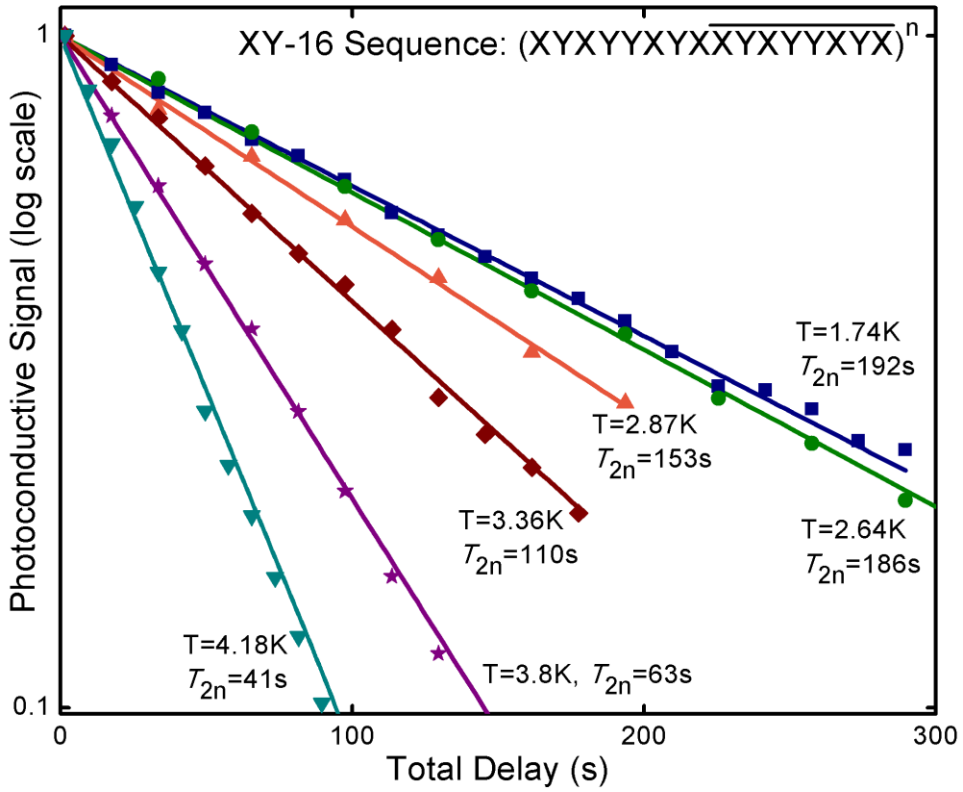

Figure 4.39: ***Coherence decays at several temperatures using the XY16 periodic decoupling sequence indicated at the top, with a delay of τ between all π pulses, where τ = 50ms for these measurements. Also shown are fits to exponential decays.***

The temperature dependence of the XY16 decoupled T_2 times shown in Figure 4.39 can be accurately explained by the sum of a temperature dependent decay rate related to T_{1e} [84] and a temperature independent rate of ~1/200 s^{-1} (illustrated in Figure 4.40). The T_{1e} process is easily understood, causing a direct flip of the electron of the

central coherent spin, which cannot be recovered by dynamic decoupling given the large frequency difference between $RF_{\uparrow}$ and $RF_{\downarrow}$. This process dominates at 4.2 K, limiting the T_2 of 41 s to two times T_{1e}, which was measured under the same conditions to be 22 s. The limiting low temperature T_2 of ~200 s may result from several contributions, one of which is likely to be direct electron flip-flops between coherent 'central' donors which have electron spin down with donors having electron spin up, which would again destroy the coherence almost instantly, and not be recoverable by dynamic decoupling. This process would be suppressed by the degree of electron polarization, but we have determined that under the conditions used in [54], at the beginning of the measurement time ~5% of the donors had incorrectly polarized electrons, and ~5% of the donors were ionized. This is a dipolar process which should scale as the donor concentration, and it is interesting to note that the 230 ms (900ms later) T_2 observed for the n-type sample was approximately 1000 times shorter than the 192 s observed for the Avogadro sample, in reasonable agreement with the ~1000 times difference in ^{31}P concentration.

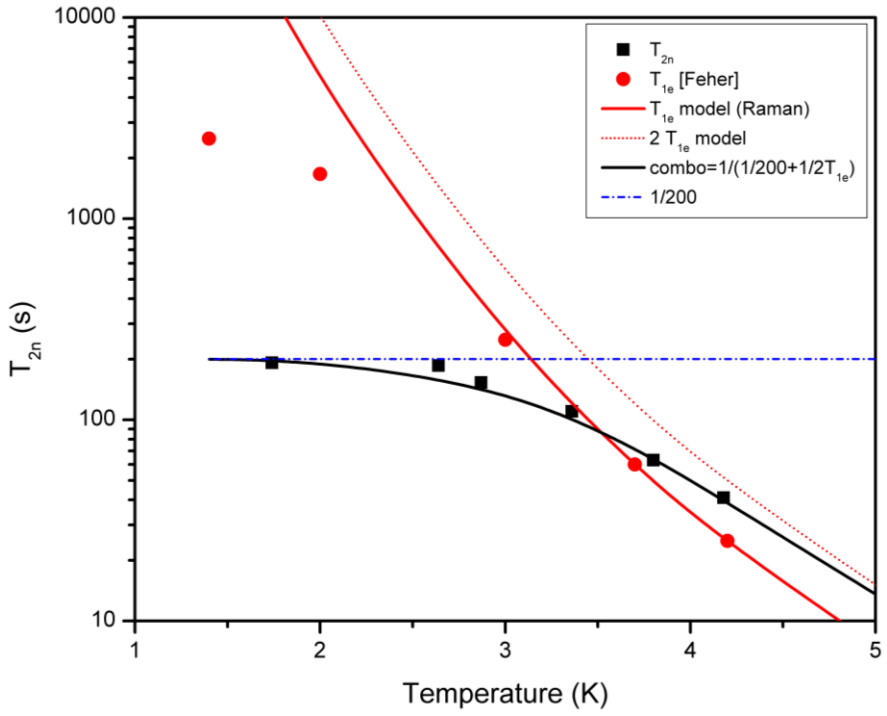

Figure 4.40: The temperature dependence of T_{2n} fitted by a simple model.

4.10.2. T_2 coherence time measurement of D^+ using XY16 pulse sequence

The coherence time of ionized ^{31}P was recently observed in natural Si, and while the nuclear coherence time was indeed much longer than the electron coherence time measured in the same device, it was limited to 18 ms due to both the presence of ^{29}Si as well as the readout mechanism being employed [85].

In Figure 4.41 we show the results of using XY16 sequence to replace the single π pulse of the Hahn echo. For all the results shown for the D^+, the delay between the π pulses in the XY16 sequence was 8 ms. At 1.2 K the coherence decay follows a single exponential, with a T_2 of 180 min, whereas at 1.9 K and 4.2 K there is an early component of a faster decay (time constant ~12 min), followed by a decay consistent with a T_2 of 180 min. We believe that this initial faster decay is due to charge dynamics in the sample after illumination, probably from D^- and A^+ centers, which are frozen out at the lowest temperature [161].

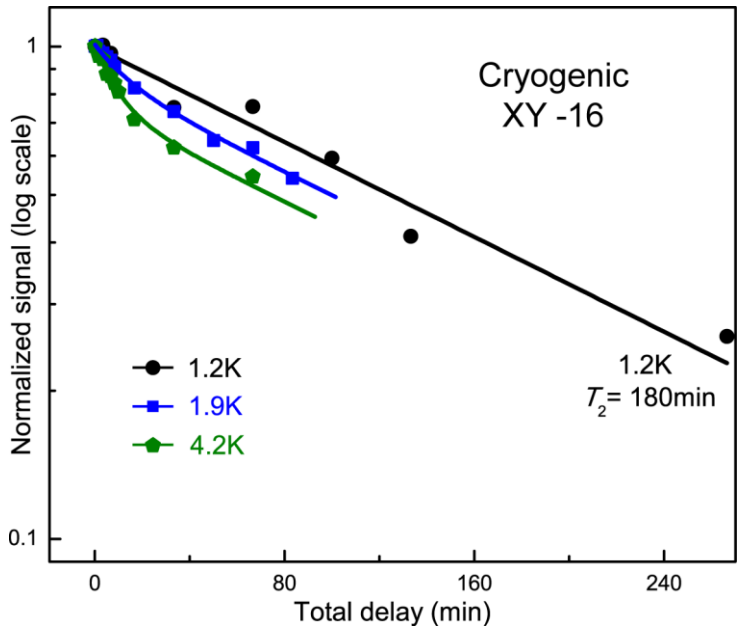

Figure 4.41: ***T_2 decays using the XY16 decoupling sequence at cryogenic temperatures. The 1.9 and 4.2 K data were fit using biexponentials, with the longer component set to 180 min.***

The low-temperature nuclear spin T_2 of ≥180 min demonstrates that the XY16 sequence is very effective in suppressing decoherence arising from slow spectral diffusion caused by the remaining ^{29}Si.

These long coherence times for the D^+ nuclear spin should be achievable even when the donor is placed near an interface in a nanodevice, as long as the temperature is low enough that flips or flip-flops of electron spins at the interface are suppressed. In addition to the promise of longer cryogenic coherence times, the removal of the hyperfine-coupled electron should result in a profound change in the temperature dependence of T_2. For the neutral donor, the electron T_1 decreases very rapidly with increasing temperature, and even at 4.2 K the nuclear T_2 is limited by the electron T_1 . This mechanism is absent for the ionized donor, and we will report on nuclear coherence time measurements for ionized ^{31}P at room temperature.

The BB1 version of XY16 for T_2 measurement of D^+ at room temperature

At liquid He temperatures and in the dark there will be no free carriers in the sample, but this of course changes as the temperature is raised. Above ~30 K the remaining neutral boron begins to thermally ionize (~1% ionized) and above 70 K essentially all the boron is ionized, providing ~$5x10^{13}$ cm^{-3} of free holes. This free hole concentration is essentially constant between 70 K and room temperature. Due to the p-type doping of the sample, e^- do not begin to appear until 230 K (~1 cm^{-3}), increasing to ~$1.2x10^6$ cm^{-3} at room temperature. These free electrons and holes could in principle have acted to depolarize or decohere the $^{31}P^+$ nuclear spins, but they are seen to have a relatively small effect. At room temperature the probability of an e^- being bound to a D^+ to give D^0 in our sample is ~ $2x10^{-13}$.

A τ of 8 ms was near optimal for XY16 decoupling at low temperature and worked well for short delays at room temperature (less than ~10 min.), but for longer times at room temperature a rapid decrease in the nuclear spin coherence signal intensity was observed. We hypothesized that this was due to a slow warming of the RF coil and transmission line for longer room temperature measurements, causing the coil tuning to change and making the π pulse length inaccurate beyond the point which could be corrected for by the XY16 sequence. We therefore replaced the simple π pulses with

BB1 composite π pulses [144], which give a closer approximation to an exact π rotation when the π pulse length is incorrect by a factor which is constant over the duration of the composite pulse. The five individual π pulses of each BB1 composite pulse were placed close together in time, with the time evolution of the system taking place during the 8 ms between the composite π pulses. This provided an adequate solution to our inability to match coil parameters as a function of temperature. A better solution would be to operate the RF coil and transmission line at a constant temperature, thermally isolated from the sample holder.

In Figure 4.42 we show a room-temperature T_2 decay of 39 min. This is a lower bound, because the same XY16 sequence applied to a ± Z state yields a decay constant of 50 min, which is substantially shorter than the 78-min T_1, indicating that pulse errors in the XY16 sequence contribute significantly to the observed decay and are also likely to contribute to the 180-min T_2 observed at cryogenic temperatures.

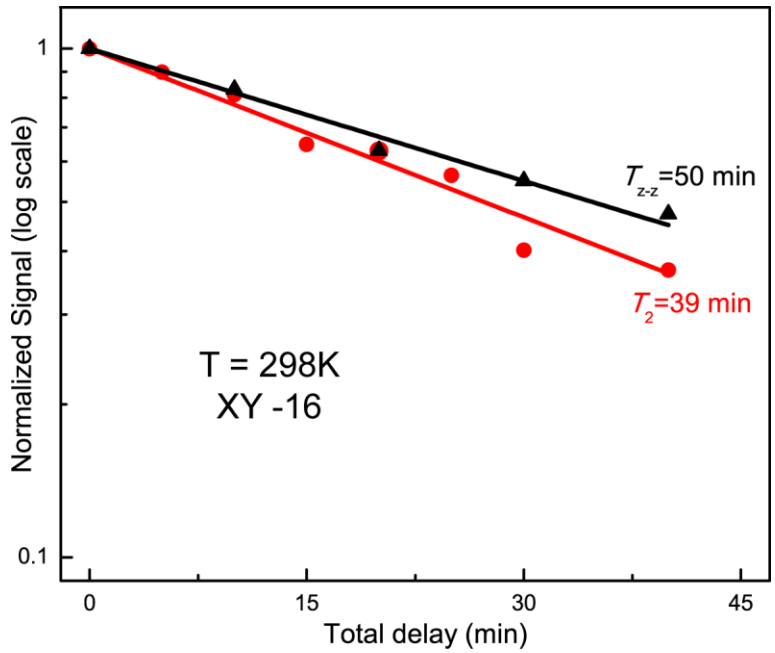

Figure 4.42: ***The T_2 decay at 298 K using XY16 decoupling, together with the observed decay of a ± Z state using XY16 decoupling under identical conditions.***

The shorter 39-min T_2 measured at room temperature could arise from carrier-induced magnetic field fluctuations, whose effect is not completely suppressed by the dynamical decoupling, combined with a higher error in the RF pulses [164].

The observed room-temperature T_2 is also compatible with the accumulated phase error from the small probability of the donor being in the D^0 ground state at room temperature. The observed room-temperature T_2 considerably exceeds that 25 s reported for ^{29}Si in natural Si using homonuclear decoupling [166]. Given that ^{29}Si should not be more sensitive to free carriers than D^+, this probably results from difficulty in completely decoupling the ^{29}Si at the high concentration present in natural Si.

Cycling D^+ coherent state from 4.2K to room temperature and back

We demonstrated the ability to change the sample temperature while the D^+ nuclear spin was in a coherent superposition state. Figure 4.43A shows a reference measurement at 4.2 K using the sequence shown in Figure 3.7, but with XY16 decoupling.

In Figure 4.43B, the D^+ nuclear spins are placed into a coherent superposition at 4.2 K, the XY16 sequence is begun, and then the temperature is ramped to room temperature in ~6 min. It is held there for 2 min before being ramped back down to 4.2 K in ~4 min. Once the sample is reimmersed in liquid He, the XY16 sequence ends and the remaining coherence is projected back into a ± Z state for readout after reneutralization.

By comparing the two readout signals we see that it is possible to bring a coherent state from cryogenic temperature to room temperature and back while retaining 62% of the coherence signal, which is equivalent to a state fidelity of 81% [167]. This loss of coherence can be largely attributed to the ~30% drop in nuclear spin polarization observed over one thermal cycle to room temperature and back.

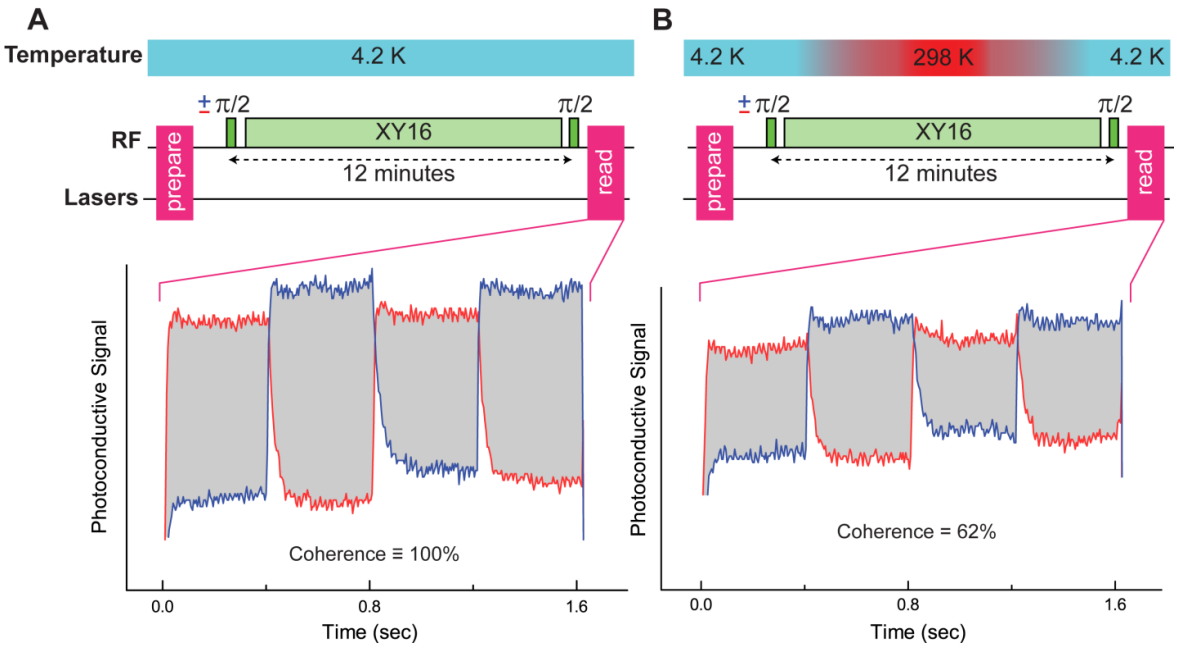

Figure 4.43: ***Cycling D^+, while in a nuclear spin superposition state, from 4.2 K to room temperature and back. (A) A measurement at a constant temperature of 4.2K, with XY16 decoupling over a 12-min period, is compared to (B), where the nuclear spins are placed into a coherent superposition at 4.2K and the XY16 decoupling sequence is begun, followed by a ~6-min ramp to 298K, 2 min at 298K, and a ~4-min ramp back down to 4.2K, after which the remaining coherence is read out. The preparation and readout sequences are as in Figure 3.4.***

4.11. Decoherence mechanisms discussion

We have already remarked on the near agreement between the observed D^0 and D^+ Hahn echo T_2 times, which could have suggested a common mechanism given that the same sample material (^{28}Si-Avo) was used, a possibility which is excluded by the further observation that XY16 decoupling extends T_2 by a factor of 400 for D^+ but only ~4.4 for D^0. Our D^+ results are well-accounted for by a combination of B_0 inhomogeneity and spectral diffusion due to the spins of the remaining ^{29}Si [86], and we now re-examine the possible mechanisms limiting the D^0 results both for the p-type Avogadro material [54] as well as the n-type material used in the original optical-NMR study [137], which has the same ^{28}Si enrichment as the Avogadro samples but ~1000 times more ^{31}P.

The hyperfine coupling present for D^0 allowed nuclear coherence measurements [54, 137] to be done at a field (~845.3 G) where $\partial RF_{\uparrow}/\partial B_0 = \partial RF_{\downarrow}/\partial B_0 = 0$, also referred to as a 'clock transition'. This was done to relax the requirement for B_0 homogeneity, given our relatively low homogeneity electromagnet. That this was successful can be seen by the fact that improving the B0 homogeneity by adding ring shims to the magnet, which improved the Ramsey fringe T_2^* for D^+ from 0.8 ms to 4.2 ms, had no effect on T_2^* for D^0, which was 38 ms before and after shimming, as seen in Figure 4.32. Operating at a clock transition additionally makes the frequency very insensitive to small fluctuations in B_0, greatly suppressing decoherence due to spectral diffusion processes [168]. We therefore consider other mechanisms, which do not involve B_0 noise, as possible sources for the coherence signal decay in the D^0 case.

We have already mentioned that in the early stages of this study of D^+ we observed decay in the D^0 population in the dark after photoneutralization resulting from donor-acceptor-pair recombination [164]. This neutral donor population decay makes a small contribution to all the decay times reported for the D^0 system.

Given that for D^0 the use of the clock transition should suppress the effects of noise and inhomogeneity in B_0, we believe that the major source of decoherence and inhomogeneous broadening for the D^0 nuclear spins in our experiments arise from modulations of the hyperfine coupling A. At our B_0 and higher, $\partial RF\uparrow/\partial A \cong \partial RF\downarrow/\partial A \cong 0.5$, and with $A \cong 117$ MHz even very small fractional changes or noise in A can be responsible for decoherence. The hyperfine constant can be affected by electric field [169, 170] or strain [171], and it is interesting to note that even changing the sample environment from 1.3 K and near-zero pressure to 4.2 K and atmospheric pressure changes A for ^{31}P by 3.1 kHz [137], a very large change in frequency on the scale of the coherence times observed for neutral ^{31}P.

The modulation of A by static inhomogeneous fields in the sample arising from chemical impurities such as the ^{31}P itself, or electrically inactive impurities such as C and O, or even from the remaining ^{29}Si and ^{30}Si [172] can explain the D^0 T_2^* of 38 ms for the present sample, which at first seemed surprisingly short given that the measurements were done at a clock transition. This is supported by the observation that a shorter T_2^* of 16.4 ms was observed for the n-type sample [137], and that the ratio of the T_2^*'s, 2.3,

is almost identical to the ratio of 2.2 between the inhomogeneously broadened bound exciton spectral linewidths in the two samples, with a full width at half maximum of 7.6 x 10^{-4} cm^{-1} for the Avogadro sample and 1.7 x 10^{-3} cm^{-1} for the n-type sample.

There must also be a contribution to the low temperature T_2 which can be lengthened by the XY16 decoupling, which was able to extend T_2 from 44 s to 192 s. One candidate is spectral diffusion due to indirect donor electron flip-flops, which might not be completely suppressed by operating at the clock transition. Another could be modulation of A by electric field noise, as the photoneutralized donors and acceptors slowly ionize in the dark by donor-acceptor-pair recombination. Estimating the size of this effect is difficult, since measurements of the hyperfine Stark shift for Sb in Si give a value -3.7x10^{-3} $\mu m^2/V^2$ [169], considerably smaller than the -2 x10^{-2} $\mu m^2/V^2$ calculated for ^{31}P [170]. Taking these two values, the ionization of an impurity located 1 μm from a coherent donor, as is roughly appropriate for the impurity concentrations in the p-type Avogadro sample, would produce a hyperfine shift of the NMR frequency by ~19 mHz or ~3.6 mHz, which could contribute significantly to the 44 s Hahn echo T_2 and still be ameliorated by the XY16 dynamical decoupling. The hyperfine Stark effect due to the static electric fields from ionized impurities could also contribute to the observed T_2*, but even assuming that 10% of the donors are ionized immediately after the hyperpolarization process, the resulting electric field distribution [173] would produce a frequency broadening of only ~1 Hz or ~0.2 Hz, making a very small contribution to the 38 ms T_2*.

5. Conclusions

We have shown that by eliminating almost all inhomogeneous broadening and host spins, highly enriched ^{28}Si approaches a semiconductor vacuum, enabling the use of hyperfine-resolved optical transitions, as is standard for atom and ion qubits in vacuum, but retaining the advantages of Si device technology, Auger photoionization for polarization and readout, and the ability to precisely and permanently place the qubit atoms [124].

The AEDMR mechanism we introduce here should be extensible to the readout of single ^{31}P impurities [62, 174] and could be combined with the already demonstrated spin-dependent–tunneling electron spin readout of single ^{31}P [175]. The method can be applied to other substitutional donors when ^{28}Si samples become available, and in particular Bi, where the much larger hyperfine coupling makes the hyperfine D^0X structure almost resolvable even in natural Si [68].

We have measured a new record cryogenic coherence time of over 180 min. for the nuclear spin of $^{31}P^+$ in ^{28}Si. To make use of the D^+ state as a quantum memory for, say, a donor-based electron spin qubit, as has already been done with the nuclear spin of D^0 [60], it will be necessary to find a way to ionize and neutralize the donor without disturbing the coherent state of the nuclear spin. The measured $T_2 \geq 39$ min. for $^{31}P^+$ in ^{28}Si at room temperature is an improvement of over three orders of magnitude on the qubit coherence time of ~2 s reported recently for a ^{13}C nuclear spin coupled to an NV center in isotopically enriched diamond [81]. It exceeds by almost two orders of magnitude the longest previously reported [166] solid-state nuclear T_2 of 25 s for ^{29}Si in natural Si obtained using homonuclear decoupling at room temperature (the absence of charged states or optical transitions in that system make it difficult to implement a ^{29}Si qubit, but a scheme has been proposed [176]).

These results would be important for the proposed cluster-state quantum computing scheme where quantum information is stored in the nuclear spins of ionized

donors [177] and support the possibility of truly long term storage of quantum information at room temperature. While ^{31}P donors in ^{28}Si at this time require low temperatures for initialization and readout, the ability to bring coherent information reversibly between cryogenic and room temperatures already suggests ways to exploit this particular system. It may also be possible to initialize and read out this system at elevated temperatures, or to find similar but more robust systems with larger electron binding energies, in which charge control can still be used to turn a hyperfine interaction on for initialization and readout and off for long term storage. In Si, one possibility would be to use much deeper donors such as chalcogens, where an optically accessible hyperfine splitting has already been observed for $^{77}Se^{+}$ in ^{28}Si [118], and where the hyperfine coupling can be removed by placing the donor into either D^{0} or D^{2+} charge states. Another promising possibility would be deep systems in wider-gap materials such as diamond and SiC [178], which can also be isotopically purified to remove background spins, and where the method of charge state control could be combined with initialization and readout at room temperature.

References

[1] M. A. Nielsen and I. L. Chuang, Quantum Computation and Quantum Information, Cambridge University Press, 2000.

[2] L. K. Grover, "A fast quantum mechanical algorithm for database search," in *28th Annual ACM Symposium on the Theory of Computing*, 1996.

[3] P. Shor, "Algorithms for quantum computation: discrete logarithms and factoring," in *35th Annual Symposium on Foundations of Computer Science*, Santa Fe, NM, 1994.

[4] P. W. Shor, "Polynomial-Time Algorithms for Prime Factorization and Discrete Logarithms on a Quantum Computer," *SIAM J.Sci.Statist.Comput.,* p. 1484–1509, 1997.

[5] R. P. Feynman, "Simulating physics with computers," *International Journal of Theoretical Physics,* pp. 467-488, 1982.

[6] S. Simmons, *Creation and Control of Entanglement in Condensed Matter Spin Systems,* Oxford: University of Oxford, 2011.

[7] D. Deutsch, "Quantum theory, the Church-Turing principle and the universal quantum computer," *Proc. R. Soc. Lond. A,* p. 97–117, 1985.

[8] E. Farhi, J. Goldstone, S. Gutmann, J. Lapan, A. Lundgren and D. Preda, "A Quantum Adiabatic Evolution Algorithm Applied to Random Instances of an NP-Complete Problem," *Science,* pp. 472-475, 2001.

[9] M. Amin, P. Love and C. Truncik, "Thermally assisted adiabatic quantum computation," *Phys. Rev. Lett.,* p. 060503, 2008.

[10] M. Johnson, M. Amin, S. Gildert, T. Lanting, F. Hamze, N. Dickson, R. Harris, A. Berkley, J. Johansson, P. Bunyk, E. Chapple, C. Enderud, J. Hilton, K. Karimi, E. Ladizinsky, N. Ladizinsky, T. Oh, I. Perminov, C. Rich, M. Thom and E. Tolkacheva, "Quantum Annealing with Manufactured Spins," *Nature,* p. 194, 2011.

[11] R. Raussendorf and H. J. Briegel, "A One-Way Quantum Computer," *Phys. Rev. Lett.,* pp. 5188-5191, 2001.

[12] H. J. Briegel and R. Raussendorf, "Persistent Entanglement in Arrays of Interacting Particles," *Phys. Rev. Lett.,* pp. 910-913, 2001.

[13] P. Walther, K. J. Resch, T. Rudolph, E. Schenck, H. Weinfurter, V. Vedral, M. Aspelmeyer and A. Zeilinger, "Experimental one-way quantum computing," *Nature,* pp. 169-176, 2005.

[14] G. Vallone, E. Pomarico, P. Mataloni, F. De Martini and V. Berardi, "Realization and Characterization of a Two-Photon Four-Qubit Linear Cluster State," *Phys. Rev. Lett. ,* p. 180502, 2007.

[15] D. P. DiVincenzo, "Quantum computation," *Science,* pp. 255-261, 1995.

[16] F. Macwilliams and N. Sloane, The theory of error-correcting codes, Amsterdam: North-Holland, 1977.

[17] D. P. DiVincenzo, "The physical implementation of quantum computation," *Fortschritte der Physik,* p. 771–783, 2000.

[18] T. D. Ladd, "Quantum computers," *Nature,* pp. 45-53, 2010.

[19] I. L. Chuang and Y. Yamamoto, "Simple quantum computer," *Phys. Rev. A,* pp. 3489--3496, 1995.

[20] P. G. Kwiat, J. R. Mitchell, P. D. D. Schwindt and A. G. White, "Grover's search algorithm: An optical approach," *Journal of Modern Optics,* pp. 257-266, 2000.

[21] K. Watanabe and Y. Yamamoto, "Limits on tradeoffs between third-order optical nonlinearity, absorption loss, and pulse duration in self-induced transparency and real excitation," *Phys. Rev. A,* pp. 1699-1702, 1990.

[22] A. Imamoglu and Y. Yamamoto, "Turnstile device for heralded single photons: Coulomb blockade of electron and hole tunneling in quantum confined p-i-n heterojunctions," *Phys. Rev. Lett.,* pp. 210-213, 1994.

[23] J. I. Cirac and P. Zoller, "Quantum Computations with Cold Trapped Ions," *Phys. Rev. Lett.,* pp. 4091-4094, 1995.

[24] D.J. Wineland and D. Leibfried, "Quantum information processing and metrology with trapped ions," *Laser Physics Letters,* pp. 175–188, 2011.

[25] A. Steane, "The ion-trap quantum information processor," *Appl. Phys. B-Lasers and Optics,* pp. 623-642, 1997.

[26] C. Monroe, D. M. Meekhof, B. E. King, W. M. Itano and D. J. Wineland, "Demonstration of a Fundamental Quantum Logic Gate," *Phys. Rev. Lett.,* pp. 4714-4717, 1995.

[27] R. G. Brewer, R. G. DeVoe and R. Kallenbach, "Planar ion microtraps," *Phys. Rev. A,* pp. R6781--R6784, 1992.

[28] Rainer Blatt and David Wineland, "Entangled states of trapped atomic ions," *Nature,* pp. 1008-1015, 2008.

[29] D. G. Cory, A. F. Fahmy and T. F. Havel, "Ensemble quantum computing by NMR spectroscopy," *PNAS,* p. 1634–1639, 1997.

[30] N. A. Gershenfeld and I. L. Chuang, "Bulk Spin-Resonance Quantum Computation," *Science,* pp. 350-356, 1997.

[31] W. S. Warren, "The Usefulness of NMR Quantum Computing," *Science,* pp. 1688-1690, 1997.

[32] I. L. Chuang, N. Gershenfeld and M. Kubinec, "Experimental Implementation of Fast Quantum Searching," *Phys. Rev. Lett.,* pp. 3408-3411, 1998.

[33] D. Loss and D. P. DiVincenzo, "Quantum computation with quantum dots," *Phys. Rev. A,* pp. 120-126, 1998.

[34] A. Huibers, M. Switkes, C. Marcus, K. Campman and A. Gossard, "Dephasing in open quantum dots," *Physica B: Condensed Matter,* pp. 348-352, 1998.

[35] A. Imamoglu, D. D. Awschalom, G. Burkard, D. P. DiVincenzo, D. Loss, M. Sherwin and A. Small, "Quantum Information Processing Using Quantum Dot Spins and Cavity QED," *Phys. Rev. Lett.,* pp. 4204-4207, 1999.

[36] Y. Nakamura, Y. A. Pashkin and J. S. Tsai, "Coherent control of macroscopic quantum states in a single-Cooper-pair box," *Nature,* pp. 786-788, 1999.

[37] J. E. Mooij, T. P. Orlando, L. Levitov, L. Tian, H. v. d. W. Caspar and S. Lloyd, "Josephson Persistent-Current Qubit," *Science,* pp. 1036-1039, 1999.

[38] B. E. Kane, "A silicon-based nuclear spin quantum computer," *Nature,* pp. 133-137, 1998.

[39] R. Vrijen, E. Yablonovitch, K. Wang, H. W. Jiang, A. Balandin, V. Roychowdhury, T. Mor and D. DiVincenzo, "Electron-spin-resonance transistors for quantum computing in silicon-germanium heterostructures," *Phys. Rev. A,* p. 012306, 2000.

[40] J. J. Morton and B. W. Lovett, "Hybrid Solid-State Qubits:The Powerful Role of Electron Spins," *Annu. Rev. Condens.Matter Phys.,* p. 189–212, 2011.

[41] E. Knill, R. Laflamme, R. Martinez and C.-H. Tseng, "An algorithmic benchmark for quantum information processing," *Nature,* pp. 368-370, 2000.

[42] K. C. Nowack, F. H. L. Koppens, Y. V. Nazarov and L. M. K. Vandersypen, "Coherent Control of a Single Electron Spin with Electric Fields," *Science,* pp. 1430-1433 , 2007.

[43] J. Wrachtrup, "Defect center room-temperature quantum processors," *PNAS,* pp. 9479-9480, 2010.

[44] R. C. Fletcher, W. A. Yager, G. L. Pearson and F. R. Merritt, "Hyperfine Splitting in Spin Resonance of Group V Donors in Silicon," *Phys. Rev. ,* p. 844, 1954.

[45] M. Xiao, I. Martin, E. Yablonovitch and H. Jiang, "Electrical detection of the spin resonance of a single electron in a silicon field-effect transistor," *Nature,* pp. 435-439, 2004.

[46] J. J. Pla, K. Y. Tan, J. P. Dehollain, W. H. Lim, J. J. L. Morton, D. N. Jamieson, A. S. Dzurak and A. Morello, "A single-atom electron spin qubit in silicon," *Nature,* pp. 541-545, 2012.

[47] D. Rugar, R. Budakian, H. J. Mamin and B. W. Chui, "Single spin detection by magnetic resonance force microscopy," *Nature,* pp. 329-332, 2004.

[48] J. M. Elzerman, R. Hanson, L. H. W. van Beveren, B. Witkamp, L. M. K. Vandersypen and L. P. Kouwenhoven, "Single-shot read-out of an individual electron spin in a quantum dot," *Nature,* pp. 431-435, 2004.

[49] F. Jelezko, I. Popa, A. Gruber, C. Tietz, J. Wrachtrup, A. Nizovtsev and S. Kilin, "Single spin states in a defect center resolved by optical spectroscopy," *Appl. Phys. Lett.,* p. 2160, 2002.

[50] F. Jelezko, T. Gaebel, I. Popa, M. Domhan, A. Gruber and J. Wrachtrup, "Observation of Coherent Oscillation of a Single Nuclear Spin and Realization of a Two-Qubit Conditional Quantum Gate," *Phys. Rev. Lett.,* p. 130501, 2004.

[51] R. J. Epstein, F. M. Mendoza, Y. K. Kato and D. D. Awschalom, "Anisotropic interactions of a single spin and dark-spin spectroscopy in diamond," *Nature Phys.,* pp. 94 - 98, 2005.

[52] T. Gaebel, M. Domhan, I. Popa, C. Wittmann, P. Neumann, F. Jelezko, J. R. Rabeau, N. Stavrias, A. D. Greentree, S. Prawer, J. Meijer, J. Twamley, P. R. Hemmer and J. Wrachtrup, "Room-temperature coherent coupling of single spins in diamond," *Nature Phys.,* pp. 408 - 413, 2006.

[53] A. M. Tyryshkin, S. Tojo, J. J. L. Morton, H. Riemann, N. V. Abrosimov, P. Becker, H.-J. Pohl, T. Schenkel, M. L. W. Thewalt, K. M. Itoh and S. A. Lyon, "Electron spin coherence exceeding seconds in high-purity silicon," *Nature Materials,* p. 143–147, 2012.

[54] M. Steger, K. Saeedi, M. L. W. Thewalt, J. J. L. Morton, H. Riemann, N. V. Abrosimov, P. Becker and H.-J. Pohl, "Quantum Information Storage for over 180s Using Donor Spins in a 28Si “Semiconductor Vacuum”," *Science,* pp. 1280-1283, 2012.

[55] K. Saeedi, S. Simmons, J. Salvail, P. Dluhy, H. Riemann, N. V. Abrosimov, P. Becker, H.-J. Pohl, J. J. L. Morton and M. L. W. Thewalt, "Room-Temperature Quantum Bit Storage Exceeding 39 Minutes Using Ionized Donors in Silicon-28," *Science,* pp. 830-833, 2013.

[56] J. J. L. Morton, A. M. Tyryshkin, A. Ardavan, S. C. Benjamin, K. Porfyrakis, S. A. Lyon and G. A. D. Briggs, "Bang-bang control of fullerene qubits using ultra-fast phase gates," *Nature Physics,* pp. 40-43, 2006.

[57] G. D. Fuchs, V. V. Dobrovitski, D. M. Toyli, F. J. Heremans and D. D. Awschalom, "Gigahertz Dynamics of a Strongly Driven Single Quantum Spin," *Science,* pp. 1520-1522, 2009.

[58] N. Zhao and J. Wrachtrup, "Quantum information: Best of both worlds," *Nature Materials,* p. 97–98, 2013.

[59] A. M. Stoneham, A. J. Fisher and P. T. Greenland, "Optically driven silicon-based quantum gates with potential for high-temperature operation," *J. Phys.: Condens. Matter,* p. L447, 2003.

[60] J. J. L. Morton, A. M. Tyryshkin, R. M. Brown, S. Shankar, B. W. Lovett, A. Ardavan, T. Schenkel, E. E. Haller, J. W. Ager and S. A. Lyon, "Solid-state quantum memory using the 31P nuclear spin," *Nature,* pp. 1085-1088, 2008.

[61] D. Karaiskaj, M. L. W. Thewalt, T. Ruf, M. Cardona, H.-J. Pohl, G. G. Deviatych, P. G. Sennikov and H. Riemann, "Photoluminescence of Isotopically Purified Silicon: How Sharp are Bound Exciton Transitions?," *Phys. Rev. Lett.,* p. 6010, 2001.

[62] A. Yang, M. Steger, D. Karaiskaj, M. L. W. Thewalt, M. Cardona, K. M. Itoh, H. Riemann, N. V. Abrosimov, M. F. Churbanov, A. V. Gusev, A. D. Bulanov, A. K. Kaliteevskii, O. N. Godisov, P. Becker, H.-J. Pohl, J. W. Ager and E. E. Haller, "Optical Detection and Ionization of Donors in Specific Electronic and Nuclear Spin States," *Phys. Rev. Lett.,* p. 227401, 2006.

[63] N. Q. Vinh, P. T. Greenland, K. Litvinenko, B. Redlich, A. F. G. v. d. Meer, S. A. Lynch, M. Warner, A. M. Stoneham, G. Aeppli, D. J. Paul, C. R. Pidgeon and B. N. Murdin, "Silicon as a model ion trap: Time domain measurements of donor Rydberg states," *PNAS,* pp. 10649-10653, 2008.

[64] D. R. McCamey, J. V. Tol, G. W. Morley and C. Boehme, "Fast Nuclear Spin Hyperpolarization of Phosphorus in Silicon," *Phys. Rev. Lett.,* p. 027601, 2009.

[65] A. Yang, M. Steger, T. Sekiguchi, M. L. W. Thewalt, T. D. Ladd, K. M. Itoh, H. Riemann, N. V. Abrosimov, P. Becker and H.-J. Pohl, "Simultaneous Subsecond Hyperpolarization of the Nuclear and Electron Spins of Phosphorus in Silicon by Optical Pumping of Exciton Transitions," *Phys. Rev. Lett.,* p. 257401, 2009.

[66] A. Yang, M. Steger, T. Sekiguchi, M. L. W. Thewalt, J. W. Ager and E. E. Haller, "Homogeneous linewidth of the 31P bound exciton transition in silicon," *Appl. Phys. Lett.,* p. 122113, 2009.

[67] P. T. Greenland, S. A. Lynch, A. F. G. v. d. Meer, B. N. Murdin, C. R. Pidgeon, B. Redlich, N. Q. Vinh and G. Aeppli, "Coherent control of Rydberg states in silicon," *Nature,* p. 1057–1061, 2010.

[68] T. Sekiguchi, M. Steger, K. Saeedi, M. L. W. Thewalt, H. Riemann, N. V. Abrosimov and N. Nötzel, "Hyperfine Structure and Nuclear Hyperpolarization Observed in the Bound Exciton Luminescence of Bi Donors in Natural Si," *Phys. Rev. Lett.,* p. 137402, 2010.

[69] R. E. George, W. Witzel, H. Riemann, N. V. Abrosimov, N. Nötzel, M. L. W. Thewalt and J. J. L. Morton, "Electron Spin Coherence and Electron Nuclear Double Resonance of Bi Donors in Natural Si," *Phys. Rev. Lett.,* p. 067601, 2010.

[70] M. H. Mohammady, G. W. Morley and T. S. Monteiro, "Bismuth Qubits in Silicon: The Role of EPR Cancellation Resonances," *Phys. Rev. Lett.,* p. 067602, 2010.

[71] G. W. Morley, M. Warner, A. M. Stoneham, P. Greenland, J. V. Tol, C. W. M. Kay and G. Aeppli, "The initialization and manipulation of quantum information stored in silicon by bismuth dopants," *Nature Materials,* p. 725–729, 2010.

[72] H. Morishita, L. S. Vlasenko, H. Tanaka, K. Semba, K. Sawano, Y. Shiraki, M. Eto and K. M. Itoh, "Electrical detection and magnetic-field control of spin states in phosphorus-doped silicon," *Phys. Rev. B,* p. 205206, 2009.

[73] K.-M. C. Fu, T. D. Ladd, C. Santori and Y. Yamamoto, "Optical detection of the spin state of a single nucleus in silicon," *Phys. Rev. B,* p. 125306, 2004.

[74] J. Stajic, "The future of quantum information processing," *Science,* pp. 1163-1184, 2013.

[75] D. R. McCamey, J. V. Tol, G. W. Morley and C. Boehme, "Electronic Spin Storage in an Electrically Readable Nuclear Spin Memory with a Lifetime >100 Seconds," *Science,* pp. 1652-1656, 2010.

[76] S. Simmons, R. M. Brown, H. Riemann, N. V. Abrosimov, P. Becker, H.-J. Pohl, M. L. W. Thewalt, K. M. Itoh and J. J. L. Morton, "Entanglement in a solid-state spin ensemble," *Nature,* p. 69–72, 2011.

[77] M. Fuechsle, J. A. Miwa, S. Mahapatra, H. Ryu, S. Lee, O. Warschkow, L. C. L. Hollenberg, G. Klimeck and M. Y. Simmons, "A single-atom transistor," *Nature Nanotechnology,* pp. 1-5, 2012.

[78] J. J. Pla, K. Tan, J. P. Dehollain, W. H. Lim, J. J. L. Morton, F. A. Zwanenburg, D. N. Jamieson, A. S. Dzurak and A. Morello, "High-fidelity readout and control of a nuclear spin qubit in silicon," *Nature,* p. 334–338, 2013.

[79] S. Wiesner, "Conjugate coding," *ACM SIGACT News,* pp. 78-88, 1983.

[80] F. Pastawski, N. Y. Yao, L. Jiang, M. D. Lukin and J. I. Cirak, "Unforgeable noise-tolerant quantum tokens," *PNAS,* pp. 16079-16082, 2012.

[81] P. C. Maurer, G. Kucsko, C. Latta, L. Jiang, N. Y. Yao, S. D. Bennett, F. Pastawski, D. Hunger, N. Chisholm, M. Markham, D. J. Twitchen, J. I. Cirac and M. D. Lukin, "Room-temperature quantum bit memory exceeding one second," *Science,* pp. 1283-1286, 2012.

[82] J. J. L. Morton, D. R. McCamey, M. A. Eriksson and S. A. Lyon, "Embracing the quantum limit in silicon computing," *Nature,* pp. 345-353, 2011.

[83] D. D. Awschalom, L. C. Bassett, A. S. Dzurak, E. L. Hu and J. R. Petta, "Quantum spintronics: engineering and manipulating atom-like spins in semiconductors," *Science,* pp. 1174-1179, 2013.

[84] G. Feher and E. A. Gere, "Electron Spin Resonance Experiments on Donors in Silicon. II. Electron Spin Relaxation Effects," *Phys. Rev.,* p. 1245 , 1959.

[85] L. Dreher, F. Hoehne, M. Stutzmann and M. S. Brandt, "Nuclear Spins of Ionized Phosphorus Donors in Silicon," *Phys. Rev. Lett.,* p. 027602, 2012.

[86] W. M. Witzel, M. S. Carroll, Ł. Cywiński and S. D. Sarma, "Quantum decoherence of the central spin in a sparse system of dipolar coupled spins," *Phys. Rev. B,* p. 035452, 2012.

[87] J. A. Jones and M. Mosca, "Implementation of a Quantum Algorithm on a Nuclear Magnetic Resonance Quantum Computer," *J. Chem. Phys.,* pp. 1648-1653, 1998.

[88] C. Negrevergne, T. S. Mahesh, C. A. Ryan, M. Ditty, F. Cyr-Racine, W. Power, N. Boulant, T. Havel, D. G. Cory and R. Laflamme, "Benchmarking Quantum Control Methods on a 12-Qubit System," *Phys. Rev. Lett.,* p. 170501, 2006.

[89] L. M. K. Vandersypen, M. Steffen, G. Breyta, C. S. Yannoni, M. H. Sherwood and I. L. Chuang, "Experimental realization of Shor's quantum factoring algorithm using nuclear magnetic resonance," *Nature,* pp. 883-887, 2001.

[90] J. J. L. Morton, A. M. Tyryshkin, A. Ardavan, K. Porfyrakis, S. A. Lyon and G. A. D. Briggs, "High Fidelity Single Qubit Operations Using Pulsed Electron Paramagnetic Resonance," *Phys. Rev. Lett.,* p. 200501, 2005.

[91] A. Malvino and D. J. Bates, Electronic principles, Mc Graw Hill, 2007.

[92] D. A. Neamen, Semiconductor physics and devices, Mc Graw Hill, 2003.

[93] A. Yang, *Optical Hyperpolarization and Detection of Electron and Nuclear Spins of Phosphorus Donors in Highly Enriched 28Si,* Burnaby: SFU, 2010.

[94] W. Kohn, "Shallow Impurity States in Silicon and Germanium," *Solid State Physics,* p. 257–320, 1957.

[95] W. Kohn, "Shallow impurity states in semiconductors," *Il Nuovo Cimento,* pp. 713-723, 1958.

[96] P. Y. Yu and M. Cardona, Fundamentals of Semiconductors: Physics and Materials Properties, Berlin: Springer, 2005.

[97] G. Feher, "Electron Spin Resonance Experiments on Donors in Silicon. I. Electronic Structure of Donors by the Electron Nuclear Double Resonance Technique," *Phys. Rev.,* p. 1219, 1959.

[98] M. A. Lampert, "Mobile and Immobile Effective-Mass-Particle Complexes in Nonmetallic Solids," *Phys. Rev. Lett. ,* p. 450, 1958.

[99] J. R. Haynes, "Experimental Proof of the Existence of a New Electronic Complex in Silicon," *Phys. Rev. Lett.,* pp. 361-363 , 1960.

[100] M. Tajima, "Determination of boron and phosphorus concentration in silicon by photoluminescence analysis," *Appl. Phys. Lett.,* p. 719, 1978.

[101] K. Nishikawa and R. Barrie, "Phonon broadening of impurity spectral lines. I.General theory," *Can. J. Phys.,* p. 1135, 1963.

[102] D. F. Nelson, J. D. Cuthbert, P. J. Dean and D. G. Thomas, "Auger Recombination of Excitons Bound to Neutral Donors in Gallium Phosphide and Silicon," *Phys. Rev. Lett.,* p. 1262–1265, 1966.

[103] W. Schmid, "Auger lifetimes for excitons bound to neutral donors and acceptors in Si," *Phys. Stat. Sol. B,* p. 529, 1977.

[104] P. J. Dean and D. C. Herbert, "Bound excitons in semiconductors, Topics in Current Physics: Excitons," Berlin, Springer , 1979, p. 55.

[105] M. L. W. Thewalt, "Excitons," Amsterdam, North Holland, 1982, p. 393–458.

[106] E. E. Haller, "Isotopically engineered semiconductors," *J. Appl. Phys.,* pp. 2857-2878, 1995.

[107] T. Ruf, R. Henn, M. Asen-Palmer, E. Gmelin, M. Cardona, H.-J. Pohl, G. G. Devyatych and P. G. Sennikov, "Thermal conductivity of isotopically-enriched silicon," *Solid State Commun.,* p. 143, 2000.

[108] F. Widulle, T. Ruf, M. Konumaa, I. Silier, M. Cardona, W. Kriegseis and V. I. Ozhogin, "Isotope effects in elemental semiconductors: a raman study of silicon," *Solid State Commun.,* pp. 1-22, 2001.

[109] P. Becker, H.-J. Pohl, H. Riemann and N. V. Abrosimov, "Enrichment of silicon for a better kilogram," *physica status solidi (a),* pp. 49-66, 2010.

[110] P. G. Sennikov, A. V. Vodopyanov, S. V. Golubev, D. Mansfeld, M. Drozdov, Y. N. Drozdov, B. Andreev, L. Gavrilenko, D. Pryakhin, V. I. Shashkin, O. Godisov, A. Glasunov, A. J. Safonov, H.-J. Pohl, M. Thewalt, P. Becker, H. Riemann, N. Abrosimov and S. Valkiers, "Towards 0.99999 28Si," *Solid State Communications,* pp. 455-457, 2012.

[111] M. Cardona and M. L. W. Thewalt, "Isotope effects on the optical spectra of semiconductors," *Rev. Mod. Phys.,* p. 1173, 2005.

[112] D. Karaiskaj, M. L. Thewalt, T. Ruf, M. Cardona and M. Konuma, "'intrinsic' acceptor ground state splitting in silicon: an isotopic effect," *Phys. Rev. Lett.,* p. 016401, 2002.

[113] D. Karaiskaj, M. L. W. Thewalt, T. Ruf and M. Cardona, "Photoluminescence studies of isotopically enriched silicon," *Phys. Status Solidi B,* p. 63, 2002.

[114] M. L. W. Thewalt, D. Karaiskaj, T. Ruf and M. Cardona, "Ultrahigh resolution photoluminescence spectroscopy of isotopically pure silicon," *Inst. Phys. Cong. Ser.,* p. 101, 2003.

[115] D. Karaiskaj, J. A. H. Stotz, T. Meyer, M. L. W. Thewalt and M. Cardona, "Impurity Absorption Spectroscopy in 28Si: The Importance of Inhomogeneous Isotope Broadening," *Phys. Rev. Lett.,* p. 186402, 2003.

[116] M. Steger, A. Yang, M. L. W. Thewalt, M. Cardona, H. Riemann, N. V. Abrosimov, M. F. Churbanov, A. V. Gusev, A. D. Bulanov, I. D. Kovalev, A. K. Kaliteevskii, O. N. Godisov, P. Becker, H.-J. Pohl, J. W. Ager III and E. E. Haller, "Impurity absorption spectroscopy of the deep double donor sulfur in isotopically enriched silicon," *Physica B,* p. 600–603, 2007.

[117] M. Steger, A. Yang, T. Sekiguchi, K. Saeedi, M. L. W. Thewalt, M. O. Henry, K. Johnston, H. Riemann, N. V. Abrosimov, M. F. Churbanov, A. V. Gusev, A. K. Kaliteevskii, O. N. Godisov, P. Becker and H.-J. Pohl, "Photoluminescence of deep defects involving transition metals in Si: New insights from highly enriched 28Si," *Journal of Applied Physics,* p. 081301, 2011.

[118] M. Steger, A. Yang, M. L. W. Thewalt, M. Cardona, H. Riemann, N. V. Abrosimov, M. F. Churbanov, A. V. Gusev, A. D. Bulanov, I. D. Kovalev, A. K. Kaliteevskii, O. N. Godisov, P. Becker, H.-J. Pohl, E. E. Haller and J. W. Ager, "High-resolution absorption spectroscopy of the deep impurities S and Se in 28Si revealing the 77Se hyperfine splitting," *Phys. Rev. B,* p. 115204, 2009.

[119] A. Yang, M. Steger, M. L. W. Thewalt, M. Cardona, H. Riemann, N. V. Abrosimov, M. F. Churbanov, A. V. Gusev, A. D. Bulanov, I. D. Kovalev, A. K. Kaliteevskii, O. N. Godisov, P. Becker, H.-J. Pohl, J. W. Ager III and E. E. Haller, "High resolution photoluminescence of sulphur- and copper-related isoelectronic bound excitons in highly enriched 28Si," *Physica B: Condensed Matter,* pp. 593-596, 2007.

[120] M. Steger, A. Yang, T. Sekiguchi, K. Saeedi, M. L. W. Thewalt, M. Henry, K. Johnston, H. Riemann, N. Abrosimov, M. Churbanov, A. Gusev, A. Bulanov, I. Kaliteevski, O. Godisov, P. Becker and H.-J. Pohl, "Isotopic fingerprints of gold-containing luminescence centers in 28Si," *Physica B: Condensed Matter,* pp. 5050-5053, 2009.

[121] M. Steger, A. Yang, T. Sekiguchi, K. Saeedi, M. L. W. Thewalt, M. O. Henry, K. Johnston, E. Alves, U. Wahl, H. Riemann, N. V. Abrosimov, M. F. Churbanov, A. V. Gusev, A. K. Kaliteevskii, O. N. Godisov, P. Becker and H.-J. Pohl, "Isotopic fingerprints of Pt-containing luminescence centers in highly enriched 28Si," *Phys. Rev. B,* p. 235217, 2010.

[122] M. Thewalt, M. Steger, A. Yang, N. Stavrias, M. Cardona, H. Riemann, N. Abrosimov, M. Churbanov, A. Gusev, A. Bulanov, I. Kovalev, A. Kaliteevskii, O. Godisov, P. Becker, H.-J. Pohl, J. Ager III and E. Haller, "Can highly enriched 28Si reveal new things about old defects?," *Physica B: Condensed Matter,* p. 587–592, 2007.

[123] M. Steger, A. Yang, N. Stavrias, M. L. W. Thewalt, H. Riemann, N. V. Abrosimov, M. F. Churbanov, A. V. Gusev, A. D. Bulanov, I. D. Kovalev, A. K. Kaliteevskii, O. N. Godisov, P. Becker and H.-J. Pohl, "Reduction of the Linewidths of Deep Luminescence Centers in 28Si Reveals Fingerprints of the Isotope Constituents," *Phys. Rev. Lett.,* p. 177402, 2008.

[124] S. R. Schofield, N. J. Curson, M. Y. Simmons, F. J. Rueß, T. Hallam, L. Oberbeck and R. G. Clark, "Atomically Precise Placement of Single Dopants in Si," *Phys. Rev. Lett.,* p. 136104, 2003.

[125] L. M. K. Vandersypen and I. L. Chuang, "NMR techniques for quantum control and computation," *Rev. Mod. Phys.,* pp. 1037-1069, 2004.

[126] G. Burkard, H. A. Engel and D. Loss, "Spintronics and quantum dots for quantum computing and quantum communication," *Fortschr. Phys.,* pp. 965-986, 2000.

[127] W. Harneit, "Fullerene-based electron-spin quantum computer," *Phys. Rev. A,* p. 032322 , 2002.

[128] A. Ardavan, M. Austwick, S. C. Benjamin, G. A. D. Briggs, T. J. S. Dennis, A. Ferguson, D. G. Hasko, M. Kanai, A. N. Khlobystov, B. W. Lovett, G. W. Morley, R. A. Oliver, D. G. Pettifor, K. Porfyrakis, J. H. Reina, J. H. Rice, J. D. Smith, R. A. Taylor, D. A. Williams, C. Adelmann, H. Mariette and R. J. Hamers, "Nanoscale solid-state quantum computing," *Phil. Trans. R. Soc. A,* pp. 1473-1485, 2003.

[129] S. A. Lyon, "Spin-based quantum computing using electrons on liquid helium," *Phys. Rev. A,* p. 052338*,* 2006.

[130] A. Schweiger and G. Jeschke, Principles of Pulse Electron Paramagnetic Resonance, Oxford University Press, 2008.

[131] M. H. Levitt, Spin Dynamics: Basics of Nuclear Magnetic Resonance, Wiley, 2001.

[132] W. N. Hardy, A. J. Berlinsky and L. A. Whitehead, "Magnetic Resonance Studies of Gaseous Atomic Hydrogen at Low Temperatures," *Phys. Rev. Lett.,* p. 1042 , 1979.

[133] T. G. Castner, "Orbach Spin-Lattice Relaxation of Shallow Donors in Silicon," *Phys. Rev.,* p. 816, 1967.

[134] G. P. Carver, D. F. Holcomb and J. A. Kaeck, "31P Spin Echoes in Metallic Phosphorus-Doped Silicon," *Phys. Rev. B,* p. 4285, 1971.

[135] H. Alloul and P. Dellouve, "Spin localization in Si:P—direct evidence from 31P NMR," *Phys. Rev. Lett. ,* pp. 578-581, 1987.

[136] M. Jeong, M. Song, T. Ueno, T. Mizusaki, A. Matsubara and S. Lee, "Spin Coherence Time T 2 in Metallic P-doped Si at Very Low Temperature," *Journal of Low Temperature Physics,* pp. 659-665, 2010.

[137] M. Steger, T. Sekiguchi, A. Yang, K. Saeedi, M. E. Hayden, M. L. W. Thewalt, K. M. Itoh, H. Riemann, N. V. Abrosimov, P. Becker and H.-J. Pohl, "Optically-detected NMR of optically-hyperpolarized 31P neutral donors in 28Si," *J. Appl. Phys.,* p. 102411, 2011.

[138] A. M. Tyryshkin, S. A. Lyon, A. V. Astashkin and A. M. Raitsimring, "Electron spin relaxation times of phosphorus donors in silicon," *Phys. Rev. B,* p. 193207, 2003.

[139] J. J. L. Morton, A. M. Tyryshkin, A. Ardavan, K. Porfyrakis, S. A. Lyon and G. A. D. Briggs, "Measuring errors in single-qubit rotations by pulsed electron paramagnetic resonance," *Phys. Rev. A,* p. 012332, 2005.

[140] E. L. Hahn, "Spin Echoes," *Phys. Rev. ,* pp. 580-, 1950.

[141] R. Freeman, Spin Choreography: Basic Steps in High Resolution NMR, Oxford University Press, 1998.

[142] M. H. Levitt, "Composite pulses," *Progress in Nuclear Magnetic Resonance Spectroscopy,* p. 61–122, 1986.

[143] M. H. Levitt, "Composite Pulses," in *Encyclopedia of NMR*, John Wiley & Sons, Ltd, 1996.

[144] S. Wimperis, "Broadband, Narrowband, and Passband Composite Pulses for Use in Advanced NMR Experiments," *J. Magn. Reson. A,* p. 221–231, 1994.

[145] L. Viola, S. Lloyd and E. Knil, "Universal Control of Decoupled Quantum Systems," *Phys. Rev. Lett. ,* p. 4888, 1999.

[146] T. van der Sar, Z. H. Wang, M. S. Blok, H. Bernien, T. H. Taminiau, D. M. Toyli, D. A. Lidar, D. D. Awschalom, R. Hanson and V. V. Dobrovitski, "Decoherence-protected quantum gates for a hybrid solid-state spin register," *Nature,* p. 82–86, 2012.

[147] R. C. Jaeger, Introduction to Microelectronic Fabrication, Upper Saddle River, NJ,: Prentice Hall, 2001.

[148] A. N. Safonov, G. Davies and E. C. Lightowlers, "Lineshape of the no-phonon luminescence of excitons bound to phosphorus in carbon-doped silicon," *Phys. Rev. B,* p. 4409, 1996.

[149] P. Becker, D. Schiel, H.-J. Pohl, A. Kaliteevski, N. Godisov, M. F. Churbanov, G. Devyatykh, A. Gusev, A. D. Bulanov, S. A. Adamchik, V. Gavva, I. D. Kovalev, N. V. Abrosimov, B. Hallmann-Seiffert, H. Riemann, S. Valkiers, P. Taylor, P. D. Bièvre and E. M. Dianov, "Large-scale production of highly enriched 28Si for the precise determination of the Avogadro constant," *Meas. Sci. Technol.,* p. 1854, 2006.

[150] W. Keller and A. Muhlbauer, "Float zone silicon," in *Preparation and properties of solid state materials vol.5*, New York, Dekker, 1981.

[151] A. S. Kaminskii, L. I. Kolesnik, B. M. Leiferov and Y. E. Pokrovskii, "Luminescence analysis of group III and V impurities in silicon," *Zh. Prikl. Spektrosk,* p. 745, 1982.

[152] P. L. McColley and E. C. Lightowlers, "Calibration of the photoluminescence technique for measuring B, P and Al concentrations in Si in the range 1012 to 1015 cm−3 using Fourier transform spectroscopy," *Semicond. Sci. Technol.,* p. 157, 1987.

[153] I. Pelant, J. Dian, J. Matouskova, J. Valenta, J. Hala, M. Ambroz, M. Vacha, V. Kohlova, K. Vojtechovsky and K. Kaslik, "Photoluminescence assessment of B, P, and Al in Si wafers: The problem of sample heating by a laser beam," *J. Appl. Phys.,* p. 3477, 1993.

[154] I. Broussell, J. A. H. Stotz and M. L. W. Thewalt, "Method for shallow impurity characterization in ultrapure silicon using photoluminescence," *J. Appl. Phys.,* p. 5913, 2002.

[155] M. Steger, *Photoluminescence of deep defects involving transition metals in silicon – new insights from highly enriched 28Si,* Burnaby: SFU, 2011.

[156] A. W. Overhauser, "Polarization of Nuclei in Metals," *Phys. Rev. ,* p. 411 , 1953.

[157] L. Viola and S. Lloyd, "Dynamical suppression of decoherence in two-state quantum systems," *Phys. Rev. A,* p. 2733 , 1998.

[158] Z.-H. Wang, W. Zhang, A. M. Tyryshkin, S. A. Lyon, J. W. Ager, E. E. Haller and V. V. Dobrovitski, "Effect of pulse error accumulation on dynamical decoupling of the electron spins of phosphorus donors in silicon," *Phys. Rev. B,* p. 085206, 2012.

[159] T. Gullion, D. B. Baker and M. S. Conradi, "New, compensated Carr-Purcell sequences," *J. Magn. Reson.,* pp. 479-484, 1990.

[160] M. Cardona, T. A. Meyer and M. L. W. Thewalt, "Temperature Dependence of the Energy Gap of Semiconductors in the Low-Temperature Limit," *Phys. Rev. Lett.,* p. 196403, 2004.

[161] W. Burger and K. Lassmann, "Energy-Resolved Measurements of the Phonon-Ionization of D− and A+ Centers in Silicon with Superconducting-Al Tunnel Junctions," *Phys. Rev. Lett.,* p. 2035, 1984.

[162] A. S. Kaminskii, V. A. Karasyuk and Y. E. Pokrovskii, "Luminescence of excitons bound to phosphorus atoms in silicon subjected to a magnetic field," *Sov. Phys. JETP,* p. 211, 1980.

[163] G. L. Bir and G. E. Pikus, Symmetry and Deformation Effects in Semiconductors, Moscow: Nauka, 1972.

[164] P. Dirksen, A. Henstra and W. T. Wenckebach, "An electron spin echo study of donor-acceptor recombination," *J. Phys.: Condens. Matter,* pp. 7085-7092, 1989.

[165] A. M. Tyryshkin, Z.-H. Wang, W. Zhang, E. E. Haller, J. W. Ager, V. V. Dobrovitski and S. A. Lyon, "Dynamical Decoupling in the Presence of Realistic Pulse Errors," *arXiv:1011.1903v2,* 2010.

[166] T. D. Ladd, D. Maryenko, Y. Yamamoto, E. Abe and K. M. Itoh, "Coherence time of decoupled nuclear spins in silicon," *Phys. Rev. B,* p. 014401 , 2005.

[167] R. Jozsa, "Fidelity for Mixed Quantum States," *J. Mod. Opt.,* p. 2315–2323, 1994.

[168] G. Wolfowicz, A. M. Tyryshkin, R. E. George, H. Riemann, N. V. Abrosimov, P. Becker, H.-J. Pohl, M. L. W. Thewalt, S. A. Lyon and J. J. L. Morton, "Atomic clock transitions in silicon-based spin qubits," *Nature Nanotechnology,* p. 561–564, 2013.

[169] F. R. Bradbury, A. M. Tyryshkin, G. Sabouret, J. Bokor, T. Schenkel and S. A. Lyon, "Stark Tuning of Donor Electron Spins in Silicon," *Phys. Rev. Lett.,* p. 176404 , 2006.

[170] M. Friesen, "Theory of the Stark Effect for P Donors in Si," *Phys. Rev. Lett. ,* p. 186403 , 2005.

[171] L. Dreher, T. A. Hilker, A. Brandlmaier, S. T. B. Goennenwein, H. Huebl, M. Stutzmann and M. S. Brandt, "Electroelastic Hyperfine Tuning of Phosphorus Donors in Silicon," *Phys. Rev. Lett. ,* p. 037601 , 2011.

[172] D. Karaiskaj, G. Kirczenow, M. L. W. Thewalt, R. Buczko and M. Cardona, "Origin of the Residual Acceptor Ground-State Splitting in Silicon," *Phys. Rev. Lett.,* p. 016404 , 2003.

[173] D. M. Larsen, "Inhomogeneous broadening of the Lyman-series absorption of simple hydrogenic donors," *Phys. Rev. B ,* p. 1681 , 1976.

[174] D. Sleiter, N. Y. Kim, K. Nozawa, T. D. Ladd, M. L. W. Thewalt and Y. Yamamoto, "Quantum Hall charge sensor for single-donor nuclear spin detection in silicon," *New J. Phys.,* p. 093028, 2010.

[175] A. Morello, J. J. Pla, F. A. Zwanenburg, K. Chan, K. Y. Tan, H. Huebl, M. Möttönen, C. D. Nugroho, C. Yang, J. A. van Donkelaar, A. D. Alves, D. N. Jamieson, C. C. Escott, L. C. Hollenberg, R. G. Clark and A. S. Dzurak, "Single-shot readout of an electron spin in silicon," *Nature,* pp. 687-691, 2010.

[176] T. D. Ladd, J. R. Goldman, F. Yamaguchi, Y. Yamamoto, E. Abe and K. M. Itoh, "All-Silicon Quantum Computer," *Phys. Rev. Lett.,* p. 017901 , 2002.

[177] J. J. L. Morton, "A silicon-based cluster state quantum computer," *arXiv:0905.4008,* 2009.

[178] W. F. Koehl, B. B. Buckley, F. J. Heremans, G. Calusine and D. D. Awschalom, "Room temperature coherent control of defect spin qubits in silicon carbide," *Nature,* p. 84–87, 2011.